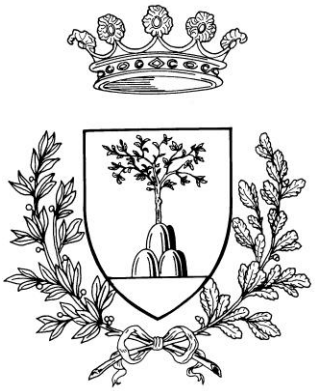

UNIVERSITÀ DEGLI STUDI DI FERRARA

Corso di Laurea Magistrale in Ingegneria Meccanica

THERMAL ANALYSIS OF THE THERMAL SHIELD AND WARM BORE IN THE Mu2e TRANSPORT SOLENOID

Tesi di Laurea di:

Veronica Ilardi

Relatore:

Chiar.mo Prof. Stefano Piva

Correlatori:

Thomas H. Nicol

Mauricio Lopes

Anno Accademico 2015 – 2016

1. INTRODUCTION

Mu2e is an experiment currently under construction, located at Fermi National Accelerator Laboratory (Fermilab), which aims to detect muon to electron conversion in the field of a nucleus.

The experiment will utilize three superconducting solenoids to accomplish this task: the Production Solenoid (PS), the Transport Solenoid (TS) and the Detector Solenoid (DS). The TS consists of two separate cryostats: the TSu (Transport Solenoid, upstream) and the TSd (Transport Solenoid, downstream). The cryogenic system used to cool down the solenoids, so, is formed by four semi-autonomous cryostats: one for the PS, one for the TSu, one for the TSd and one for the DS.

The cryostats can be cooled down or warmed up independent of the state of the other cryostats. Each of them will require 4.5 - 4.7 K liquid helium as well as 80 - 90 K liquid nitrogen for the cryostat thermal shields.

The TS cryostats include a Vacuum Vessel, a Thermal Shield, a Coil Module Assembly and a Warm Bore. The Vacuum Vessel, which is the outermost cryostat component, served to contain the insulating vacuum and functioned as the major structural element to which all other systems are ultimately attached to the floor, through three supports. It has an inner diameter equal to ID = 1605.95 mm and a thickness t = 19.05 mm; it is made by austenitic stainless steel (316L), maintained at room temperature (T = 293.15 K) and has a pressure $p = 1.3 \times 10^{-4}$ Pa.

Inside the Vacuum Vessel is the Thermal Shield, which acts as a radiative barrier and is cooled using a series of tubes, containing liquid nitrogen, which also provide a structural skeleton.

It is divided in the Outer and the Inner Thermal Shield, both made by 6061 T6 aluminum alloy and maintained at a temperature T = 80 K and at a pressure $p = 1.3 \times 10^{-4}$ Pa.

The outer shield has an inner diameter equal to ID = 1280.55 mm and a thickness t = 6.35 mm; the inner one has an inner diameter equal to ID = 631.75 mm and a thickness t = 6.35 mm.

Between the Outer and the Inner Thermal Shield is the Coil Module Assembly, maintained at a temperature T = 4 K by several tubes containing liquid helium.

Eventually, inside the Inner Thermal Shield is the Warm Bore, with an inner diameter equal to ID = 500 mm and a thickness t = 15.875 mm. It is made by stainless steel (316L) and maintained at room temperature (T = 293.15 K) and at a pressure $p = 1.3 \times 10^{-4}$ Pa.

The first part of this paper (Section 7) has the purpose to analyze the Thermal Shield cooling system under two different aspects.

First of all, a steady state thermal analysis was conducted (Section 7.1) to establish how many nitrogen tubes were required to maintain the Thermal Shield at a temperature T = 80 K.

After this, a transient thermal analysis was developed (Section 7.2) in order to determine how long the Thermal Shield took to cool down.

In the second part of the paper (Section 8) are presented two steady state thermal analysis of the Warm Bore.

The Warm Bore and the Thermal Shield have different temperatures, so there is a heat flux that comes from the Warm Bore and enters the inner surface of the Inner Thermal Shield. Since there is vacuum inside the whole Vacuum Vessel, the heat flux is due to radiation and residual gas conduction.

The first analysis, so, aims to determine the Warm Bore temperature, considering the heat flux. Its results are presented in Section 8.4.

Although, the second analysis (Section 8.5) takes into account the scenario with the Warm Bore temperature lower than the temperature at which the water freezes. This is not a problem during the experiment, because the cryostat is sealed and the vacuum is maintained inside it. However, we need to open it for maintenance and, in this case, the air is expected to enter the Warm Bore and the water contained in it to freeze on the walls. In order to avoid the icing, it was decided to put some heaters on the Warm Bore external surface.

The second steady state thermal analysis on the Warm Bore aims to establish how many heaters are necessary, in what position and at what power, to maintain the Warm Bore at room temperature, in order to avoid icing during the opening of the cryostat, or even in the case of a vacuum loss.

2. MU2E PROJECT MISSION

Fermi National Accelerator Laboratory and the Mu2e Collaboration, composed of about 155 scientists and engineers from 28 universities and laboratories around the world, have collaborated to create this technical design for a new facility to study charged lepton flavor violation using the existing Department of Energy investment in the Fermilab accelerator complex.

Mu2e proposes to measure the ratio of the rate of the neutrinoless, coherent conversion of muons into electrons in the field of a nucleus, relative to the rate of ordinary muon capture on the nucleus.

The conversion process is an example of charged lepton flavor violation (CLFV), a process that has never been observed experimentally. The current best experimental limit on muon-to-electron conversion is from the SINDRUM II experiment [1] and Mu2e will probe four orders of magnitude beyond the SINDRUM II sensitivity. Observation of this process would provide unambiguous evidence for physics beyond the Standard Model and can help to illuminate discoveries made at the Large Hadron Collider (LHC) or point to new physics beyond the reach of the LHC.

To achieve the sensitivity goal cited above, a high intensity, low energy muon beam, coupled with a detector capable of efficiently identifying 105 MeV electrons while minimizing background from conventional processes, will be required. The muon beam is created by an 8 GeV proton beam striking a production target and a system of superconducting solenoids that efficiently collect pions and transport their daughter muons to a stopping target.

The scope of work required to meet the scientific and technical objectives of Mu2e is listed below:

- Modify the accelerator complex to transfer 8 GeV protons from the Fermilab Booster to the Mu2e detector, while the 120 GeV neutrino program is operating. To accomplish this, the existing Recycler and Debuncher Rings will be modified to re-bunch batches of protons from the Booster and then slow extract beam to the Mu2e detector.
- Design and construct a new beamline from the Debuncher Ring to the Mu2e detector. The beamline includes an extinction insert that removes residual out-of-time protons.
- Design and construct the Mu2e superconducting solenoid system (Figure 2.1), consisting of a Production Solenoid that contains the target for the primary proton beam, an S-shaped Transport Solenoid that serves as a magnetic channel for pions and muons of the correct charge and momentum range and a Detector Solenoid that houses the muon stopping target and the detector elements.

- Design and construct the Mu2e detector (Figure 2.1) consisting of a tracker, a calorimeter, a stopping target monitor, a cosmic ray veto, an extinction monitor and the electronics, trigger and data acquisition required to read out, select and store the data. The tracker accurately measures the trajectory of charged particles, the calorimeter provides independent measurements of energy, position and time, the cosmic ray veto identifies cosmic ray muons traversing the detector region that can cause backgrounds and the extinction monitor detects scattered protons from the production target to monitor the fraction of out-of-time beam.
- Design and construct a facility to house the Mu2e detector and the associated infrastructure (Figure 2.2). This includes an underground detector enclosure and a surface building to house necessary equipment and infrastructure that can be accessed while beam is being delivered to the detector.

Mu2e is integrated into Fermilab's overall science program that includes many experiments that use the same machines and facilities, though often in different ways. Because of the overlapping needs of several experimental programs, the scope of work described above will be accomplished through a variety of mechanisms. The NOvA and g-2 experiments both require upgrades to the Recycler Ring that will be used by Mu2e. Infrastructure required by both Mu2e and g-2 will be funded as common Accelerator Improvement Projects (AIPs) and General Plant Projects (GPPs). These common projects will be managed by Fermilab to ensure completion on a time scale consistent with the Lab's overall program plan and to guarantee that the needs of the overall program are satisfied.

REFERENCES

[1] W. Bertl, SINDRUM II Collaboration, *A Search for muon to electron conversion in muonic gold*, Eur. Phys. J. C47, 337, 2006

[2] arXiv:1501.05241, *Mu2e Technical Design Report*, March 2015

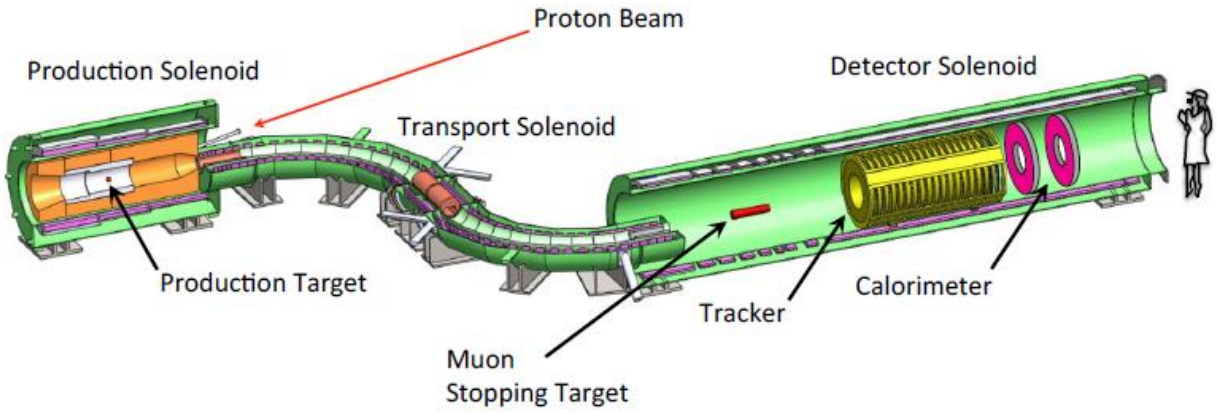

Figure 2.1 - The Mu2e Detector. (L. Bartoszek et al.)

Figure 2.2 - Depiction of the above-grade portion of the Mu2e facility. (L. Bartoszek et al.)

3. SUPERCONDUCTING SOLENOIDS

The solenoids perform several critical functions for the Mu2e experiment. Magnetic fields generated from these magnets are used to efficiently collect and transport muons from the production target to the muon stopping target while minimizing the transmission of other particles. Electrons are transported from the stopping target to detector elements where a uniform and precisely measured magnetic field is used to measure the momentum of electrons. The magnetic field values range from a peak of 4.6 T at the upstream end to 1 T at the downstream end [1]. In between is a complex field configuration consisting of graded fields, toroids and a uniform field region, each designed to satisfy a very specific set of criteria.

Mu2e creates this complex field configuration through the use of three magnetically coupled solenoid systems: the Production Solenoid (PS), the Transport Solenoid (TS) and the Detector Solenoid (DS). It also includes all ancillary systems such as magnet power converters, magnetic field mapping, cryogenic distribution and quench protection instrumentation and electronics.

The Mu2e solenoid system is shown in Figure 3.1.

3.1 PRODUCTION SOLENOID

The Production Solenoid, shown in Figure 3.2, is a high field magnet with a graded solenoidal field varying smoothly from 4.6 T to 2.5 T [1]. The gradient will be formed by 3 axial coils with a decreasing number of windings, made of aluminum stabilized NbTi. The solenoid is approximately 4 m long with an inner bore diameter of approximately 1.5 m that is evacuated to 1.3×10^{-3} Pa [1]. The Production Solenoid is designed to capture pions and the muons into which they decay and guide them downstream to the Transport Solenoid. This process is initiated by 8 GeV protons striking a production target near the center of the Production Solenoid [1]. A heat and radiation shield, constructed from bronze, will line the inside of the Production Solenoid to limit the heat load in the cold mass from secondaries produced in the production target and to limit radiation damage to the superconducting cable.

Protons enter the Production Solenoid through a small port on the low field side of the solenoid before intercepting the production target. Remnant protons that are not absorbed by the target and very forward-produced secondary particles exit at the high field end of the solenoid. Pions in the forward direction with angles greater than 30°, relative to the solenoid axis, are reflected back by the higher field and move along with the backward produced particles in helical trajectories towards the Transport Solenoid.

As mentioned above, the Production Solenoid must generate an axially graded field varying smoothly from 4.6 T to 2.5 T [1]. This axial field change is accomplished using three solenoid coils with 3, 2 and 2 layers of high-current, low-inductance aluminum-stabilized NbTi cable that allows for efficient energy extraction during a quench, requires fewer layers to achieve the required field strength and minimizes thermal barriers between the conductor and cooling channels. Aluminum stabilizer is used for several reasons: nuclear heating from the large flux of secondaries produced in the production target is reduced in aluminum compared to copper stabilizer, the other alternative; aluminum is less dense than copper, reducing the weight of the Production Solenoid; it can also be annealed at room temperature to reverse the impact of atomic displacements, primarily from neutrons, that degrade performance over time. This is further described in the section that follows.

3.1.1 Heat and Radiation Shield

Lining the inside of the Production Solenoid warm bore is a heat and radiation shield designed to protect the solenoid's superconducting coils (Figure 3.3). The Heat and Radiation Shield is designed to limit the heat load in the cold mass to prevent quenching, limit radiation damage to superconductor insulation and epoxy and limit the damage to the superconductor's aluminum stabilizer. The shield is constructed primarily from bronze. Because the proton beam is incident from one side of the Production Solenoid, the pattern of energy deposition in the heat shield is asymmetric with the largest depositions being near the target and collinear with the incoming proton beam direction. Even with the protection of the Heat and Radiation Shield, a significant number of atomic displacements will occur over time in the aluminum stabilizer surrounding the superconductor. The Residual Resistivity Ratio (RRR) of the aluminum, the ratio of the electrical resistance at room temperature of a conductor to that at 4.5 K, will decrease to the point where the stabilizer cannot adequately protect the superconductor in the event of a quench. The RRR can be completely recovered by warming the aluminum stabilizer to room temperature. Based on models of neutron production and energy deposition, it is anticipated that it will only be necessary to warm up once per year, coincident with annual accelerator shutdowns.

3.2 TRANSPORT SOLENOID

The S-shaped Transport Solenoid (Figure 3.4) consists of a set of superconducting solenoids and toroids, contained in two cryostats: the TSu cryostat ("upstream") and the TSd cryostat ("downstream"). This set forms a magnetic channel that efficiently transmits low energy negatively charged muons from the

Production Solenoid to the Detector Solenoid. Negatively charged particles with high energy, positively charged particles and line-of-sight neutral particles are nearly all eliminated by absorbers and collimators before reaching the Detector Solenoid. Selection of negatively charged muons is accomplished by taking advantage of the fact that a charged particle beam traversing a toroid will drift perpendicular to the toroid axis, with positives and negatives drifting in opposite directions. Most of the positively charged particles are absorbed in the central collimator. The Transport Solenoid consists of five distinct regions: a 1 m long straight section, a 90° curved section, a second straight section about 2 m long, a second 90° curved section that brings the beam back to its original direction, and a third straight section of 1 m length. The major radius of the two curved sections is about 3 m and the resulting total magnetic length of the Transport Solenoid along its axis is about 13 m. The inner warm bore of the Transport Solenoid cryostat has a diameter of about 0.5 m [1].

Late arriving particles are a serious potential background for Mu2e. To minimize the transport of particles that spend a long time in the magnet system, the magnetic field in the straight sections is designed to always have a negative gradient that accelerates particles from the Production Solenoid through the Detector Solenoid. This eliminates traps, where particles bounce between local maxima in the field until they eventually scatter out and travel to the Detector Solenoid where they arrive late compared to the beam pulse. The requirement on a negative gradient is relaxed in the curved sections of the TS because trapped particles will eventually drift vertically out of the clear bore and be absorbed by surrounding material.

3.3 DETECTOR SOLENOID

The Detector Solenoid (Figure 3.5) is a large, low field magnet that houses the muon stopping target and the components required to identify and analyze conversion electrons from the stopping target. It is nearly 11 m long with a clear bore diameter of about 2 m [1]. The muon stopping target resides in a graded field that varies from 2 T to 1 T [1]. The graded field captures conversion electrons that are emitted in the direction opposite the detector components causing them to reflect back towards the detector. The graded field also plays an important role in reducing background from high energy electrons that are transported to the Detector Solenoid by steadily increasing their pitch as they are accelerated towards the downstream detectors. The resulting pitch angle of these beam electrons is inconsistent with the pitch of a conversion electron from the stopping target. The actual detector components reside in a field region that is relatively uniform. The inner bore of the Detector Solenoid is evacuated to 1.3×10^{-2} Pa to limit backgrounds from muons that might stop on gas atoms [1]. The graded and uniform field sections of the Detector Solenoid

are wound on separate mandrels but housed in a common cryostat. The conductor is aluminum stabilized NbTi. The gradient is achieved by introducing spacers to effectively change the winding density of the superconducting cable.

The solenoids are the cost and schedule driver for the Project. The Production and Detector Solenoids will be constructed in industry. The relatively unique Transport Solenoid will be designed and fabricated at Fermilab, though many of the components (superconducting cable, cryostats, etc.) will be procured from industry. The make-buy decisions are based on the similarity of the Production and Detector Solenoids to other solenoids fabricated in industry and to the limited availability of resources at Fermilab. The superconducting cable required for the solenoids are long-lead items that must be procured early.

Significant infrastructure is required to support the operation of the solenoids. This includes power, quench protection, cryogens (liquid nitrogen and liquid helium), control and safety systems as well as mechanical supports to resist the significant magnetic forces on the magnets.

3.4 REQUIREMENTS OF THE SOLENOIDS

3.4.1 General Requirements

The Mu2e solenoids and their supporting subsystems are designed to meet a complex set of requirements. The requirements are defined so that the deliverables will meet the physics goals of the experiment. They are summarized below.

Because of the high magnetic field and large amount of stored energy, the solenoids will be made from superconducting NbTi coils, indirectly cooled with liquid helium and stabilized with high conductivity aluminum. It must be possible to cool down and energize each solenoid independent of the state of the adjacent magnets. Individual magnets will have different schedules for installation and commissioning, requiring independent operation. It will also be necessary to warm-up individual magnets to repair detector components housed inside or to anneal the conductor. Furthermore, it may be required that the magnets be operated in special field configurations for detector calibration. Significant axial forces will be present between these magnetically coupled systems and these forces will change if the fields are changed. The magnets must be designed to withstand these forces when they are being operated in their standard configuration as well as in the various configurations described above. The mechanical support for each of the magnets will be independent and will not depend on adjacent magnets. This simplifies integration issues, but complicates the mechanical support system. The bore of the magnets share a common beam vacuum but the magnet vacuums will be bridged with bellowed connections.

The solenoid coils must be designed for repeated full field quenches and thermal cycles, without degradation in performance, over the lifetime of the experiment. The expected duration of the experiment is 3 years at full luminosity; however, the magnets should be designed for the possibility of an extended physics run at the maximum design luminosity. The primary consequence of extended running will be the need for repeated thermal cycles to anneal the damage from irradiation. Quenches may occur during the initial campaign to full field as well as during normal operation conditions.

3.4.2 Magnetic Field Requirements

Each of the solenoids performs a different set of functions and each has a unique set of field requirements. Note that these requirements are necessary but not sufficient to fully specify the field. The magnetic field generated from the coil assemblies must keep experimental backgrounds at an acceptable limit. The field is verified to meet the Mu2e requirements only after extensive computer background simulations supplied by the Mu2e experiment. These studies must cover the full range of possible field values that can result from coil manufacturing tolerances.

3.4.2.1 PS Uniform axial gradient (PS2)

The Production Solenoid is a relatively high field solenoid with an axial grading that varies from 4.6 T to 2.5 T. The purpose of the Production Solenoid is to trap charged pions from the production target and direct them towards the Transport Solenoid as they decay to muons. The nominal peak field of 4.6 T provides the high end of the field gradient while still allowing for sufficient operating margins for temperature and current density with NbTi superconductor. There is a ± 5% requirement on the deviation from a uniform gradient along the axis (dB/B). At radii less than 0.3 m there can be no local field minimums where particles might get trapped. [1]

3.4.2.2 Solenoid straight sections in the transport solenoid (TS1, TS3, TS5)

Particles produced with a small pitch in a uniform field region can take a very long time to progress down the beamline toward the muon stopping target. To suppress background from these late arriving particles, the three straight sections in the Transport Solenoid employ negative axial gradients for radii smaller than 0.15 m. The radius is set by the geometry of the beam collimators. This requirement is intended to eliminate traps, where particles bounce between local maxima in the field until they eventually scatter out and travel to the Detector Solenoid where they arrive late and may cause background. [1]

3.4.2.3 Toroid sections (TS2 and TS4)

In the toroidal sections of the Transport Solenoid, the field varies as ~1/r, where r is the distance from the toroid center of curvature. In a toroid region, spiraling particles drift up or down depending on the sign of their charge, with a displacement that is proportional to their momentum and inversely proportional to their pitch. Particles with small pitch progress slowly through the toroid and drift to the wall where they are absorbed. This allows for a relaxed gradient specification in the toroid sections, defined by dBs/dr > 0.275 T/m, where s is the coordinate along the beam path. There is an additional requirement on the field ripple, dB, within a 0.15 m radius transverse to the central axis of the magnet system. Large field ripples can trap particles. [1]

3.4.2.4 Detector Solenoid Gradient region (DS1, DS2)

The muon stopping target resides in a graded field provided by the Detector Solenoid that varies from 2 T to 1 T. On the Transport Solenoid side of the muon stopping target, the graded field captures conversion electrons that are emitted in the direction opposite the detector components causing them to reflect back towards the detector. On the other side of the stopping target, the graded field focuses electrons towards the tracker and calorimeter. The graded field also plays an important role in background suppression by shifting the pitch of beam particles that enter the Detector Solenoid out of the allowed range for conversion electrons before they reach the tracker. The muon stopping target is located approximately in the middle DS1. In a conical volume defined by the proton absorber the uniformity requirement for the graded field is dB/ds = 0.25 T/m, where s is the direction along the solenoid axis. DS2 is the transition region between the graded and uniform fields. It should be as short as possible without introducing a local minimum in the axial field. [1]

3.4.2.5 Nearly Uniform field section (DS3 and DS4 Uniform)

The field in this region has two competing requirements. First, the magnetic field is important for the measurement of the electron momentum and energy. The trackerdetermined trajectory, along with the magnetic field map, determines the electron momentum. This requires the magnetic field to be as uniform as possible. The trackerdetermined trajectory is then extrapolated into the downstream calorimeter and matched with calorimeter energy deposition. The energy/momentum match further validates the electron identification. The second design consideration is that local field minima are a potential source of backgrounds. This background is reduced by superimposing a small negative axial gradient in the tracker and calorimeter region.

3.4.3 Alignment Requirements

Magnetic elements must be properly aligned with respect to one another as well as external interfaces such as beam collimators, the proton beam line and internal detector elements in order to assure optimal muon transmission, suppression of backgrounds, minimization of forces amongst magnetically coupled systems, and minimization of radiation damage due to improperly located collimators. Generally speaking, alignment tolerances between cryostated magnetic elements (PS, TSu, TSd, DS) in their cold and electrically powered nominal positions are ~10 mm. Alignment tolerances between coils within a cryostated magnet are ~5 mm. Alignment between magnets and tracker elements is ~0.1 mm. [1]

3.4.4 Radiation Requirements

Radiation damage to the solenoids must be carefully considered during the design process. The coil insulation, superconductor and superconductor stabilizer are the biggest concerns. The largest radiation dose is estimated to be 0.3 MGy/year at full beam intensity to the Production Solenoid. Materials with poor radiation properties must be avoided. Irradiation of the conductor and insulation is not expected to be a major concern over a 20-year life cycle. There is a significant concern about damage to the superconductor stabilizer in the Production Solenoid, causing a significant reduction in electrical and thermal conductivity at low temperature.

For aluminum, the stabilizer room temperature resistivity ratio (RRR) must not fall below ~100 over the lifetime of the experiment. For copper the requirement is for the RRR to stay above 30.

The experimental hall in the vicinity of the PS will be highly activated and accessible only to highly trained personnel under strictly controlled conditions; therefore, every effort must be made to reduce the need for access. Cryogenic valves, power connections and instrumentation connections should be located outside of this area. [1]

3.4.5 Electrical Requirements

The following electrical requirements have been developed for the solenoid system.

- The magnets will be designed with sufficient superconductor margin to allow operation without quenching at full field during the delivery of peak beam intensities. The target operating Jc margin is 30% and the required Tc margin is 1.5 K.
- The superconductor will be standard copper stabilized NbTi strand. In order to achieve the Jc and Tc margins for the Production Solenoid, the design Jc (4.2 K, 5 T) value must be greater than 2800 A/mm^2 for conductor in the peak field region of the PS. The magnet will be operated DC.

- The NbTi strand will be woven into a Rutherford cable. The cable will be further stabilized with low resistivity aluminum.
- The solenoids will be divided into several independent power circuits. Each circuit will have an external energy extraction resistor. The value of the resistor will be chosen so that the peak voltages will be limited during a quench to less than 300 V to ground and 600 V across the magnet terminals. For DS and PS depending on the intra-coil connection scheme, there is the possibility of ~100 V between adjacent coil layers. Coil-to-ground and layer-to-layer insulations must be sized to meet these requirements. Turn-to-turn voltages are not expected to exceed 10 V; however, cable insulations must be designed conservatively as these potentially damaging turn-to turn electrical breakdowns will be difficult to detect during fabrication.
- The peak coil temperature must not exceed 130 K as the result of a quench. Stabilizer will be sized to meet this requirement.
- To insure that there is no net transfer of magnetic stored energy between magnets during a quench, the stand-alone time constant for energy extraction for each power circuit must be set to approximately 30 seconds. [1]

3.4.6 Cryogenic Requirements

The solenoids will be divided into 4 cryogenic units. All solenoid coils will be potted with epoxy and indirectly (conduction) cooled by liquid helium. The coils can be cooled using either a “force flow” or a “thermal siphoning” system. 80 K thermal intercepts in the cryostat will be cooled by liquid nitrogen. Refrigerators located in a separate cryo building will supply liquid helium for the entire solenoid system. Based on the estimated heat loads, the required liquid helium can be supplied by one Tevatron “satellite” refrigerator. This means that during normal operations, the 4.5 K heat load cannot exceed 600 Watts. A second refrigerator will double the available capacity for use during initial cool-down and quench recovery. Cryogens will flow to and from each cryostat via a single cryo-link chimney. This chimney must be routed from the magnet cryostat through the concrete shielding and cosmic ray veto counters up to the cryogenic feed box located at ground level. Care must be taken in locating these gaps in the shielding to avoid “line of sight” paths for neutron and cosmic ray backgrounds. The chimney should be routed to minimize interference with utilities and crane coverage. [1]

REFERENCES

[1] arXiv:1501.05241, *Mu2e Technical Design Report*, March 2015

[2] G. Ambrosio, R. Coleman, V. Kashikhin, M. Lamm, N. Mokhov, J. Popp, V. Pronskikh, *Requirements for the Mu2e Production Solenoid Heat and Radiation Shield*, January 2013

[3] G. Tatkowski, S. Cheban, N. Dhanaraj, D. Evbota, M. Lopes, T. Nicol, R. Sanders, R. Schmitt, E. Voirin., *Forced two-phase helium cooling scheme for the Mu2e Transport Solenoid*, IOP Publishing Ltd

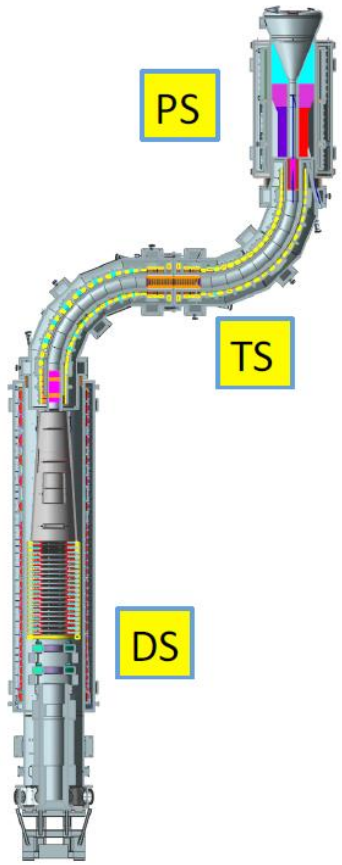

Figure 3.1 - The Mu2e solenoid system. (L. Bartoszek et al.)

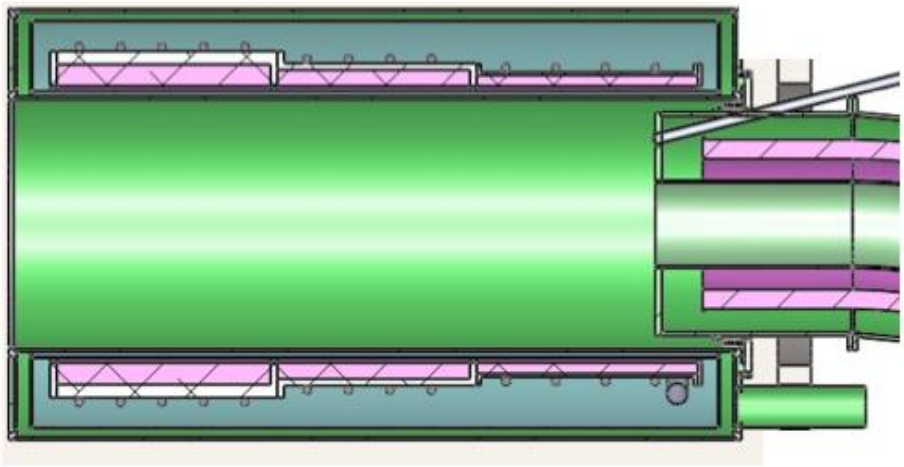

Figure 3.2 - Plan view of the Mu2e Production Solenoid. (L. Bartoszek et al.)

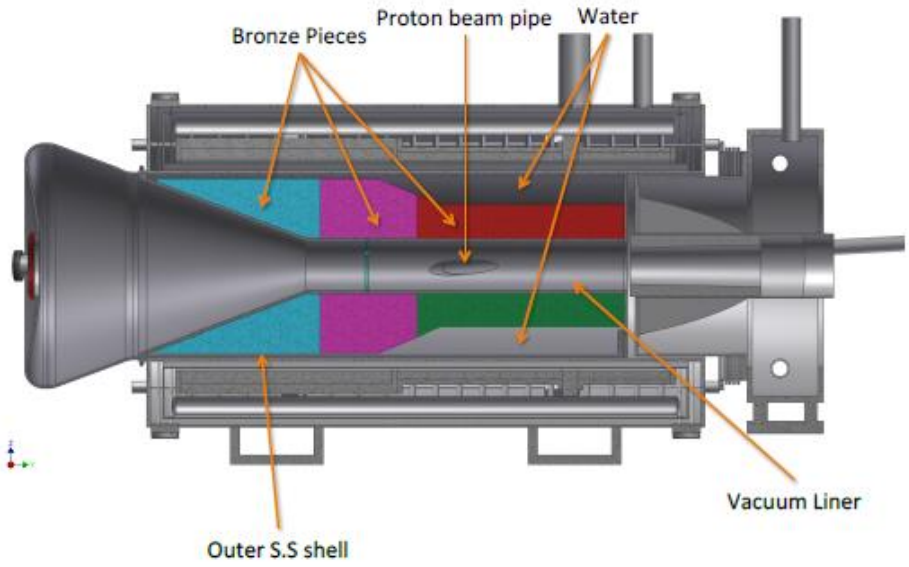

Figure 3.3 – Elevation view of the Heat and Radiation Shield. (L. Bartoszek et al.)

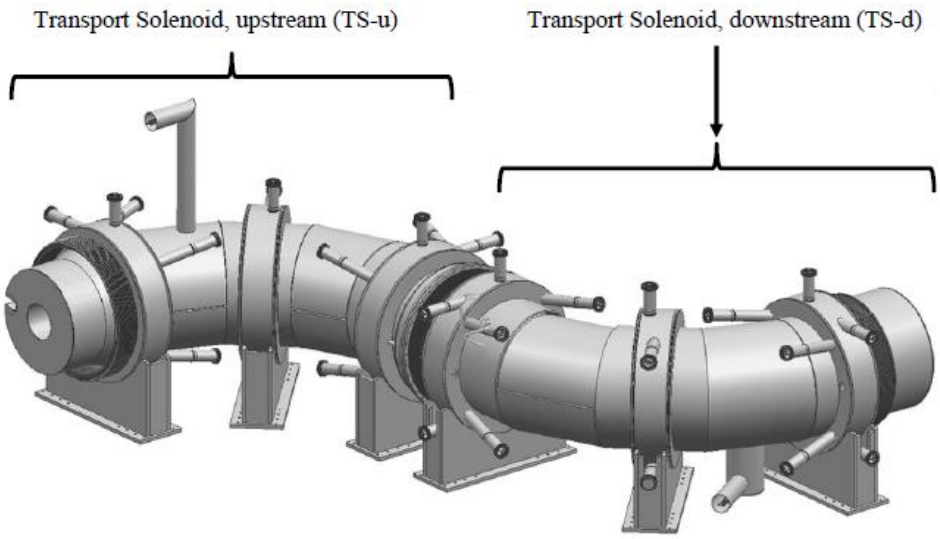

Figure 3.4 – 3D Model of the Mu2e Transport Solenoid. (G. Tatkowski et al.)

Figure 3.5 – The Detector Solenoid. (L. Bartoszek et al.)

4. TECHNICAL DESIGN OF THE TRANSPORT SOLENOID

The Transport Solenoid (Figure 4.1) consists of a series of wide aperture superconducting solenoid rings contained in two cryostats: the TSu cryostat and the TSd cryostat. Each of them has a chimney for superconducting leads, helium supply and return lines and instrument ports. Internal mechanical supports in each cryostat transmit forces to external mechanical supports that connect to the experiment enclosure structure. The Transport Solenoid does not have an iron return yoke. It is segmented into the following set of components:

- TS1: Straight section that interfaces with the Production Solenoid;
- TS2: Toroid section downstream of TS1;
- TS3: Straight section downstream of TS2. TS3u coils are in the TSu cryostat and TS3d coils are in the TSd cryostat;
- TS4: Toroid section downstream of TS3;
- TS5: Straight section downstream of TS4 that interfaces with the Detector Solenoid.

The TS1, TS2 and TS3u coils are assigned to the TSu cryostat; the TS3d, TS4 and TS5 coils share the TSd cryostat. Each cryostat will have its own superconducting link, feed box, power converter and extraction circuit.

All TS coils use the same conductor design and similar cooling schemes. The TSu unit and the TSd unit are nearly identical, so only the preliminary design of TSu will be presented.

4.1 TSU DESIGN

The TSu is shown in Figure 4.2 and includes the following design features:

- A single cryostat is employed to avoid gaps between coils and reduce complexity and cost;
- The coils are powered in series to minimize the number of leads and the complexity of the power and quench protection systems;
- The quench protection strategy is based on extracting most of the energy and delivering it to external dump resistors;
- Coils are preassembled and tested inside modules, with two coils per module in most cases, in order to reduce complexity during cold mass assembly;

- The mechanical support system consists of 17 supports including: six supports along the toroid main radius, four axial supports close to each end, and three gravity supports.

There is a gap between the TS3u and the TS3d coils as a result of the cryostat interfaces and the mechanical hardware necessary to actuate the rotating collimator and to insert the anti-proton window. To allow for a 220 mm gap, the inner radii of the TS3 coils have been increased to 465 mm, compared to inner radii of 405 mm for the remaining TS coils.

4.1.1 TSu Coil Design

The TS coils will be wound on collapsible mandrels and then inserted into aluminum shells (modules). The modules are assembled into a single cold mass and power unit. TS1 is a straight solenoid made of 3 coils with different outer diameters and separated by flanges. TS2 is a quarter of a toroid made of 18 coils. TS3u is a straight solenoid made of four coils. Figure 4.3 shows the distribution of these coils and Table 4.1 lists the main coil parameters.

The TSu cold mass is comprised of thirteen coil modules. Each module consists of bobbins made of 5083 - 0 Al. Most coil modules contain two wound coils inside the inner diameter. There are twenty-five coils total. Modules are bolted together at flanges to create a rigid structural unit. That unit is mounted in the cryostat using seventeen Inconel support rods, each of which have a spherical bearing at each end. The TS cold mass and cryostat components are shown in Figure 4.4.

Each module can house up to two coils, which are inserted into each end. A typical module can be seen in Figure 4.5. Each coil is wound in a collapsible mandrel over an aluminum strip, which is used to provide cooling for the coil and ground insulation (around the whole coil). Each module will be warmed up, allowing sufficient clearance (typically 1 mm) for coil insertion followed by a shrink fit. The modules can be fabricated by using a 5-axis industrial milling machine and a CNC lathe.

4.1.2 TSu Mechanical Design

As described above, the mechanical support system for TSu consists of seventeen support rods, made of Inconel 718: six radial supports (in the direction of the toroid main radius), eight axial supports and three gravity supports (Figure 4.6).

They are configured in such a way that the gravity supports bear only the weight of the cold mass (approximately 70 kN), while the remaining supports, which are considerably more robust, oppose the magnetic forces. Under normal operation, these forces tend to act toward the center of the toroid's axis of revolution in the horizontal plane, and total 1915 kN. [1]

Of the fourteen magnetic force supports, only the four axial supports at the downstream end are designed to resist both tension and compression. The remaining supports can resist only tension.

The magnetic supports attach at their cold ends to three reinforced bobbins on the cold mass and at their warm ends to three reinforced support rings on the cryostat. The warm support ends attach to the cryostat at nozzles. The radial supports lie in the horizontal plane; the axial supports are tipped outward 15 degrees from the toroid magnetic axis to prevent interference with the cryostat shell.

The cryostat sits on three rectangular boxes that attach to the floor in the experimental hall. These boxes are ultimately responsible for safely transferring the total magnetic force into the structure of the floor. Current thoughts on the alignment and cool down strategy are as follows:

- The cold mass is suspended on the gravity supports and adjusted so that the center of the toroid lies slightly below the centers of the PS solenoid and the TSd magnet. This vertical offset compensates for the small upward motion caused by contraction of the gravity supports on cool down. All other supports, including the downstream axial supports, are loose during this operation.
- When vertical alignment is achieved, the downstream axial supports (which can resist both tension and compression) are locked in place.
- The magnet is cooled down.
- After cool down, the tension-only supports are tightened just enough to remove any play.

Several load cases were simulated in order to study the TS coil displacements, the stresses in the coils, the structure and support rods during normal operation and various failure scenarios.

After cooldown (Figure 4.7) and during excitation (Figure 4.8) the von Mises stress in the coils is less than 25 MPa when stress concentration points due to the mesh are excluded. [1]

Table 4.2 shows the stress in the supports during normal operation (all magnets at operating current) and in case of failure scenarios (PS off or TSd off, with all other magnets on). These conditions will be avoided during normal operation; nonetheless, they will occur during test of TSu as stand-alone magnet and may occur in the case of a quench or the failure of adjacent systems. The radial supports see the highest tensile load during normal operation. The axial supports could see the highest tensile stresses or some compression if adjacent magnets fail. The Inconel 718 has an allowable stress of 531 MPa when cold, and the supports are designed to withstand the full load of these failure modes. In all conditions the stresses are below the allowable stress for Al-5083 (107 MPa at 4 K).

The global displacements (vector sum) of the cold mass for the cool down, energized and warm up load cases are shown in Figure 4.9 and Figure 4.10, respectively. The cool down and warm up displacements are given relative to the original warm position. The contribution from energizing is small compared to the

thermal contractions, and so is shown with the cool down load step subtracted out; in other words, the energizing deformations are relative to the cool down position. The cool down deformations are consistent with the lengths and thermal contractions of the cold mass. Because the downstream axial supports are fixed in axial translation, the motion of the downstream end of the cold mass is primarily that of the support contractions and the contraction of the last bobbin. This displacement amounts to about 4 - 5 mm. At the upstream end, total displacements of up to 20 - 21 mm occur. The deformations due to energizing, seen in Figure 4.10, show that displacements of about 1.8 mm will occur at approximately the midpoint of the toroidal arc. The axial and radial supports provide good stiffness against the attractive forces from the PS and TSd, with displacements of less than a millimeter at each end.

Table 4.3 lists the dimensions and materials for the various cryostat components. The TSu cryostat (Figures 4.11 – 4.12) consists of the components and systems listed below:

- Structural supports for the magnetic coils and the vacuum vessel;
- A 4.5 K cooling circuit;
- An 80 K thermal shield;
- A vacuum vessel with a warm bore;
- Interface to the PS cryostat;
- Interface to the proton beam line;
- Interface to the TSd cryostat and to the antiproton window;
- Interface to a cryogenic transfer line;
- Support for a Collimator in the warm bore at the PS interface;
- Support for a Rotatable Collimator in the warm bore at the TSd interface, and interface with rotating mechanism.

REFERENCES

[1] arXiv:1501.05241, *Mu2e Technical Design Report*, March 2015

Table 4.1 – TSu coil parameters. (L. Bartoszek et al.)

Coil #	Section	Coil Inner Radius [mm]	Coil Outer Radius [mm]	Coil Length [mm]	Number of layers	Number of turns per layer
1	TS1	405.00	423.13	164.96	5	16
2		405.00	434.00	257.75	8	25
3		405.00	444.88	154.65	11	15
4	TS2	405.00	448.50	175.27	12	17
5		405.00	448.50	175.27	12	17
6		405.00	448.50	175.27	12	17
7		405.00	463.00	175.27	16	17
8		405.00	463.00	175.27	16	17
9		405.00	463.00	175.27	16	17
10		405.00	463.00	175.27	16	17
11		405.00	466.63	175.27	17	17
12		405.00	466.63	175.27	17	17
13		405.00	466.63	175.27	17	17
14		405.00	466.63	175.27	17	17
15		405.00	470.25	175.27	18	17
16		405.00	470.25	175.27	18	17
17		405.00	470.25	175.27	18	17
18		405.00	470.25	175.27	18	17
19		405.00	470.25	175.27	18	17
20		405.00	477.50	175.27	20	17
21		405.00	448.50	175.27	12	17
22	TS3u	465.00	523.00	175.27	16	17
23		465.00	512.13	82.48	13	8
24		465.00	519.38	175.27	15	17
25		465.00	620.88	82.48	43	8

Table 4.2 – Stresses in the support rods under different power conditions. (L. Bartoszek et al.)

Support	Load Case Normal Operation [MPa]	PS Failed [MPa]	TSd Failed [MPa]
Upstream Axial 1	158	0	250
Upstream Axial 2	169	0	262
Upstream Axial 3	151	0	208
Upstream Axial 4	164	0	220
Downstream Axial 1	175	371	-121
Downstream Axial 2	176	374	-119
Downstream Axial 3	192	294	-62
Downstream Axial 4	204	309	-53
Upstream Radial 1	159	51	70
Upstream Radial 2	154	18	64
Downstream Radial 1	140	0	94
Downstream Radial 2	134	3	88
Central Radial 1	283	14	165
Central Radial 2	263	18	145
Gravity 1	24	24	24
Gravity 2	28	27	28
Gravity 3	20	19	20

Table 4.3 – TSu cryostat parameters. (L. Bartoszek et al.)

Cryostat Component	Dimension [mm]	Material
Vacuum Vessel Outer Shell	Outer diameter = 1625 Wall thickness = 19.05	Stainless Steel (316L)
Vacuum Vessel Inner Shell	Inner diameter = 500 Wall thickness = 15.875	Stainless Steel (316L)
Vacuum Vessel End Wall	Upstream = 19 Downstream thickness = 19	Stainless Steel (316L)
Thermal Shield Outer Shell	Outer diameter = 1286.9 Wall thickness = 6.35	Aluminum (6061 T6)
Thermal Shield Inner Shell	Inner diameter = 638.1 Wall thickness = 6.35	Aluminum (6061 T6)
Thermal Shield End Wall	Thickness = 6.35	Aluminum (6061 T6)

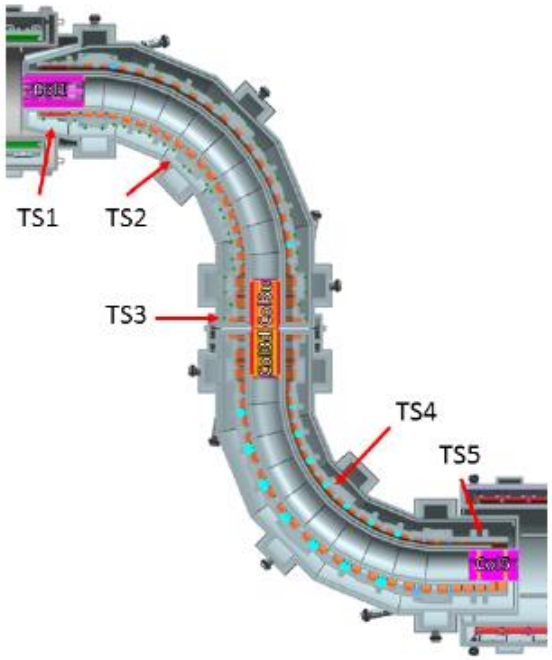

Figure 4.1 – The Transport Solenoid. (L. Bartoszek et al.)

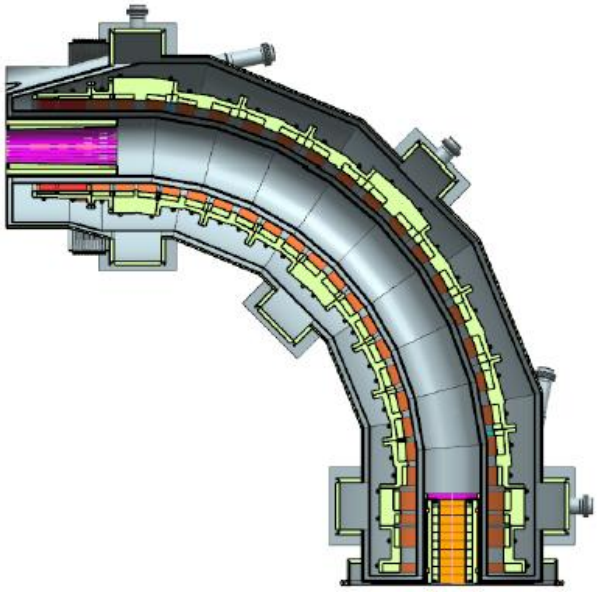

Figure 4.2 – Tsu cross section along the horizontal plane. (L. Bartoszek et al.)

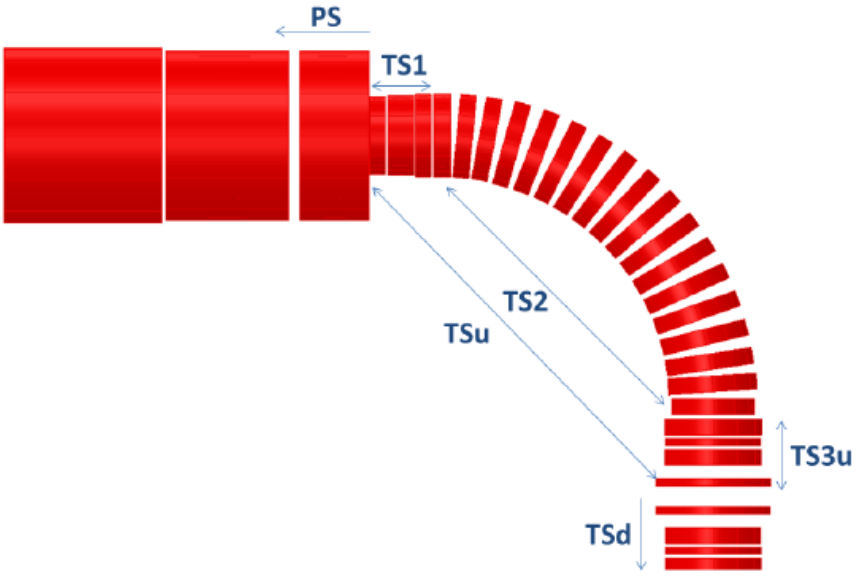

Figure 4.3 – TSu coil locations with respect to the adjacent magnets. (L. Bartoszek et al.)

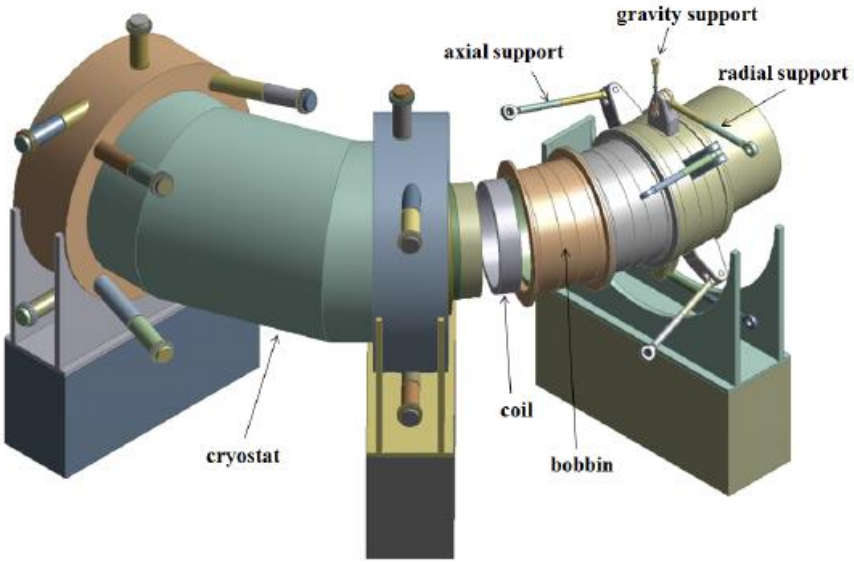

Figure 4.4 – TSu components (partial cutaway). (L. Bartoszek et al.)

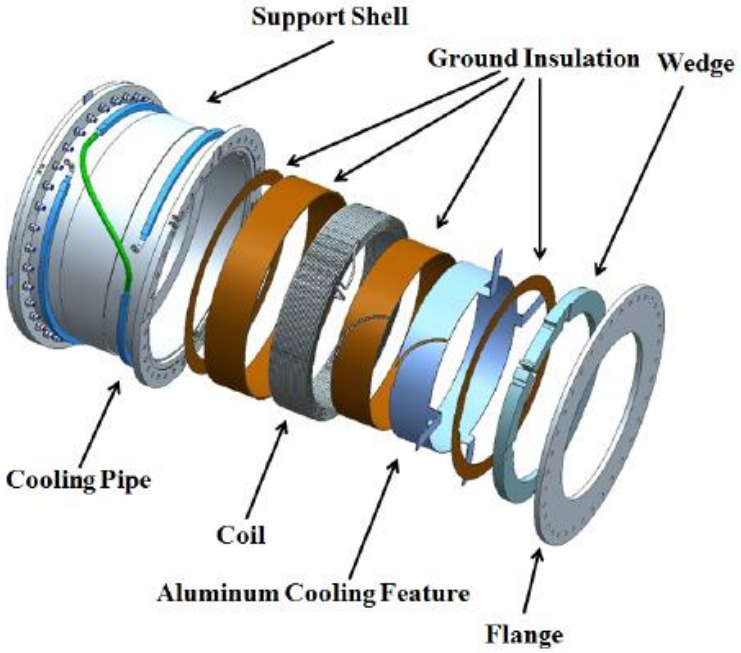

Figure 4.5 – A typical TS coil module. (L. Bartoszek et al.)

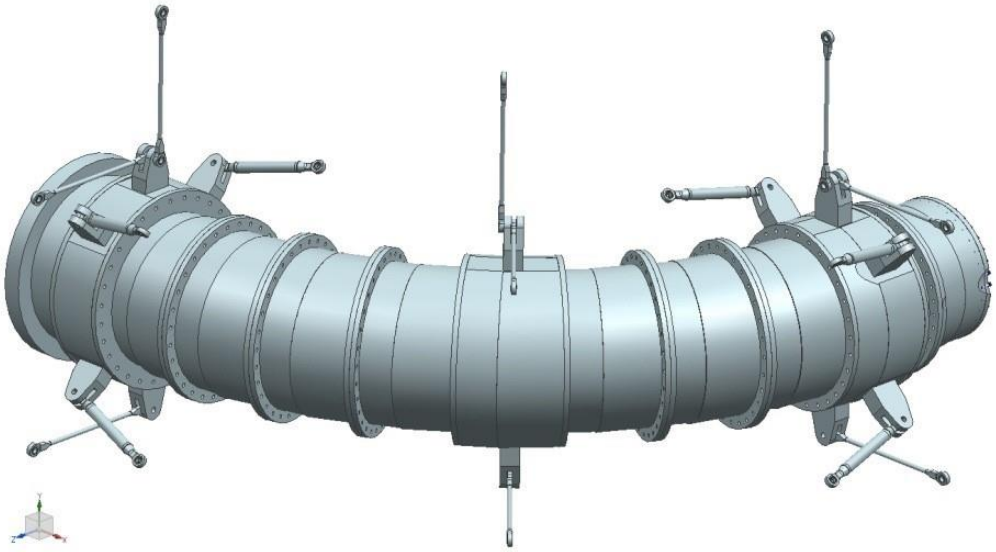

Figure 4.6 – TSu cold mass assembly. (L. Bartoszek et al.)

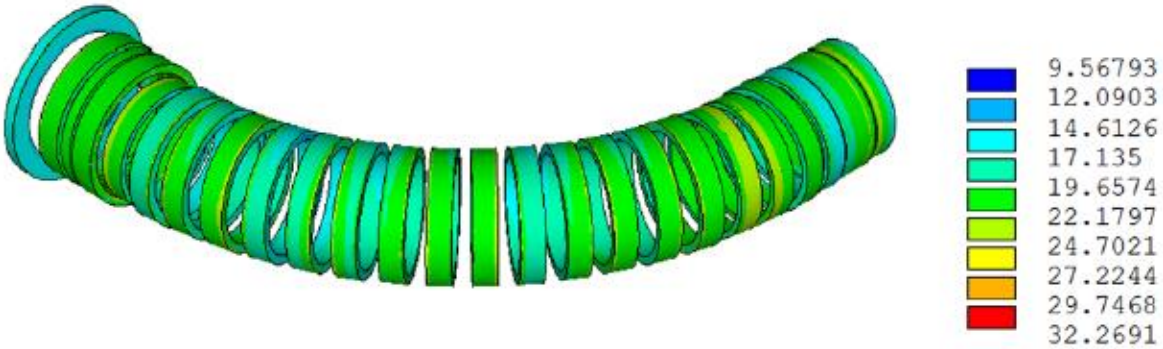

Figure 4.7 – Stresses (in MPa) in the TSu coils after cool down. (L. Bartoszek et al.)

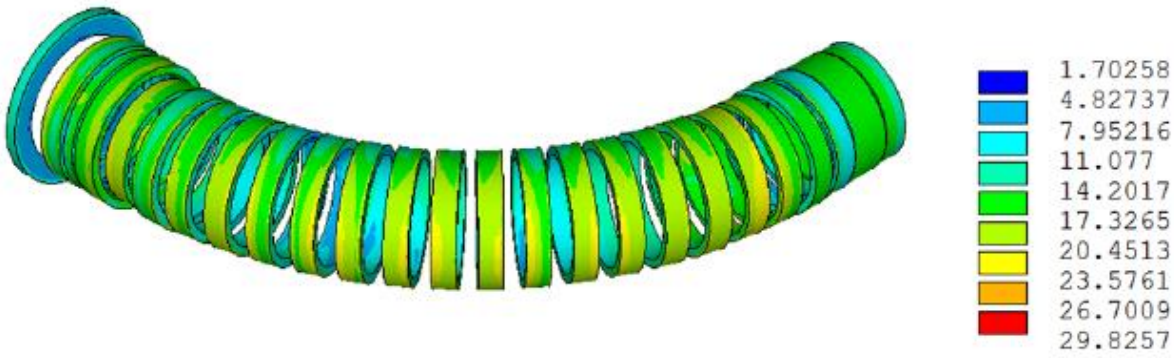

Figure 4.8 – Stresses (in MPa) in the TSu coils during excitation. (L. Bartoszek et al.)

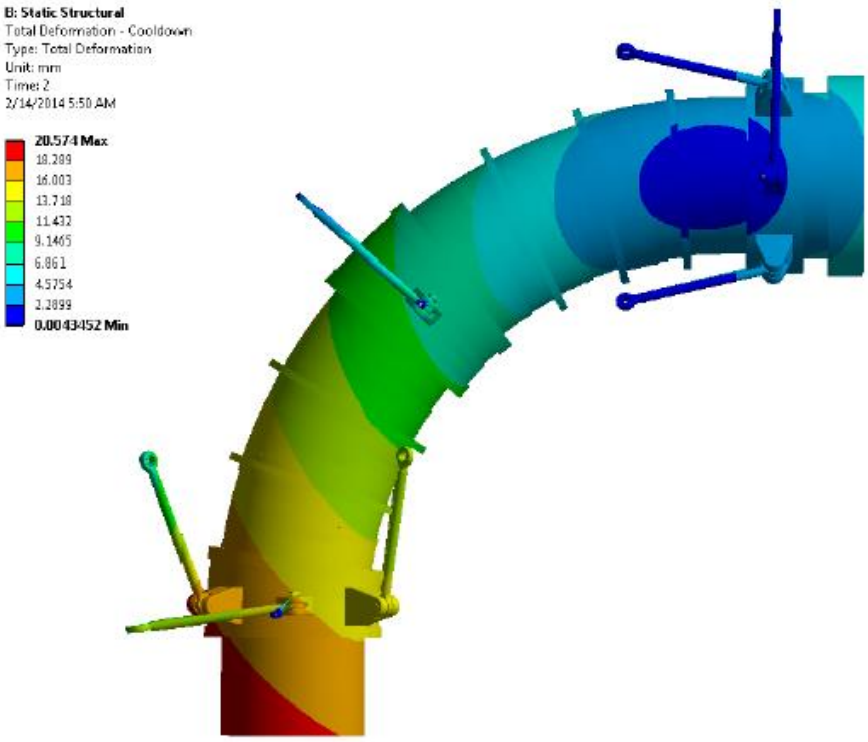

Figure 4.9 – Cold mass displacement after cool down. (L. Bartoszek et al.)

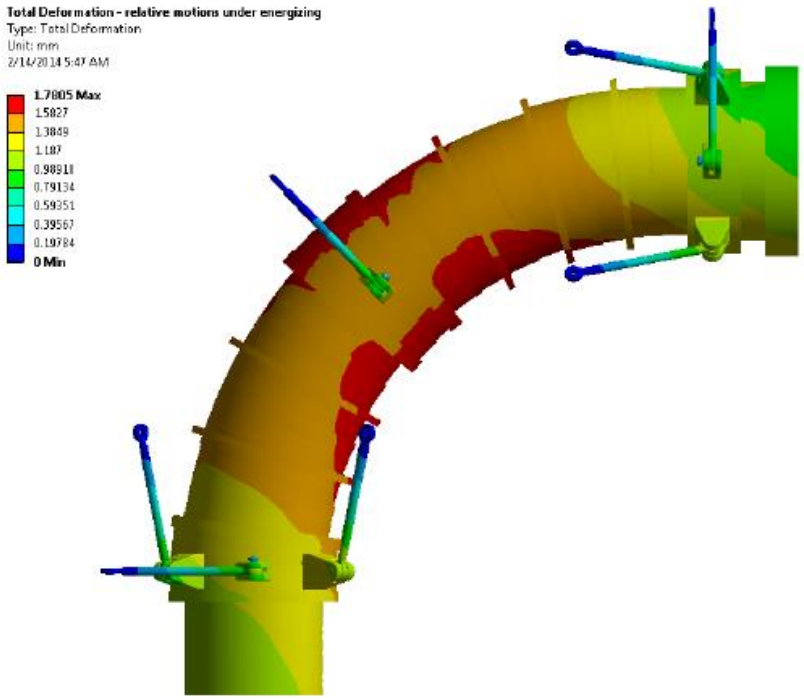

Figure 4.10 – Cold mass displacements during the energization relative to the cool down. (L. Bartoszek et al.)

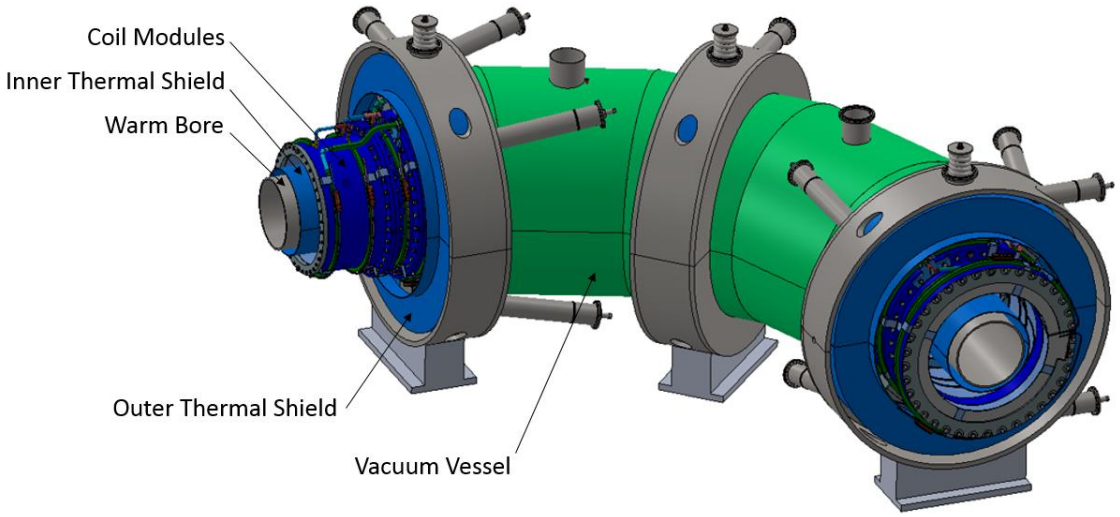

Figure 4.11 – Assembly of the TSu Cryostat. (T. H. Nicol)

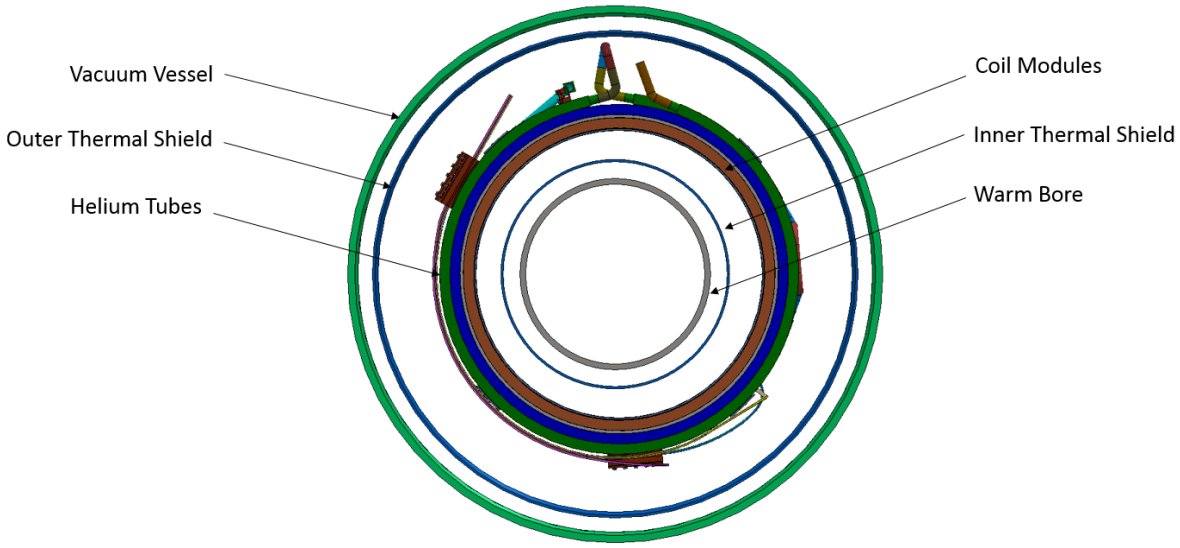

Figure 4.12 – Section of the TSu Cryostat.(T. H. Nicol)

5. Mu2e CRYOGENIC DISTRIBUTION LAYOUT

The superconducting solenoids require a cryogenic distribution system and supporting cryoplant for liquid helium and liquid nitrogen. The requirements for this system are described in Section 3.4.6. The scheme is to divide the solenoids into 4 semi-autonomous cryostats. Cryostats can be cooled down or warmed up independent of the state of the other cryostats. Each cryostat will require 4.5 - 4.7 K liquid helium as well as 80 - 90 K liquid nitrogen for the cryostat thermal shields. [2]

The liquid helium is provided to the experiment from two Tevatron-style satellite refrigerators. Approximately 152.4 m of outdoor transfer line separate the refrigeration facility from the Mu2e experimental hall. Upon entry into the Mu2e building, helium is routed through a large valve box known as the "distribution box" and into a helium storage dewar. After leaving the dewar, helium flow re-enters the distribution box, is split, and is routed to four separate valve boxes called "feedboxes" in four shorter and separate transfer lines. These feedboxes distribute helium to each of the four Mu2e cryostats independently. As mentioned previously, the TS magnet consists of both the TS-u and the TS-d, thus two separate feedboxes are used for the TS as a whole. Upon leaving the feedboxes, helium flows through another set of independent transfer lines down into the experimental pit where it can be delivered to each of the cryostats. After cooling each solenoid, helium is returned to the respective feedbox, back to the distribution box, and then finally to the cryogenic refrigeration facility. A generalized schematic of the helium distribution system can be seen in Figure 5.1.

Helium tubing is arranged in a helical configuration inside of each of the TS cryostats to consist of 25 horizontal-axis rings connected in series via crossover tubing; with 18 of the 24 rings having a 1 m diameter and 7 rings having a 1.25 m diameter (Figure 5.2). [2]

REFERENCES

[1] arXiv:1501.05241, *Mu2e Technical Design Report*, March 2015

[2] G. Tatkowski, S. Cheban, N. Dhanaraj, D. Evbota, M. Lopes, T. Nicol, R. Sanders, R. Schmitt, E. Voirin., *Forced two-phase helium cooling scheme for the Mu2e Transport Solenoid*, IOP Publishing Ltd

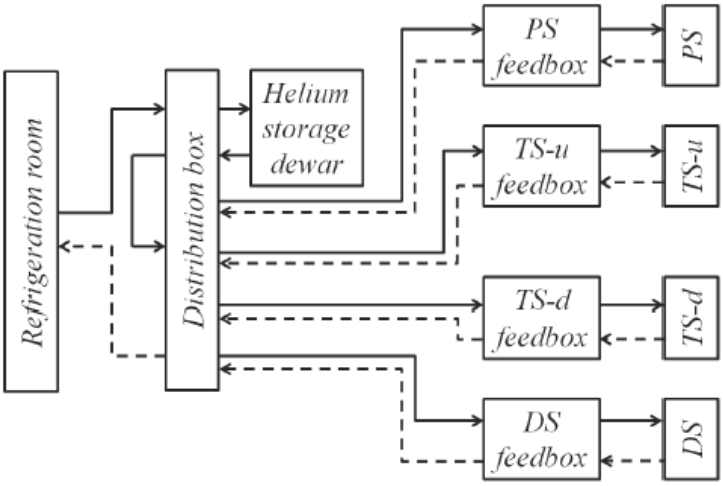

Figure 5.1 – Generalized helium flow schematic for the Mu2e experiment. (G. Tatkowski et al.)

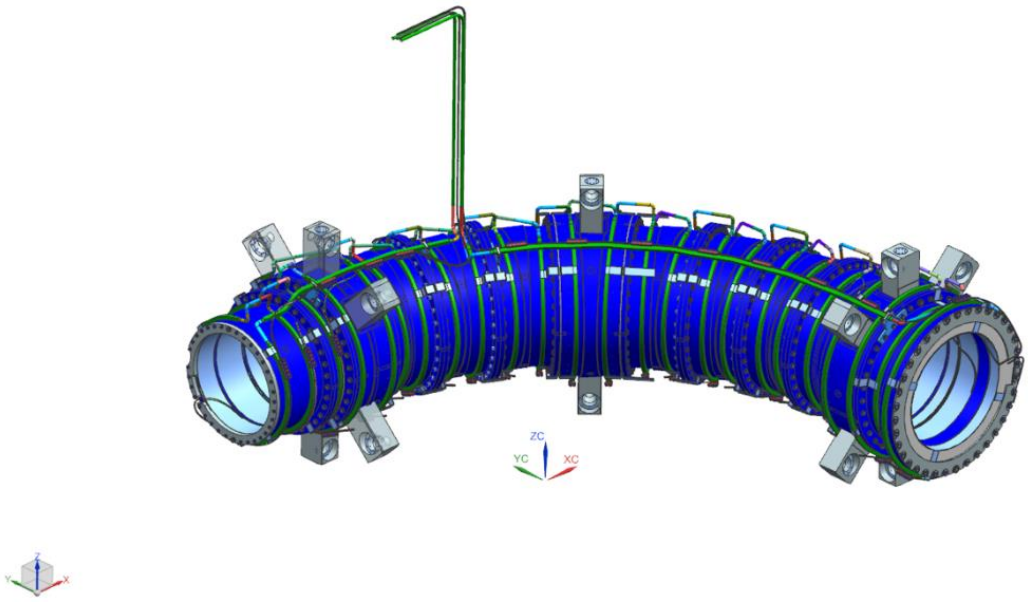

Figure 5.2 – TSu with cryostat and shielding removed (He cooling tubes shown in green). (T. H. Nicol)

6. STATUS OF ART: THE CRYOSTAT OF THE LHC INTERACTION REGION QUADRUPOLE MAGNET

6.1 INTRODUCTION

This chapter describes the LHC IR inner triplet quadrupole magnet cryostats designed and manufactured at Fermilab as part of the US-LHC collaboration, and includes discussions on the structural and thermal considerations involved in the development of each of the major systems.

The cryostat of a Large Hadron Collider (LHC) Interaction Region (IR) quadrupole magnet consists of all components of the inner triplet except the magnet assembly itself. It serves to support the magnet accurately and reliably within the vacuum vessel, to house all required cryogenic piping, and to insulate the cold mass from heat radiated and conducted from the environment. It must function reliably during storage, shipping and handling, normal magnet operation, quenches, and seismic excitations, and must be able to be manufactured at low cost.

There are four interaction points (IP) in the LHC, two high-luminosity and two low-luminosity IPs. Two magnet triplets are installed at each IP, one on each side, mirrored about the IP. Each triplet consists of four superconducting quadrupole magnets in three individual cryostats. The magnet assemblies are designated Q1, Q2a, Q2b, and Q3. Q2a and Q2b are assembled in to a single cryostat designated Q2.

The cryostat consists of the vacuum vessel, structural support system, insulation, thermal shield, and internal piping, that is, essentially all of the complete magnet components except the magnet assembly itself.

6.2 VACUUM VESSEL

The primary purpose of the vacuum vessel is to maintain the insulating vacuum environment for the cold mass and other internal piping. Additionally, it serves as a secondary containment in the event that an internal pipe or bellows failure releases cryogens inside the vacuum space. Finally, it provides the mechanical connection of the cold mass and piping to the accelerator tunnel floor. Each of the different quadrupoles, Q1 through Q3, requires a different vacuum vessel design, differing mostly in length. The dominant features however are the same. Each is constructed from rolled and welded sections of carbon steel pipe connected at heavier-walled reinforcing sections. The reinforcing sections are coincident with

the internal supports and transfer the weight and any mechanical loads to ground. The end flanges allow the insulating vacuum bellows to be "parked" over the outermost section while connecting the interconnect piping during installation in the tunnel. While ordinarily at room temperature, there are failure modes in which the vacuum vessel might experience lower operating temperatures for short periods. This could occur in the event of an internal failure that spills cryogens inside the vessel. It can also occur during a loss of insulating vacuum in which the vessel would be cooled by conduction from the cold mass and internal piping. These conditions require a material with higher fracture toughness at low temperature than normal construction-grade carbon steel. CERN has developed a material specification adopted by all collaborating laboratories that defines the toughness in terms of a minimum Charpy impact strength at –50 °C. Several domestic and foreign materials commonly used in the gas pipeline industry have been shown to meet this specification. Stainless steel and aluminum were considered for fabrication of these vessels early in the design process, but were dropped from consideration due to their high cost. Figure 6.1 shows a vacuum vessel assembly typical of those used in all LHC triplet magnets.

6.3 STRUCTURAL SUPPORT SYSTEM

The suspension system for this cryostat design represents a departure from systems used in similar magnets over the course of the last several years. SSC collider dipole cryostats, Tevatron low-beta quadrupole cryostats, and LHC arc dipole and quadrupole cryostats all employ composite support posts to support the weight of the cold assembly and to resist loads experienced during shipping and handling.

Early in the design phase of this project it was elected to place the He II heat exchanger outside the cold mass, but inside the vacuum vessel. This precluded the use of a support post scheme like these other magnets since it would have necessitated a vacuum vessel much larger in diameter than could have been transported into the LHC tunnel. Rather, it was decided to use a composite "spider" to support the cold mass and internal piping similar to structures used in the construction of cryogenic transfer lines. These structures are very strong and stiff in the radial direction and make good use of radial space. One of their weaknesses is in resisting axial loads encountered during shipping, handling, and cooldown. To better distribute these loads to all the support spiders, each pair of spiders has a set of axial tie-bars to tie them together. The tie-bars are made from Invar tube to minimize axial forces imposed on the supports during cooldown. Figure 6.2 illustrates a complete two-support suspension system including the support spider axial tie-bars. Q1 and Q3 cryostats use two supports and Q2 uses three. The cold mass is attached to the support at the bearing blocks located at the horizontal plane. These are Garlock-DU® sleeve bearings and

allow the cold mass to slide axially during cooldown to accommodate up to 14 mm of thermal contraction. The holes through the composite are clearance holes for the internal piping. The band around the outer perimeter is stainless steel and serves as an axial stiffener and as the thermal intercept when attached to the 70 K shield. The composite material is G-11CR.

6.4 MULTI-LAYER INSULATION SYSTEM

Multi-layer insulation is installed on the outside of the 70 K thermal shield, the cold mass, and around the internal helium pipes. The insulation is made in blankets consisting of alternating layers of 6 μm to 12 μm reflective Mylar and nylon spacer. The reflective aluminum coating thickness is 300 Å minimum on each side. The edges of the blankets are terminated with Velcro strips to ensure a good seal and easy, repeatable installation. The thermal shield uses two blankets of 15 layers each (15 layers of reflector, 14 layers of spacer) for a total of 30 reflective layers. The cold mass and internal piping each have single blankets of 10 reflective layers each. The expected performance of the thermal shield blankets based on earlier testing at CERN is 1.2 W/m^2 from 300 K to 70 K for all thirty layers. Similarly, the expected performance below 70 K is 50 to 100 mW/m^2 for ten layers [1]. Aluminized Mylar is almost transparent to infrared radiation below 20 K and so is nominally not effective on the cold mass or internal piping. It is used as protection from residual gas conduction in the event of a spoiled insulating vacuum and to reduce the transient heat load on the cold mass and piping in the event of a catastrophic loss-of-vacuum accident.

6.5 THERMAL SHIELD

A single thermal shield operating nominally at 70 K intercepts heat radiating from room temperature at the inside surface of the vacuum vessel. The temperature of the shield varies from about 60 K at the beginning of the triplet to 75 K at the end [1]. The shield consists of an aluminum shell surrounding the entire cold assembly, attached at the horizontal plane to two aluminum extrusions. The annular shell is constructed in segments to minimize the effects of bowing due to longitudinal temperature gradients during cooldown. Each extrusion has an aluminum to stainless steel transition welded to the end to allow welding to stainless steel interconnect bellows. Figure 6.3 illustrates a complete shield assembly. The holes through the shell allow the lugs on the support spider shown in Figure 6.2 to pass through for connection of the suspension system to the vacuum vessel.

6.6 INTERNAL PIPING

The internal piping consists of the He II heat exchanger, pumping line, cooldown line, and 4.5 K intercept lines. The He II heat exchanger is a corrugated copper tube inside a stainless steel shell. Helium in the outer shell is common with the magnet volume. It operates at 1.9 K and 1.3 bar. The inside of the corrugated copper operates at 1.8 K and 16 mbar [1]. The cooldown line is used only during initial filling of the magnet volume. The 4.5 K intercept lines will be used to cool absorbers located at each magnet interconnect and potentially any cold bore liner that might be installed at CERN. Pipe supports are positioned at both ends of the cold mass and at one or two places along the cold mass length. These supports position the ends of the pipes accurately to facilitate magnet interconnections and stiffen the ends to preclude interconnect bellows failure due to elastic instability caused by high internal pipe pressures. Since the pipe supports have no direct connection to anything other than the cold mass, there is no additional heat load associated with any of the internal piping. Figure 6.4 shows the completed internal assembly and includes the cold mass, suspension system, piping supports, and all the internal piping.

6.7 FINAL ASSEMBLY

After the assembly is completed to the stage shown in Figure 6.5, the multi-layer insulation blankets are installed over the cold mass and internal piping, the thermal shield and its insulation is installed, and the entire assembly is rolled into the vacuum vessel. The lower support blocks on each support spider contain a series of four cam rollers that allow the assembly to roll on the inside surface of the vacuum vessel. A close-up of this block and its associated rollers is shown in Figure 6.5. A rail system that is part of the final assembly tooling being fabricated for the production magnets helps to effect the transition from the assembly table to the vacuum vessel. A cable and winch system is used to pull the assembly into the vessel on the rollers shown in Figure 6.5. Guides installed inside the vacuum vessel and assembly tooling help to ensure the final alignment of the internal assembly with respect to the vacuum vessel. Mechanical fasteners are inserted into the support blocks from outside the vacuum vessel to anchor the internal assembly. Fine tuning the rough alignment mentioned earlier takes place at this stage through an adjustment mechanism built into the vacuum vessel penetrations. Finally, Conflat gaskets and flanges are installed to effect the final vacuum closure. Figure 6.6 shows a model of the completed first prototype assembly.

REFERENCES

[1] T. H. Nicol, C. Darve, Y. Huang, T. M. Page, *LHC Interaction Region Quadrupole Cryostat Design and Fabrication*, IEEE Transactions on Applied Superconductivity (Volume:12 , Issue: 1), August 2002

Figure 6.1 – Vacuum Vessel Assembly.(T. H. Nicol et al.)

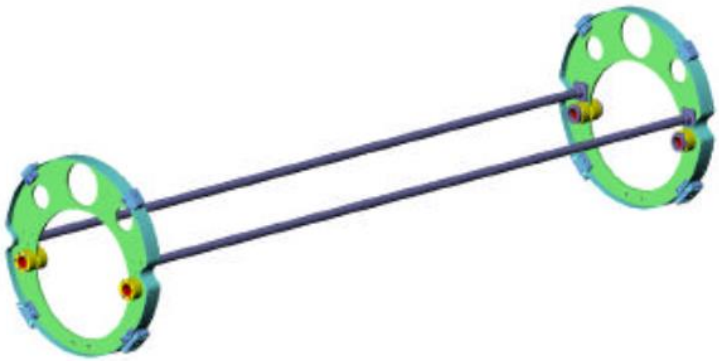

Figure 6.2 – Suspension System Assembly. (T. H. Nicol et al.)

Figure 6.3 – 70 K Thermal Shield Assembly. (T. H. Nicol et al.)

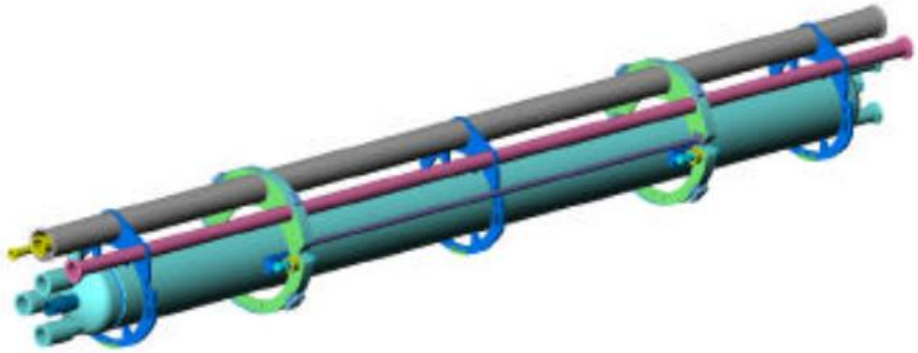

Figure 6.4 – Internal Piping Assembly. (T. H. Nicol et al.)

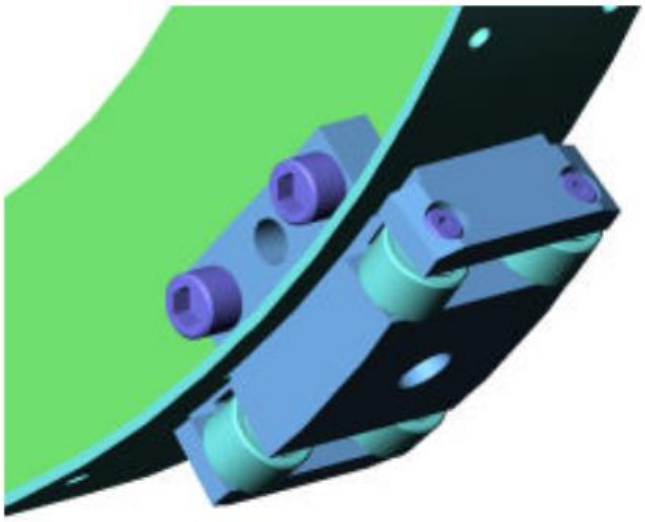

Figure 6.5 – Close – up for support block and rollers. (T. H. Nicol et al.)

Figure 6.6 – Complete Magnet Assembly. (T. H. Nicol et al.)

7. TSU THERMAL SHIELD COOLING SYSTEM

The purpose of the first part of this study is to analyze the Mu2e Transport Solenoid Thermal Shield cooling system.

The Thermal Shield is included in the TS cryostat (Figures 4.11 - 4.12), composed of a Vacuum Vessel, an Outer Thermal Shield, a Coil Module Assembly, an Inner Thermal Shield and a Warm Bore.

The Vacuum Vessel is the outermost cryostat component and serves to contain the insulating vacuum. In addition, it functions as the major structural element to which all other systems are ultimately attached to the floor, through three supports. It is made by austenitic stainless steel (316L), maintained at room temperature (T = 293.15 K) and it has an inner diameter equal to ID = 1605.95 mm and a thickness t = 19.05 mm. [1]

The pressure inside it is equal to $p = 1.3 \times 10^{-4}$ Pa.

Cryogenic vessels are generally made of austenitic stainless steels. The austenitic structure does not undergo any ductile-to-brittle transition at cryogenic temperature. The 304-type (18Cr8Ni on a Fe basis) is the most common grade in use. Its low-carbon steel version 304L ($C \leq 0.030\%$), is preferred because of its enhanced corrosion resistance and ductility in welded structures. Austenite is non-magnetic, but for special applications where a fully austenitic and stable structure is sought even at cryogenic temperatures (high field quality in superconducting magnets, for instance), 316-type steels and, in particular, 316LN should be used. The 316LN type is also commonly used in bellows convolutions owing to its formability and ductility. [2]

The physical properties of the 316L stainless steel at room temperature are shown in Table 7.1.

Inside the Vacuum Vessel are the Outer and the Inner Thermal Shield (Figures 7.1 - 7.2), both made by 6061 T6 aluminum alloy. The physical properties of the 6061 T6 aluminum alloy are summarized in Table 7.2. Thermal shields must be composed by high thermal conductivity material. Copper and aluminum are the materials of choice, preferentially as alloys for their better mechanical properties and manufacturability while still preserving good thermal conductivity. Pure coppers are preferred only for demandingly high thermal conductivity where temperature homogeneity matters. Aluminum alloys are by far the most used materials in thermal shields for accelerator cryostats. They are used for inner vessels (particularly 6061 and 5083), in heat-conducting baffles and shields (1100 and 3003), and in extrusions and piping (6063 and 6061). Aluminum is characterized by light weight (2768 kg/m^3), relatively high thermal conductivity (1100 and 6063), moderate allowable design stress (68 to 70 MPa for 6061 and

5083), and a low average modulus of 69 GPa. Aluminum alloys are clean in vacuum service and have a low rate of hydrogen diffusion. Clean aluminum has low thermal radiation emissivity, typically from 1 to 4 or 5%, depending on surface temperature and condition. [2]

The Outer and the Inner Thermal Shield are maintained at a temperature T = 80 K and a pressure $p = 1.3 \times 10^{-4}$ Pa. The first has an inner diameter equal to ID = 1280.55 mm and a thickness equal to t = 6.35 mm. The second has an inner diameter equal to ID = 631.75 mm and a thickness equal to t = 6.35 mm. [1]

The Thermal Shield acts as a radiative barrier, as well as an intermediate cooling stage between the cold cavity and outer vacuum chamber. The shield will be actively cooled using a series of tubes which also provide a structural skeleton.

Between the Outer and the Inner Thermal Shield is the Coil Module Assembly, at a temperature T = 4 K (Figure 7.3).

Eventually, inside the Inner Thermal Shield, is the Warm Bore, made by 316L stainless steel (see Table 7.1 for its physical properties) and maintained at room temperature (T = 293.15 K) and pressure $p = 1.3 \times 10^{-4}$ Pa. It has an inner diameter equal to ID = 500 mm and a thickness t = 15.875 mm. [1]

In Table 7.3 are summarized the information given above.

Since inside the Cryostat the pressure is equal to $p = 1.3 \times 10^{-4}$ Pa, the thermal exchange between all the its components is mainly due to radiation, which in literature, for the cryogenic systems, is called “residual gas conduction”. From now on, so, this expression will be used to describe the thermal exchange inside the facility.

Thermal radiation protection of the Thermal Shield and the coil module assembly is enhanced by the use of MLI (multilayer insulation protection).

It is based on the principle of multiple radiation reflection obtained by inserting reflective layers between the warmer radiating surface (typically the vacuum vessel) and the colder surfaces (thermal shield or cold surface of the internal device).

In practice, reflective layers are packed in blankets, and thermal contact between adjacent layers would be inevitable; for this reason, the reflective layers are interleaved with insulating spacers, as schematically shown in Figure 7.4, limiting thermal conduction.

MLI in accelerator cryostats generally consists of aluminized thin polyethylene films as reflective surfaces, and paper, glass-fiber, or polyester insulating nets as insulating spacers.

The efficiency of MLI also depends on the practical aspects of how it is mounted. The packing density of the layers plays an important effect. Figure 7.5 shows schematically that with increasing packing density,

the solid conduction contribution increases. There is a somewhat optimal packing density, which can be found between 15 and 25 layers per centimeter.

MLI efficiency also depends on practical implementation rules. The ideal packing density should be preserved after installation of the blankets. When mounted in horizontal accelerator cryostats, MLIs tend to be compressed by their weight on the top part of the thermal shields, whereas it tends to be looser at the bottom. A good rule is to check that an acceptably correct packing remains after installation. Also, when preassembled MLI blankets are to be mounted around circular geometries, one should include in the design the larger circumferential dimension of the outermost layers with respect to innermost ones.

Differential thermal contractions between the MLI and its support should be also considered to preserve the correct packing when cold.

Finally, a typical mistake is to stack too many layers in a reduced space between warm and cold surfaces, ending up with unwanted thermal conduction shorts. A good rule is to leave a minimum gap of at least a few centimeters between the warm surface and the outermost MLI layer.

The choice of the ideal number of MLI layers is not a straightforward one, and is very much dependent on the materials employed (film material and thickness, single or double-aluminisation, aluminisation thickness, type of spacers, etc.); a general tendency is to introduce as many layers as can possibly fit in the available space, sometimes resulting in thermal contact shorts, but also in an increase of material and assembly costs.

At Fermilab, an optimal and cost-effective solution was chosen for the MLI blankets of the thermal shield (Figure 7.6): 30 reflective layers of Mylar.

Radiation heat load from the ~ 300 K Vacuum Vessel can be greatly reduced by multi-layer superinsulation. The exact number is difficult to calculate. Previous detectors have quite large range in specify the heat load. CMS [6] gives 5 W/m^2, while CDF [7] gives 0.86 W/m^2. D0 [8] and ATLAS [9] have some value in between (2.736 and 1.268 W/m^2, respectively).

Fesmire and Augustynowicz [10] of Cryogenics Test Laboratory of NASA Kennedy Space Center gave an example of test in which 30 layers Jehier, 0.01 m thick were placed between 80 K and 300 K. The resulted apparent conductivity is 0.034 mW/m-K.

R.J.Powers et al. [11] did tests at Fermilab for SSC 12 m dipole magnet cryostat model. They got apparent conductivity of 0.062 mW/m-K for aluminized plastic films with fiberglass mat as spacer material (18 layers/cm).

For the TS cryostat, the heat load considered are:

- for the Thermal Shield, two equal to 1.5 W/m^2 , one entering from the external surface of the Outer Thermal Shield, and the other entering from the internal surface of the Inner Thermal Shield;
- for the Coil Module Assembly, two equal to 0.15 W/m^2, one entering the external surface and the other entering the internal one.

These heat loads are shown in Figure 7.7.

The Thermal Shield and the Coil Module Assembly have to be cooled down through a series of tubes that contains a cryogenic fluid. For the Thermal Shield it was chosen the liquid nitrogen and for the Coil Modules the liquid helium. The nitrogen properties at the normal boiling point are shown in Table 7.4.

Neglecting the Coil Module Assembly study, that is not the subject matter of the research, this first part of paper has the purpose to analyze the Thermal Shield cooling system under two different aspects.

In Section 7.1 is presented a steady state thermal analysis, intended to establish how many tubes are required to maintain the Thermal Shield at a temperature of T = 80 K.

Although, Section 7.2 describes a transient thermal analysis, utilized in order to determine how long the Thermal Shield takes to cool down.

7.1 STEADY STATE THERMAL ANALYSIS

7.1.1 Thermal Shield Model

The Steady State Thermal Analysis of the Thermal Shield was developed in Ansys Workbench 17.1.

As first attempt, it was used the model in Figures 7.8 – 7.9, that represented the entire TSu, without the support rods.

However, using a Dell Optiplex 980 (Processor: Intel ® Core ™ 7 CPU 870 @2.93 GHz 2.93 GHz; RAM: 8.00 GB), this first model turned out to be too heavy for the simulations, so it was decided to use a simplified model.

As we can see in Figure 7.8, the Outer Thermal Shield was composed by eighteen different sections: nine on the upper half of the body and the other nine in the lower one. In the same way, Figure 7.9 shows that the Inner Thermal Shield was divided into ten sections in the upper half of the body and ten sections in the lower one. The presence of these sections increased the calculation time, so it was decided to delete all of them, representing the Outer and Inner Thermal Shield as two cylinders.

Moreover, we were able to represent just half of these cylinders, cutting them along the horizontal center line. As described in Section 4.1.2, three gravity support rods were placed on the upper half of the Outer Thermal Shield, adding a heat load on it, so it was decided to analyze the upper half of the shield, in order to be conservative. The obtained model is shown in Figure 7.10 and its section in Figure 7.11.

It was decided to connect four tubes on the Outer Thermal Shield and two on the Inner Thermal Shield by welding (Figure 7.12 – 7.13). All the tubes were made by 6061 T6 aluminum alloy (see Table 7.2 for its physical properties), had an inner diameter equal to ID = 22 mm and a thickness of t = 1.7 mm. The two Outer Thermal Shield "external" tubes were located at 20° from the horizontal plane, the "internal" ones at 60° and the two of the Inner Thermal Shield at 45°.

7.1.2 Heat Loads on the Thermal Shield

Inside the Thermal Shield was a pressure equal to $p = 1.3 \times 10^{-4}$ Pa.

In order to run the simulations, it was necessary to specify the heat loads and the temperatures operating on the shields.

An uniform temperature equal to T = 293 K, representing the room temperature, was imposed on the body.

Two heat fluxes equal to 1.5 W/m^2 were represented, one entering from the external surface of the Outer Thermal Shield, and the other entering from the internal surface of the Inner Thermal Shield.

The Outer Thermal Shield was connected to the Vacuum Vessel through six radial supports (in the direction of the toroid main radius), eight axial supports and three gravity supports (as described in Section 4.1.2).

Clearly, since we represented just half of the shield, in our model we had the holes for just three radial supports, four axial supports and the three gravity supports. They were clearance holes and were the holes where the rods had to be mechanically connected, so their inner surface represented the heat exchange surface between the Vacuum Vessel at T = 293.15 K and the Thermal Shield, that we wanted to cool down at T = 80 K.

It was necessary to take into account the thermal effect that these connections had on the Thermal Shield. To do this, we imposed an uniform heat flow equal to 2 W on the holes inner surfaces of the three gravity support rods and an uniform 5 W heat flow on the ones of the radial and axial support rods.

The heat flows just described are shown in Figure 7.14.

Eventually, to cool down the thermal shield, on the inner surfaces of the tubes was imposed an uniform temperature of T = 80 K. The nitrogen inside the tubes was actually a two-phase fluid, with a pressure

p = 1.36 bar and a quality equal to x = 0.06 at the entrance of the TSu and a pressure p = 1.01 bar and a quality equal to x = 0.6 at the end of it. The nitrogen properties are shown in Table 7.4. [12]

7.1.3 Selection of the Mesh for the Finite Element Analysis

To obtain the mesh size sensitivity, six different mesh densities were tested, using the temperature average as the benchmark.

The results are shown in Table 7.5.

To reduce the computation time, it was chosen the grid with 491761 elements, since with the successive mesh densities the maximum change of the mean temperature was equal to 10^{-3} K.

On the chosen mesh, three different body sizing were inserted, to obtain a thicker grid on the smaller bodies:

- one for the tubes, with the element size equal to 5×10^{-3} m;
- one for the G10 insulating layers, with the element size equal to 5×10^{-3} m;
- one for the rest of the model, with the element size equal to 5×10^{-2} m.

In Figures 7.15 – 7.16 – 7.17 is shown the mesh, respectively, on the entire body, on the Inner Thermal Shield and on the tubes and the insulating layer. Moreover, in Figure 7.18 is a detail of the mesh on a tube.

We obtained a single unit curved structured grid on the Inner Thermal Shield, the tubes and the G10 layers, and an unstructured grid on the Outer Thermal Shield, with tetrahedral elements.

The unstructured grid is more flexible from the geometric point of view than the structured one, so it is more appropriate to treat the complicated geometries of industrial interest. Moreover, it is an adaptive grid, so it is easy to increase automatically the number of elements on the areas of interest. On the other side, it has a higher complexity than the structured grid.

7.1.4 Analyses

As described in Section 7.1.1, the initial configuration consisted of four tubes on the Outer Thermal Shield (two located at 20° from the horizontal plane, the other two at 60°) and two on the Inner Thermal Shield (at 45° from the horizontal plane), so the first simulation took into account this model.

The following simulations considered various scenarios, each one with a different combination of the six tubes.

First of all, we tried to figure out the most convenient number of tubes for the Outer Thermal Shield, keeping unchanged the tubes configuration on the Inner Thermal Shield. Therefore, with two tubes on the inner shield, we studied on the outer one the cases with:

1. Tubes at 20° only;
2. Tubes at 60° only;
3. One 20° tube only;
4. One 60° tube only.

The second part of the work was to analyze how many tubes were necessary on the Inner Thermal Shield, keeping unchanged the scheme that turned out to be the most efficient for the Outer Thermal Shield.

So, using the best system for the outer shield, we simulated for the inner one the cases with:

1. One tube only;
2. No tubes.

7.1.5 Results

Using the mesh with 491761 elements, the result was, for each simulation, the distribution of temperature created inside the Thermal Shield.

Using two tubes on the Inner Thermal Shield, we analyzed the cases with:

1. All four tubes

   As shown in Figure 7.19, on the Outer Thermal Shield the temperature reaches its minimum (T = 80 K) near the tubes, increases on the three reinforced support rings and becomes maximum (T = 80.579 K) near the gravity and radial support rods. Although, as we can see from Figure 7.20, the minimum temperature of T = 80 K is uniformly maintained on the entire Inner Thermal Shield.

2. Tubes at 20° only

   The temperature distribution on the Outer Thermal Shield is shown in Figure 7.21. It reaches its minimum (T = 80 K) near the tubes and increases in the sections far from them. The maximum (T = 81.094 K) is reached near the gravity and radial support rods. Although, as shown in Figure 7.22, the temperature on the Inner Thermal Shield is equal to T = 80 K, except for its two extremities, which have a temperature of T = 80.242 K.

3. Tubes at 60° only

   As shown in Figure 7.23, on the Outer Thermal Shield the temperature reaches its minimum (T = 80 K) near the tubes, increases far from them and becomes maximum (T = 80.721 K) near the radial rods of the two reinforced support rings placed at the extremities of the shield. Although, as we can see from Figure 7.24, the minimum temperature of T = 80 K is uniformly maintained on the entire Inner Thermal Shield.

4. The “external” tube at 20° only

The temperature distribution on the Outer Thermal Shield is shown in Figure 7.25. It reaches its minimum (T = 80 K) near the "external" tube at 20° and increases in the sections far from it, until it reaches its maximum (T = 82.545 K) on the opposite side of the shield, the "internal" one. Although, as shown in Figure 7.26, the temperature on the Inner Thermal Shield is maintained at about T = 80 K.

5. The "internal" tube at 20° only

   As shown in Figure 7.27, on the Outer Thermal Shield the temperature reaches its minimum (T = 80 K) near the "internal" tube at 20°, increases far from it and becomes maximum (T = 83.626 K) on the opposite side of the shield, the "external" one. Although, as we can see from Figure 7.28, the minimum temperature of T = 80 K is uniformly maintained on the entire Inner Thermal Shield.

6. The "external" tube at 60° only

   The temperature distribution on the Outer Thermal Shield is shown in Figure 7.29. It reaches its minimum (T = 80 K) near the "external" tube at 60° and increases in the sections far from it. It reaches its maximum (T = 81.578 K) on the opposite side of the shield, the "internal" one. Although, as shown in Figure 7.30, the temperature on the Inner Thermal Shield is maintained at about T = 80 K.

7. The "internal" tube at 60° only

   As shown in Figure 7.31, on the Outer Thermal Shield the temperature reaches its minimum (T = 80 K) near the "internal" tube at 60°, increases far from it and becomes maximum (T = 82.121 K) on the opposite side of the shield, the "external" one. Although, as we can see from Figure 7.32, the minimum temperature of T = 80 K is uniformly maintained on the entire Inner Thermal Shield.

Eventually, using two tubes at 60° on the Outer Thermal Shield, we analyzed, for the Inner Thermal Shield, the cases with:

8. The "external" tube only

   The temperature distribution on the Outer Thermal Shield is shown in Figure 7.33. It reaches its minimum (T = 80 K) near the tubes at 60° and increases in the sections far from it. It reaches its maximum (T = 80.722 K) near the radial rods of the two reinforced support rings placed at the extremities of the shield. Although, as shown in Figure 7.34, the temperature on the Inner Thermal Shield is equal to T = 80 K on the "external" side and increases until T = 80.24 K, moving to the "internal" one.

9. The "internal" tube only

As shown in Figure 7.35, on the Outer Thermal Shield the temperature reaches its minimum (T = 80 K) near the tubes at 60°, increases far from it and becomes maximum (T = 80.731 K) near the radial rods of the two reinforced support rings placed at the extremities of the shield. Although, as we can see from Figure 7.36, the temperature on the Inner Thermal Shield is equal to T = 80 K on the "internal" side and increases until T = 80.324 K, moving to the "external" one.

10. No tubes

    As shown in Figure 7.37, the temperature on the entire Outer Thermal Shield does not change much and is maintained between T = 80 ÷ 80.484 K. Although, as shown in Figure 7.38, the temperature on the Inner Thermal Shield is equal to T = 81.939 K on the extremities of the shield and increases until its maximum of T = 86.79 K, moving to the shield's center.

7.1.6 Discussion of the results

The first result is that the Thermal Shield turned out to be almost isothermal, with a temperature of about T = 80 K over all its surfaces.

It was possible to identify one of the proposed schemes as the most efficient.

In the case of two tubes on the Inner Thermal Shield and two tubes at 60° on the Outer Thermal Shield the mean temperature was T = 80.3605 K, while in the initial configuration with four tubes on the Outer Thermal Shield it was T = 80.2895 K. So, the difference between the two values was equal to 0.1 K.

Considering the Simulations 1 – 7, the scheme with two tubes on the Inner Thermal Shield and two tubes at 60° on the Outer Thermal Shield turned out to be the most efficient and this is confirmed by the fact that, with this layout, the tubes were closer to the outer shield's section with more heat loads.

From Simulations 8 – 10 (described in Section 7.1.5), realized with two tubes at 60° on the Outer Thermal Shield, the system with only the "external" tube at 45° on the Inner Thermal Shield turned out to be the most efficient. Its mean temperature was T = 80.361 K, so the difference between it and the one of the layout with two tubes on the inner shield was equal to 10^{-4} K.

In conclusion, the analysis allowed to reduce the number of tubes at three for each half of the Thermal Shield (two at 60° on the outer shield and the "external" one at 45° on the inner shield), saving money and time in the construction process.

The chosen cooling scheme is shown in figure 7.39.

However, it is necessary to specify that, in order to be conservative, the number of tubes should be increased at least at five, but this lies outside the subject of this paper.

7.2 TRANSIENT THERMAL ANALYSIS

7.2.1 Thermal Shield Model

The aim of the transient thermal analysis of the Thermal Shield was to analyze the time necessary to the Thermal Shield to cool down until a temperature of T = 80 K.

To do this, it was chosen to work on the cooling system that turned out to be the most efficient for the steady state analysis: the one composed by two tubes at 60° from the horizontal plane on the Outer Thermal Shield and one "external" tube at 45° on the Inner Thermal Shield.

As for the steady state analysis model (Section 7.1.1), the Thermal Shield was represented as two concentric half cylinders, with the holes for the mechanical connections of the support rods.

To reduce the computation time, the G10 layers were suppressed. Their dimensions were really small, compared to the shield's one, so a very thick mesh on them would have been necessary. Moreover, since the G10 was an insulating material, its thermal contribution was so great that the others would not have been relevant for the analysis.

The model is shown in the Figures 7.40 – 7.41.

The analysis was conducted in Ansys Workbench 17.1.

7.2.2 Heat Loads on the Thermal Shield

At the beginning of the analysis, the Thermal Shield was at room temperature, so, on the body, was imposed an uniform initial temperature T = 293.15 K. The pressure on it was equal to $p = 1.3 \times 10^{-4}$ Pa.

The same heat loads of the steady state analysis were maintained. Therefore, in the same way, were considered:

- an uniform 5 W heat flow on each axial and radial support;
- an uniform 2 W heat flow on each gravity support;
- an uniform 1.5 W/m^2 heat flux, entering from the outer surface of the Outer Thermal Shield;
- an uniform 1.5 W/m^2 heat flux, entering from the internal surface of the Inner Thermal Shield.

A brief clarification about the heat loads is necessary. The heat loads represented the thermal exchange between the Thermal Shield and the close cryostat sections that were at a higher temperature, which were the Vacuum Vessel and the Warm Bore (T = 293.15 K). This made sense for the steady state analysis, where the Thermal Shield was supposed to be at a temperature of T = 80 K. However, since the aim of the transient thermal analysis was to cool down the Thermal Shield, its initial temperature was equal to T = 293.15 K, so, in reality, there was no thermal exchange between it, the Vacuum Vessel and the Warm

Bore, at the beginning of the analysis. The thermal exchange started with the Thermal Shield cooling down and the heat loads grew up during its development. Anyway, we considered unvaried the values of the heat loads written above for the whole analysis, in order to study the worst case scenario. In fact, in this way, we simulated the cool down of the Thermal Shield with the maximum heat load on it. This means that the real time needed to cool down the shield will never exceed the one obtained from the simulation.

To cool down the shield, an uniform temperature of T = 80 K was imposed on the inner surfaces of the three tubes.

Moreover, it was necessary to take into account also the thermal contribution of the convection between the liquid nitrogen inside the tubes and the wall of the tubes themselves. The nitrogen inside the tubes was actually a two-phase fluid, with a pressure p = 1.36 bar and a quality equal to x = 0.06 at the entrance of the Tsu and a pressure p = 1.01 bar and a quality equal to x = 0.6 at the end of it. [12]

The heat transfer coefficient for it (provided by the Cryogenic Division) was equal to h = 105.1 W/m^2-K. The nitrogen properties are shown in Table 7.4.

7.2.3 Selection of the Mesh for the Finite Element Analysis

To study the mesh size sensitivity, we decided to simulate 3 hours of cooling down, using a step end time equal to 10800 s. It is usually possible to choose also the time step, a parameter that indicates the time step between two measurements done by the software. To run these simulations, an arbitrary time step of 160 s was chosen.

Leaving unchanged these parameters, we realized five simulations, imposing two different body sizing on the body, in order to obtain on the tubes a thicker mesh than on the shield.

To compare the different mesh densities, the temperature average was chosen as the benchmark.

The body sizing chosen, the number of elements and the mean temperatures are summarized in Table 7.6.

To avoid the increasing of the computational time, the mesh with 106031 elements was chosen. It has a single unit curved structured grid on the Inner Thermal Shield and an unstructured grid on the Outer Thermal Shield and the tubes, with tetrahedral elements. The characteristics of this kind of grids are briefly described in Section 7.1.3.

In Figures 7.42 – 7.43 – 7.44 is shown the mesh, respectively, on the entire body, on the Inner Thermal Shield and on the tubes. Moreover, in Figure 7.45 is a detail of the mesh on a tube.

7.2.4 Selection of the Time Step

In the transient thermal analysis, in addition to the mesh size sensitivity, a similar analysis is necessary for the time step.

Six simulations were conducted, using the mesh described in Section 7.2.3. For all of them, it was chosen to simulate 10 hours of cooling down, so the step end time was equal to 28800 s.

The temperature average obtained from the analyses was chosen as the benchmark.

The results are listed in Table 7.7.

To avoid the increasing of the computational time, it was chosen to run the simulation with a time step equal to 160 s.

7.2.5 Results

In Figures 7.46 – 7.47 – 7.48 are shown, respectively, the profiles of the maximum temperature, the minimum temperature and the two together. In the first 13 h 33 min (48800 s) the maximum and the minimum temperatures converge to the temperature T = 80 K.

In Figures 7.49 – 7.50 the distributions of temperature on the Outer and Inner Thermal Shield are shown. On the Outer Thermal Shield the temperature reaches its minimum (T = 79.993 K) near the nitrogen tubes, increases in the areas far from them and reaches the maximum (T = 80.714 K) near the holes of the radial support rods. On the Inner Thermal Shield, the temperature reaches its minimum near the nitrogen tube and increases in the areas far from it, until a temperature T = 80.313 K on the "internal" side of the shield.

7.2.6 Discussion of the results

The transient thermal analysis on the Thermal Shield shows that the time needed to cool down the shield until a temperature of about T = 80 K is equal to t = 48800 s, that is 13 h 33 min.

At the beginning, we expected to have an initial increase of the global maximum temperature, due to the heat loads. Whereas, as we can see from Figure 7.46, since the heat loads were very small, the temperature started immediately to decrease. Therefore, the maximum temperature profile properly decreased until it almost converged with the minimum temperature one.

In particular, in the first three hours (12000 s) the biggest temperature decrease occurred, from 293.15 K to 100 K. It is shown in Figure 7.51. After this, the temperature decrease became slower.

At the end of the cooling down, the maximum temperature reached was T = 80.702 K. In Section 7.1.5 are listed the maximum temperatures obtained from the steady state thermal analysis. In particular, the one for the model utilized also for the transient thermal analysis, is the one of the simulation number 8 and it is

equal to T = 80.722 K. Therefore, considering the maximum temperature obtained from the steady state analysis, the difference between it and the one obtained from the transient thermal analysis is equal to 2×10^{-2} K. Moreover, the time needed to cool down the shield is acceptable, according to the Fermilab Technical Division.

REFERENCES

[1] arXiv:1501.05241, *Mu2e Technical Design Report*, March 2015

[2] J. G. Weisend, *Handbook of Cryogenic Engineering*, edited by CRC Press, July 1998

[3] N. Templeton, T. Jones, S. Pattalwar, K. Marinov, A. May, E. Nolan, G. Burt, K. Artoos, R. Calaga, O. Capatina, T. Capelli, F. Carra, R. Leuxe, C. Zanoni, A. Ratti, *Design of the Thermal and the Magnetic Shielding for the LHC High Luminosity Crab-Cavity upgrade*

[4] T. H. Nicol, *SSC Collider Dipole Cryostat*

[5] arXiv:1502.02950v1, *Cryostat Design*, contribution to the CAS-CERN Accelerator School: Superconductivity for Accelerators, Erice, Italy, edited by R. Bailey, 24 April – 4 May 2013

[6] Ph. Fazilleau, Ph. Bredy, and B. Levesy, *CMS Coil Thermal Shields Final Design*, IEEE Transactions on Applied Superconductivity, Vol. 12, No. 1, March 2002

[7] R. Fast, J. Grimson, R. Kephart, E. Leung, L. Mapalo, R. Wands, R. Yamada, H. Minemura, S. Mori, M. Noguchi, R. Yoshizaki, K. Kondo, *Design Report for an Indirectly Cooled 3-m Diameter Superconducting Solenoid for the FERMILAB Collider Detector Facility*, October 1982

[8] J. Brzezniak, R.W. Fast, K. Krempetz, A. Kristalinski, A. Lee, D. Markley, A. Mesin, S. Orr, R. Rucinski, S. Sakla, R.L. Schmitt, R.P. Smith, B. Squires, R.P. Stanek, A.M. Stefanik, A. Visser, R. Wands, R. Yamada, *Conceptual Design of a 2 Tesla Superconducting Solenoid for the Fermilab D0 Detector Upgrade*, May 1994

[9] ATLAS Collaboration, *ATLAS Magnet Project TDR Volume 4: Central Solenoid*, April 30, 1997

[10] J. E. Fesmire, S. D. Augustynowicz, *Cryogenic Thermal Insulation Systems*, 16th Thermal and Fluids Analysis Workshop, Orlando, Florida, August 9, 2005

[11] R. J. Powers, J. D. Gonczy, J. Otavka, R. C. Niemann, A. Szymulanski, J. L. Tague, *5cm, No Iron SSC Dipole 12m Model Cryostat Thermal Performance*, September 1985

[12] G. Tatkowski, J. Catalanell, *Mu2e Nitrogen Process "Steady State" Flow Diagram*, 2014

Table 7.1 – Physical properties at room temperature of the 316L stainless steel. (G. Di Caprio)

Specific Heat [J/kg-K]	500
Thermal Conductivity [W/m-K]	15
Thermal expansion (20 – 100 °C) [K^{-1}]	16.0 x 10^{-6}
Elastic Modulus [GPa]	200
Electrical Resistivity [Ω-mm^2/m]	0.75
Density [g/cm^3]	8.0

Table 7.2 – Physical properties at room temperature of the 6061 T6 aluminum alloy. (ASM)

Specific Heat [J/kg-K]	900
Thermal Conductivity [W/m-K]	170
Thermal expansion [µm/m/K]	23
Melting Point [°C]	582 (solidus) – 652 (liquidus)
Elastic Modulus [GPa]	69
Electrical Resistivity [µΩ/cm]	3.99
Density [g/cm^3]	2.7

Table 7.3 – Cryostat's components characteristics. (L. Bartoszek et al.)

Component	**Material**	**Intern Diameter [mm]**	**Thickness [mm]**	**Temperature [K]**	**Pressure [Pa]**
Vacuum Vessel	Austenitic Stainless steel (316L)	1605.95	19.05	293.15	1.3 x 10^{-4}
Outer Thermal Shield	Aluminum (6061 T6)	1280.55	6.35	80	1.3 x 10^{-4}
Inner thermal shield	Aluminum (6061 T6)	631.75	6.35	80	1.3 x 10^{-4}
Warm Bore	Austenitic Stainless Steel (316L)	500.00	15.875	293.15	1.3 x 10^{-4}

Table 7.4 – Saturated – Liquid Property of nitrogen at 1 atm. (J. G. Weisend)

Normal boiling point [K]	77.36
Critical temperature [K]	126.1
Critical pressure [MPa]	3.39
Triple-point temperature [K]	63.2
Triple-point pressure [kPa]	12.85
Density [kg/m^3]	807.3
Latent heat [kJ/kg]	199.3
Specific heat [kJ/kg-K]	2.05
Viscosity [µPa-s]	158
Thermal conductivity [mW/m-K]	139.6

Table 7.5 – Mesh Size Sensitivity for the steady state thermal analysis.

Number of Elements	**Mean Temperature [K]**
136296	80.240
144671	80.270
176556	80.282
491761	80.2895
632648	80.288
756413	80.289

Table 7.6 – Mesh Size Sensitivity for the transient thermal analysis.

Number of Elements	**Tubes Element Size [m]**	**Shield Element Size [m]**	**Mean Temperature [K]**
78201	5×10^{-2}	2×10^{-1}	95.995
87180	4×10^{-2}	1×10^{-1}	92.055
106031	3×10^{-2}	7×10^{-2}	93.215
265302	5×10^{-3}	5×10^{-2}	93.25
572441	2.5×10^{-3}	2.5×10^{-2}	93.26

Table 7.7 – Time Step Sensibility for the transient thermal analysis.

Time Step [s]	**Mean Temperature [K]**
1280	80.5455
640	80.455
320	80.421
160	80.4065
80	80.3995
40	80.3965

Figure 7.1 – TSu Outer Thermal Shield. (T. H. Nicol)

Figure 7.2 – TSu Inner Thermal Shield. (T. H. Nicol)

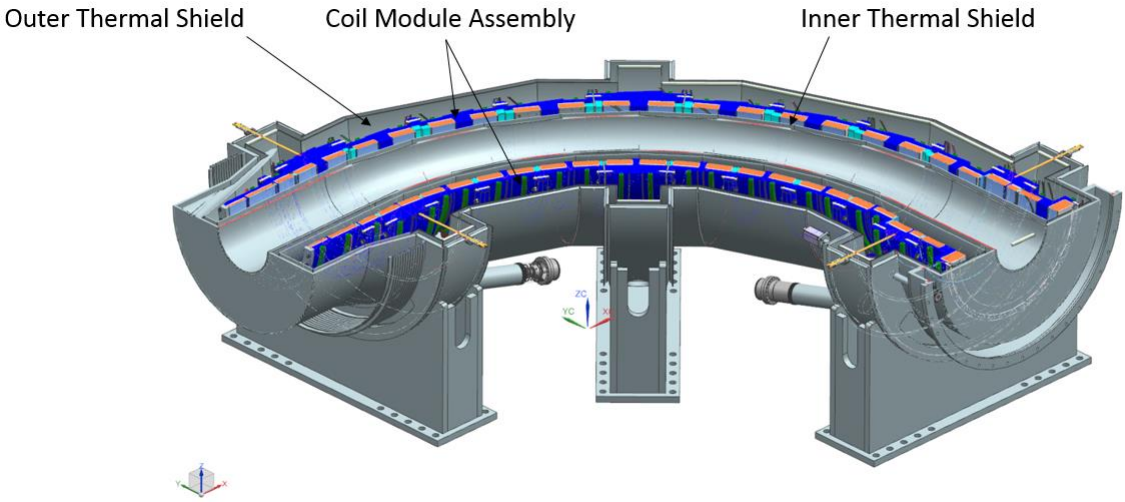

Figure 7.3 – TSu cross section. (T. H. Nicol)

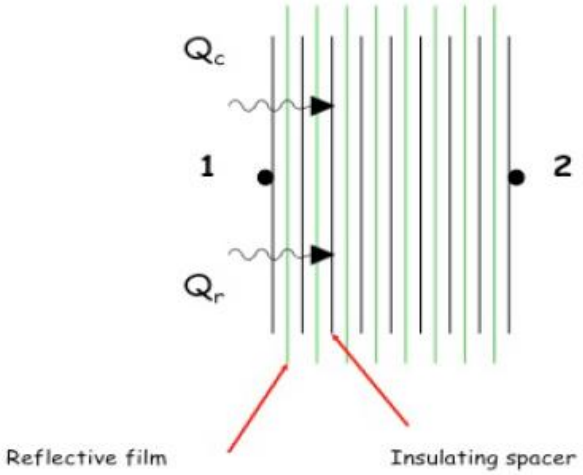

Figure 7.4 - MLI structure, showing reflective layers interleaved with insulating spacers.(V. Parma et al.)

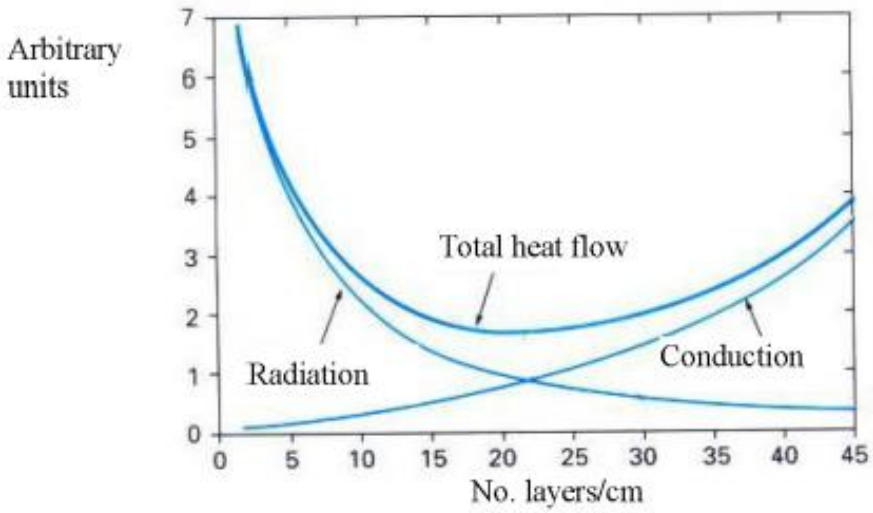

Figure 7.5 - Total heat flow as a function of MLI packing density. (V. Parma et al.)

Figure 7.6 - MLI stack in a blanket. (V. Parma et al.)

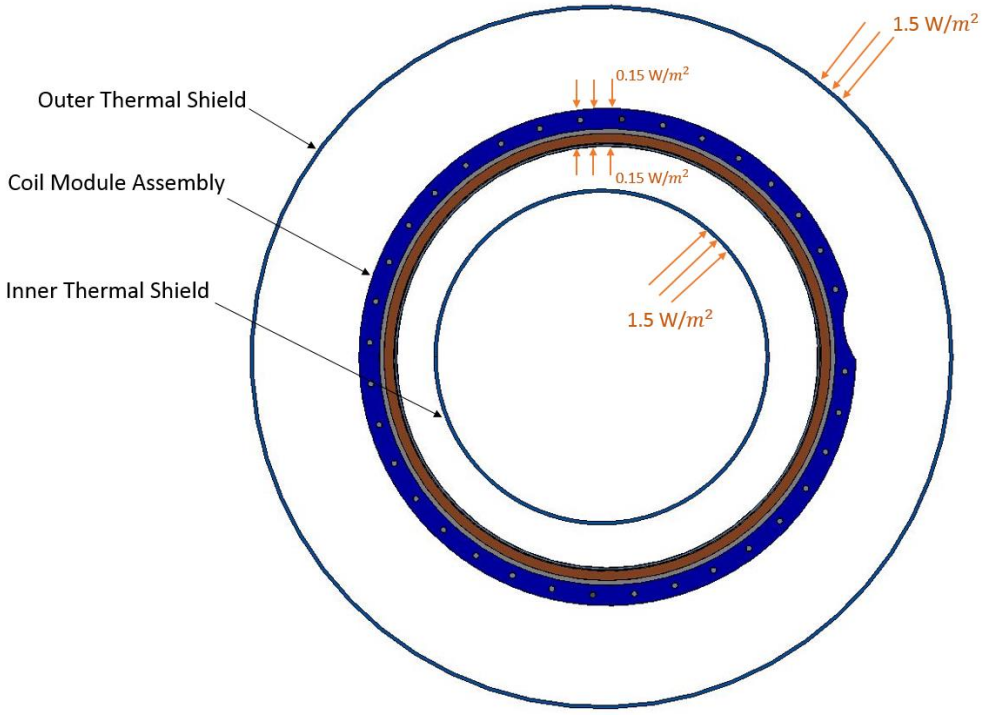

Figure 7.7 – Thermal Shield heat loads. (T. H. Nicol)

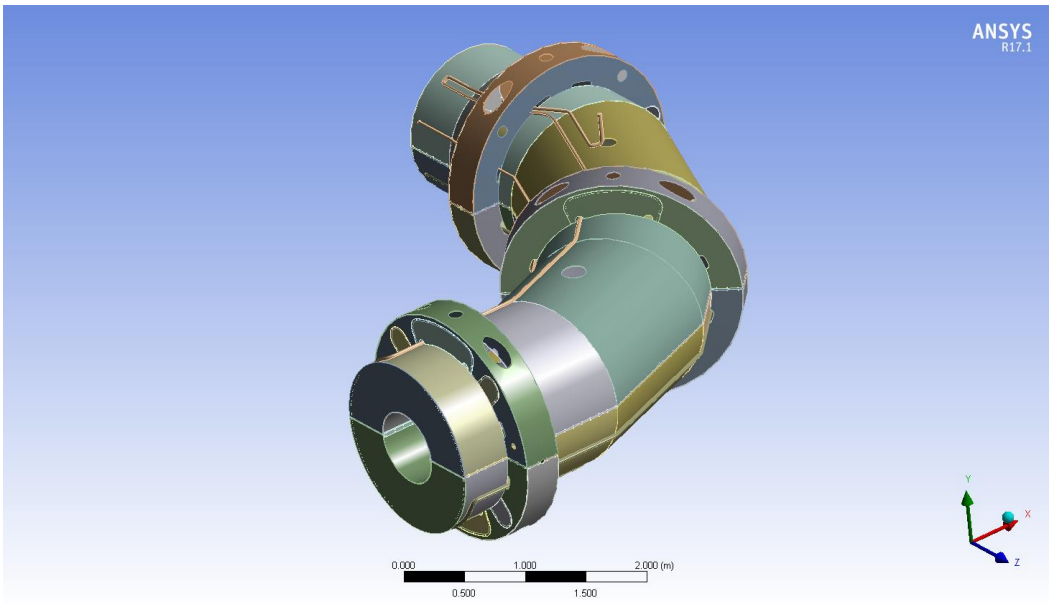

Figure 7.8 – Model of the Outer Thermal Shield.

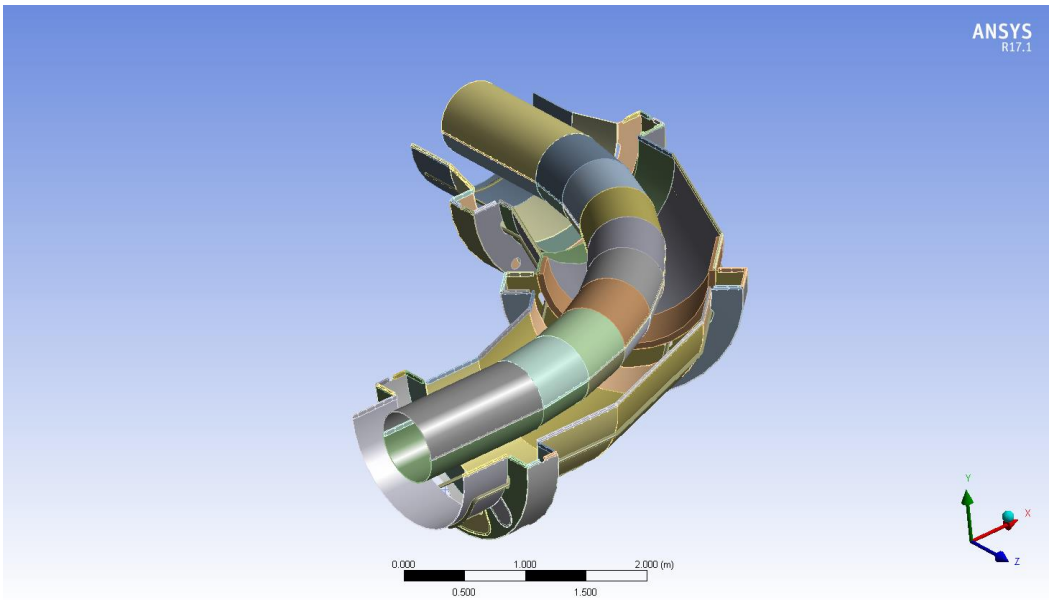

Figure 7.9 – Model of the Inner Thermal Shield.

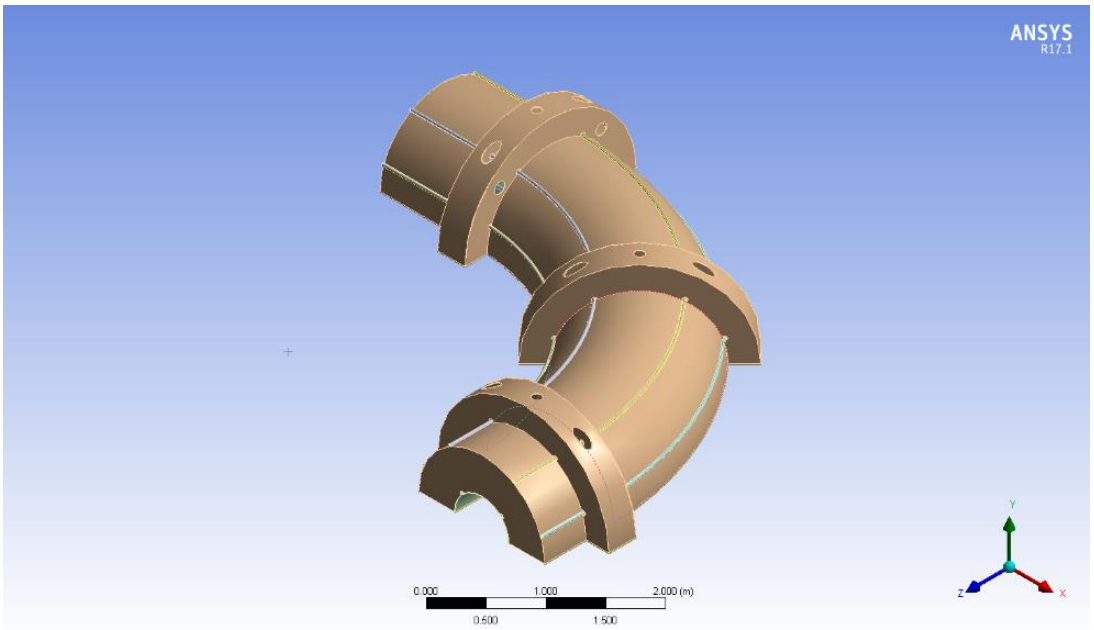

Figure 7.10 – Simplified model of the Thermal Shield for the Steady State Thermal Analysis.

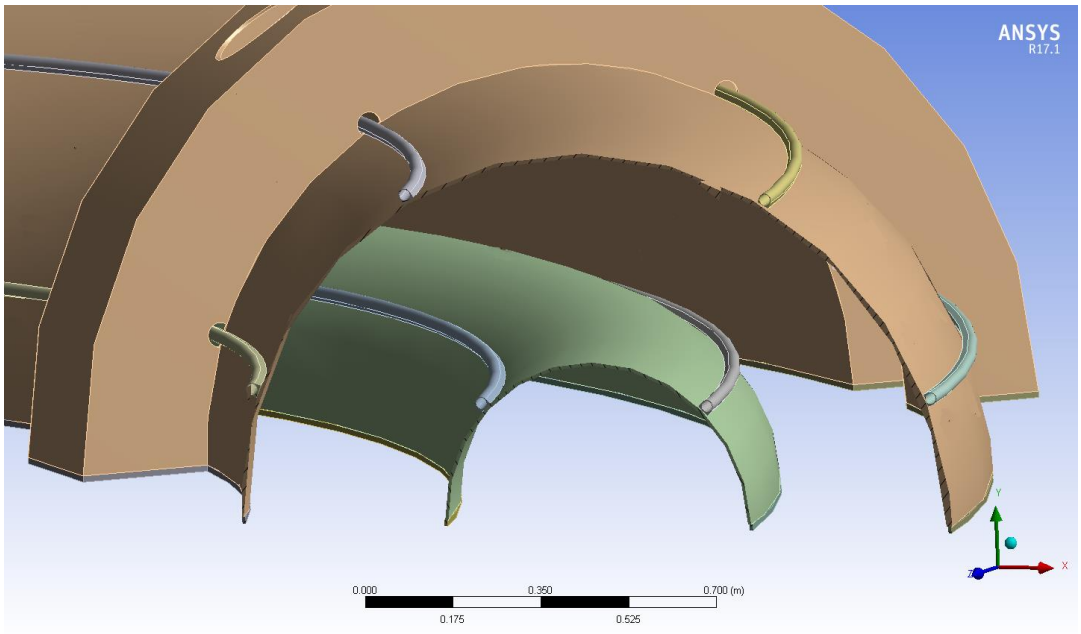

Figure 7.11 – Thermal Shield section.

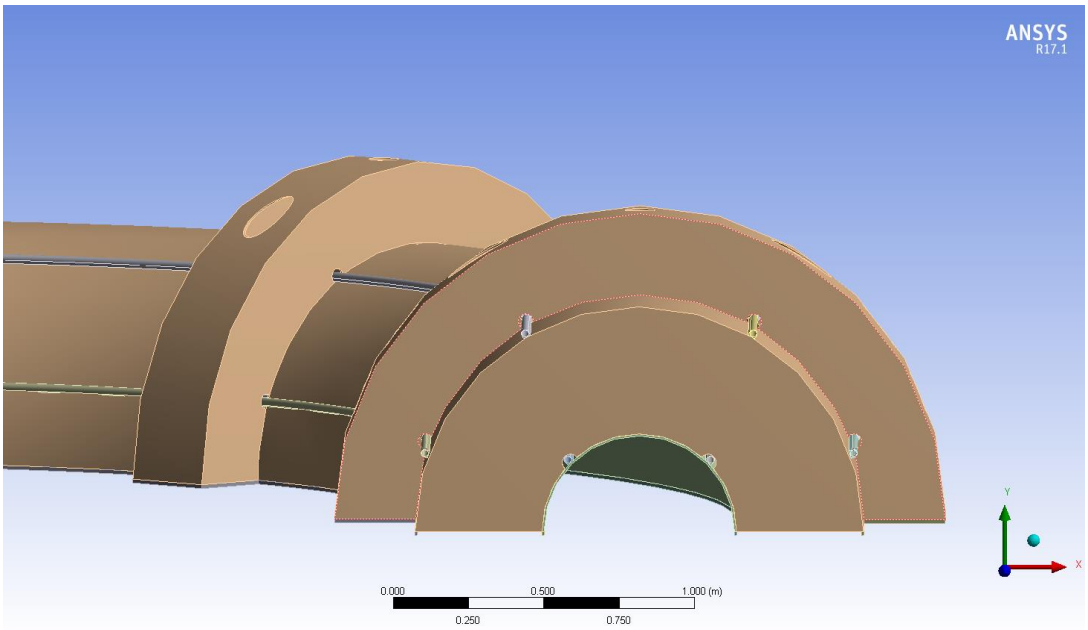

Figure 7.12 – Arrangement of the tubes on the Thermal Shield for the Steady State Thermal Analysis.

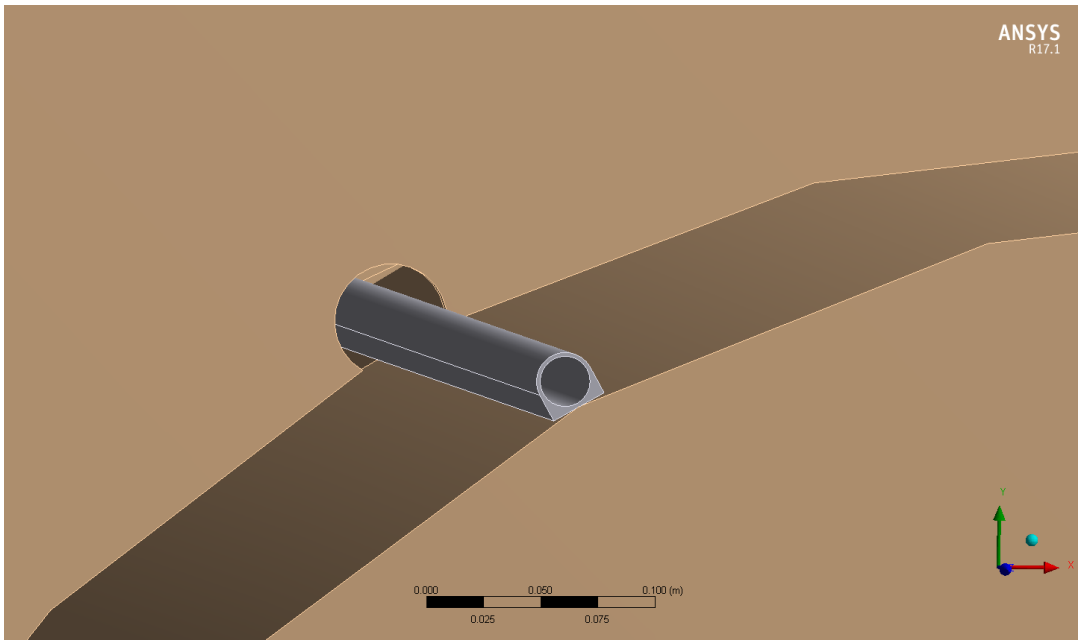

Figure 7.13 – Detail of a tube connected to the shield by welding.

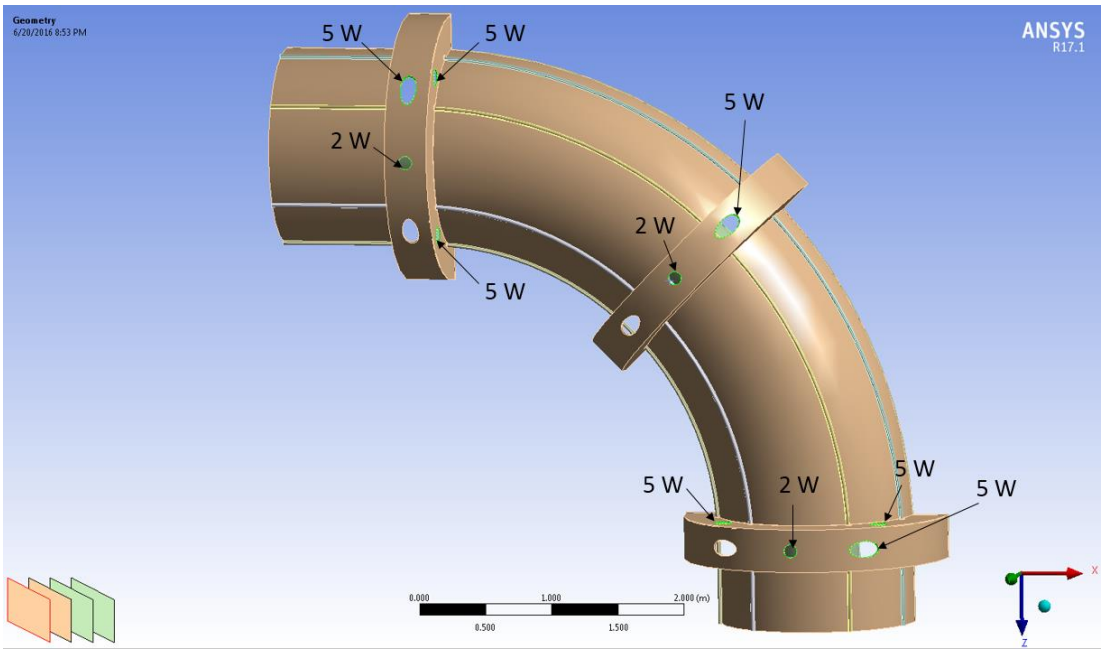

Figure 7.14 – Heat flow on the Outer Thermal Shield.

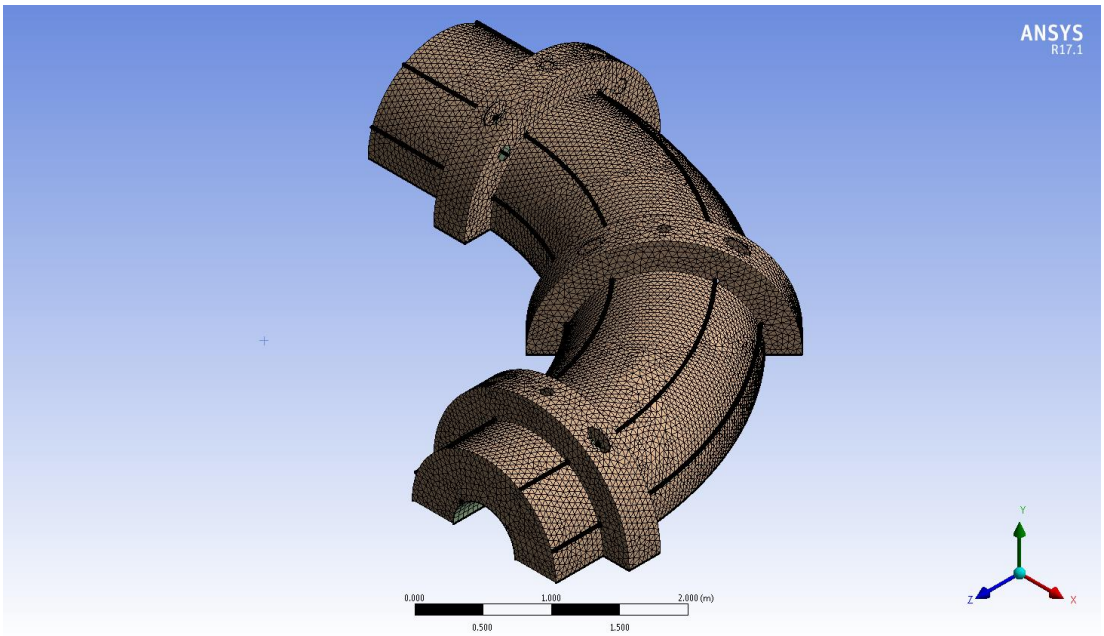

Figure 7.15 – The Mesh on the entire body for the Steady State Thermal Analysis.

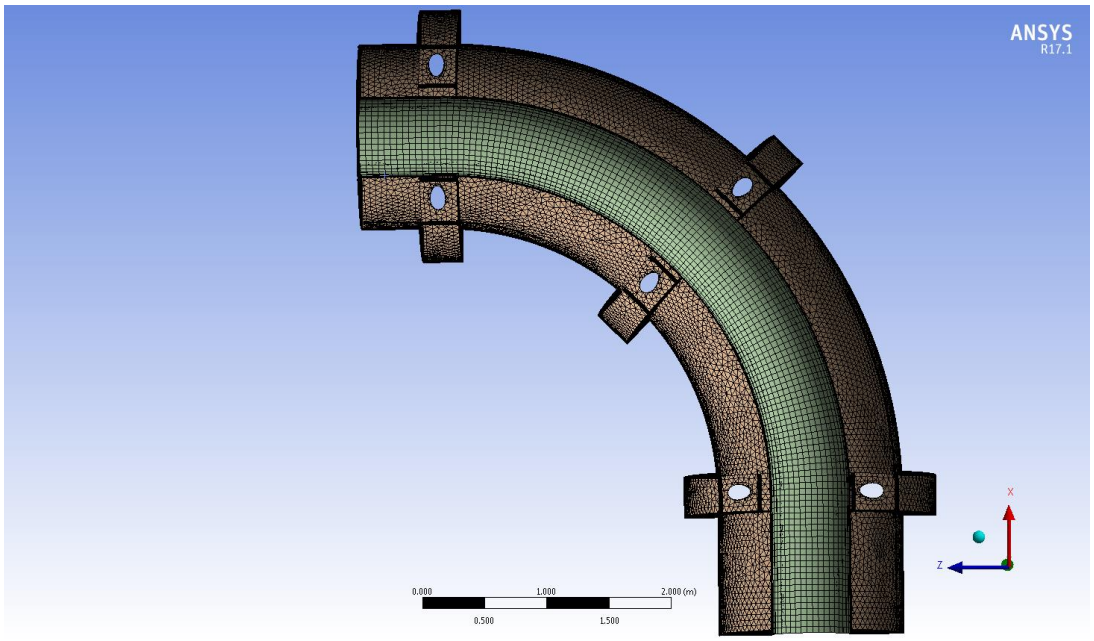

Figure 7.16 – The Mesh on the Inner Thermal Shield for the Steady State Thermal Analysis.

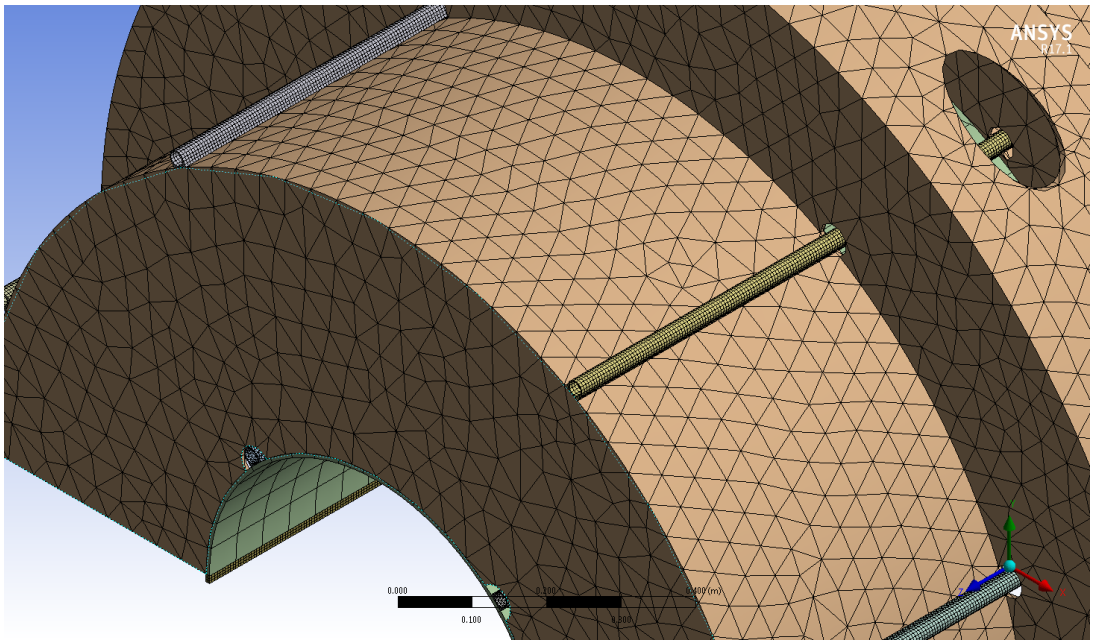

Figure 7.17 – The Mesh on the tubes and on the G10 layer for the Steady State Thermal Analysis.

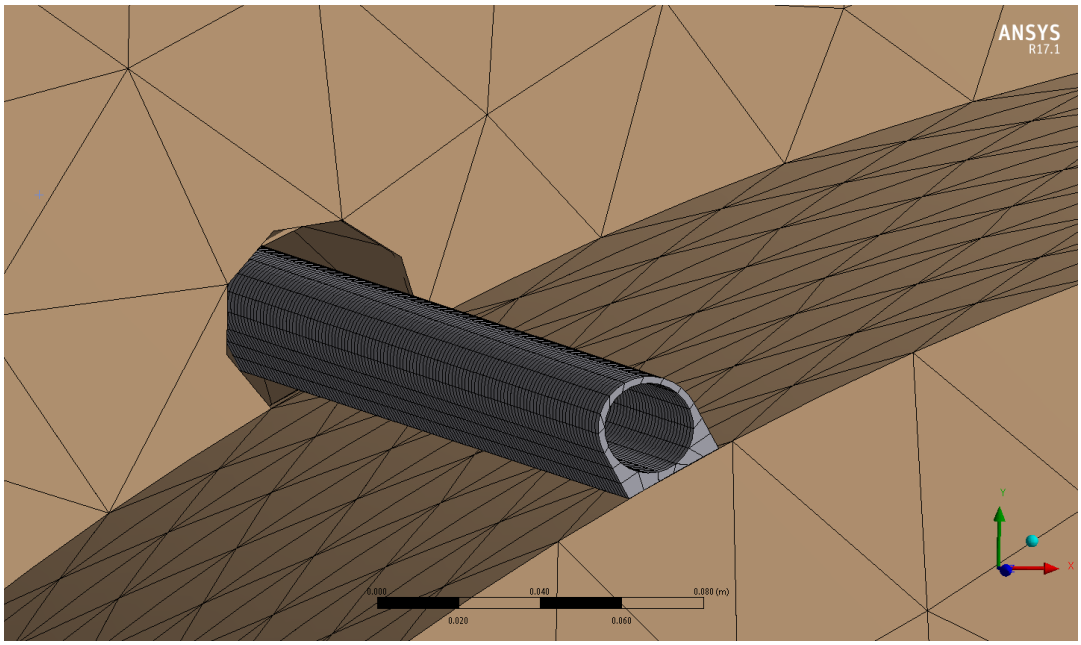

Figure 7.18 – Detail of the mesh on a tube.

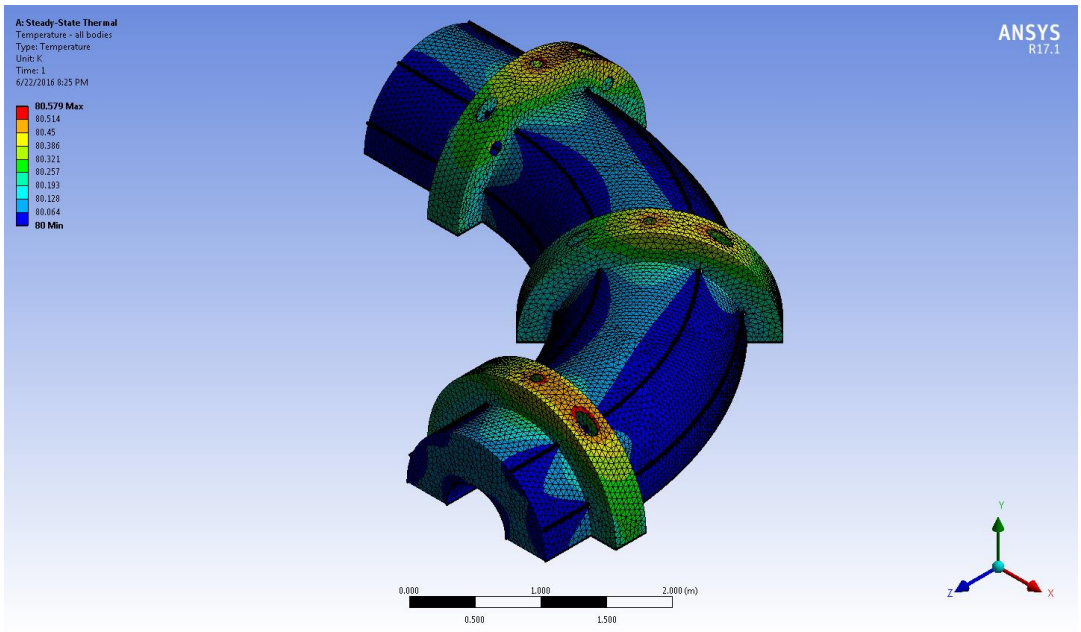

Figure 7.19 – Outer Thermal shield in the case with four tubes on it and two tubes on the Inner Thermal Shield.

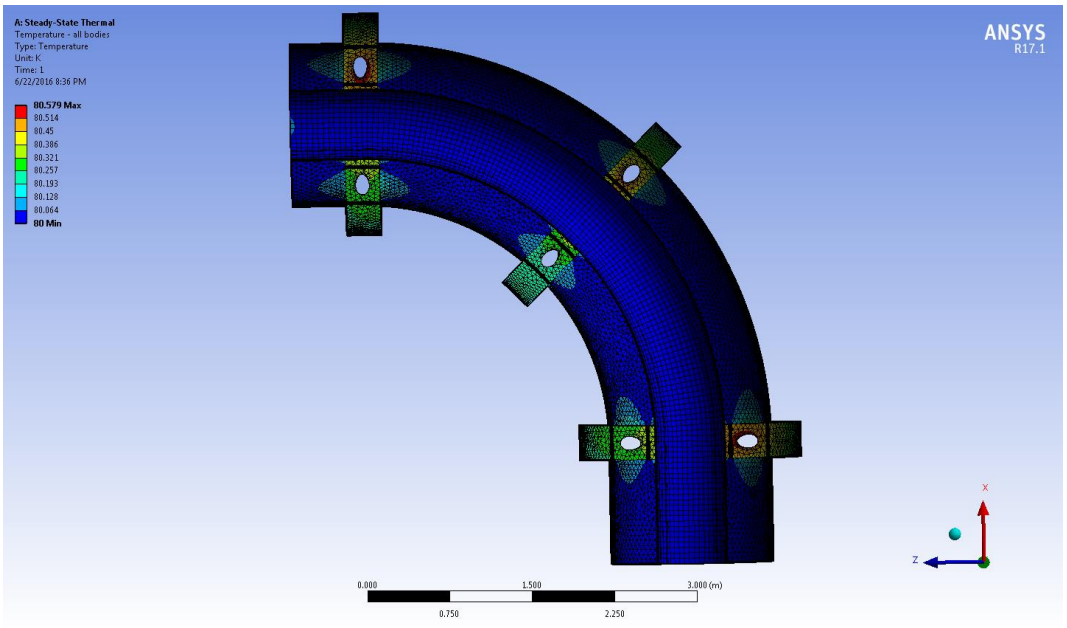

Figure 7.20 - Inner Thermal shield in the case with two tubes on it and four tubes on the Outer Thermal Shield.

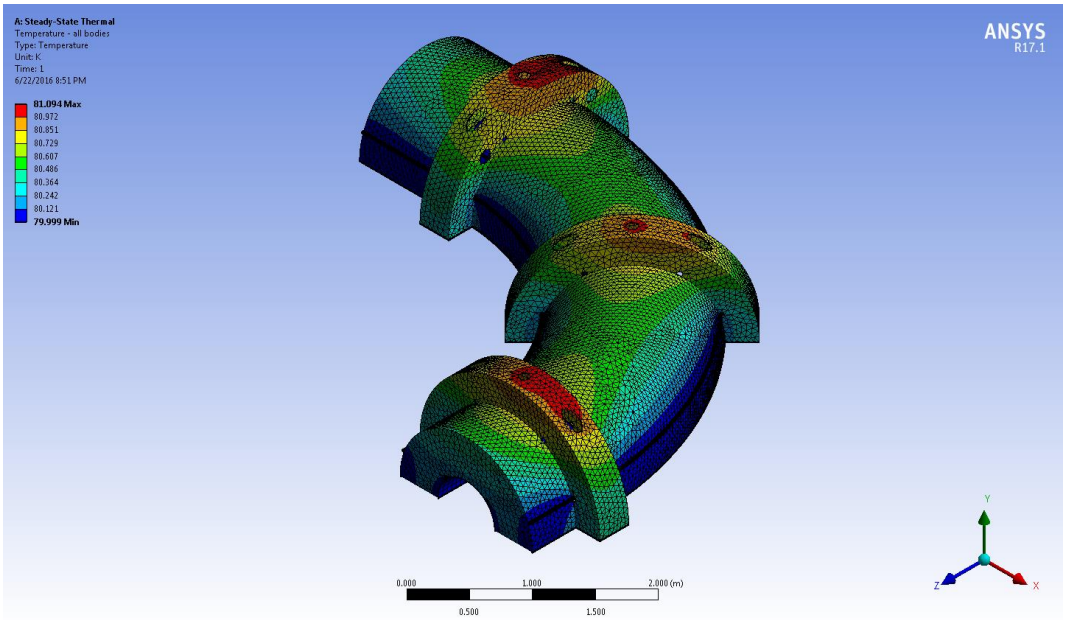

Figure 7.21 - Outer Thermal shield in the case with tubes at 20° only on it and two tubes on the Inner Thermal Shield.

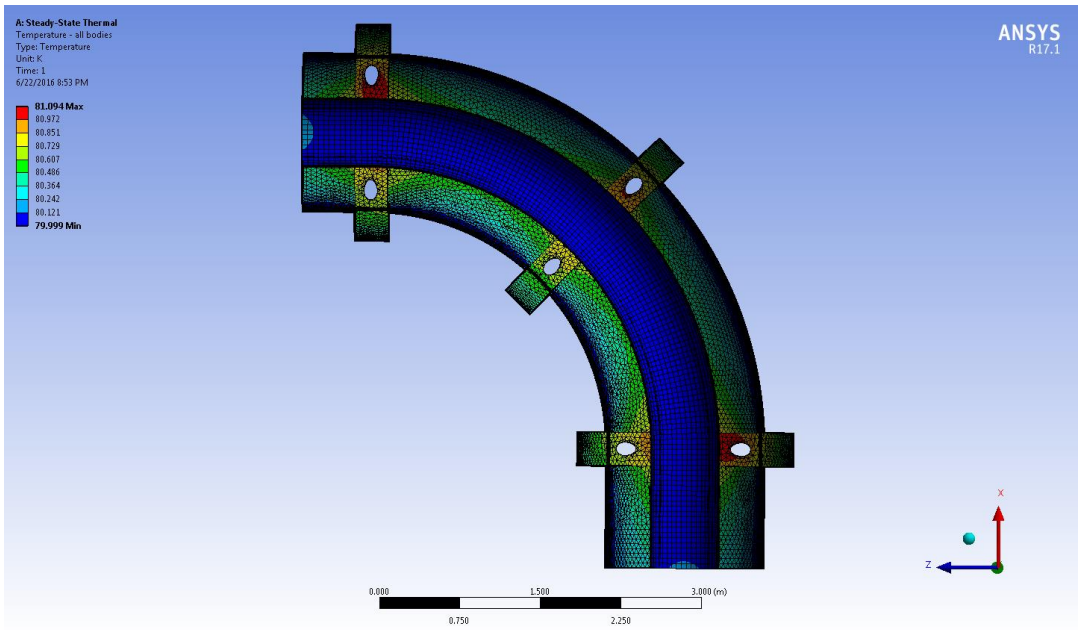

Figure 7.22 - Inner Thermal shield in the case with two tubes on it and two tubes at 20° on the Outer Thermal Shield.

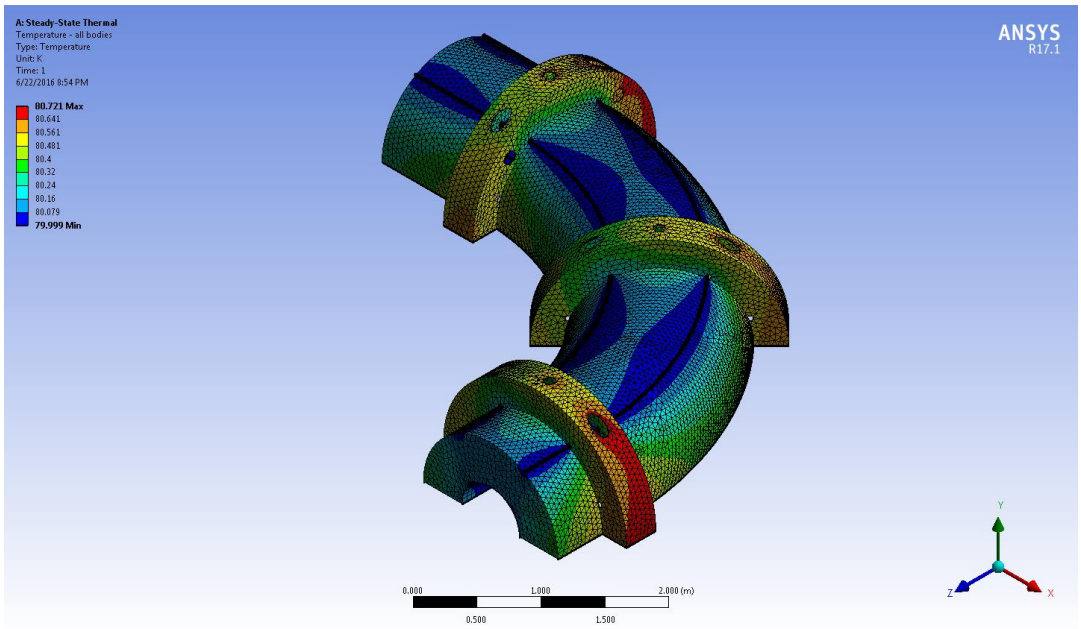

Figure 7.23 - Outer Thermal shield in the case with tubes at 60° only on it and two tubes on the Inner Thermal Shield.

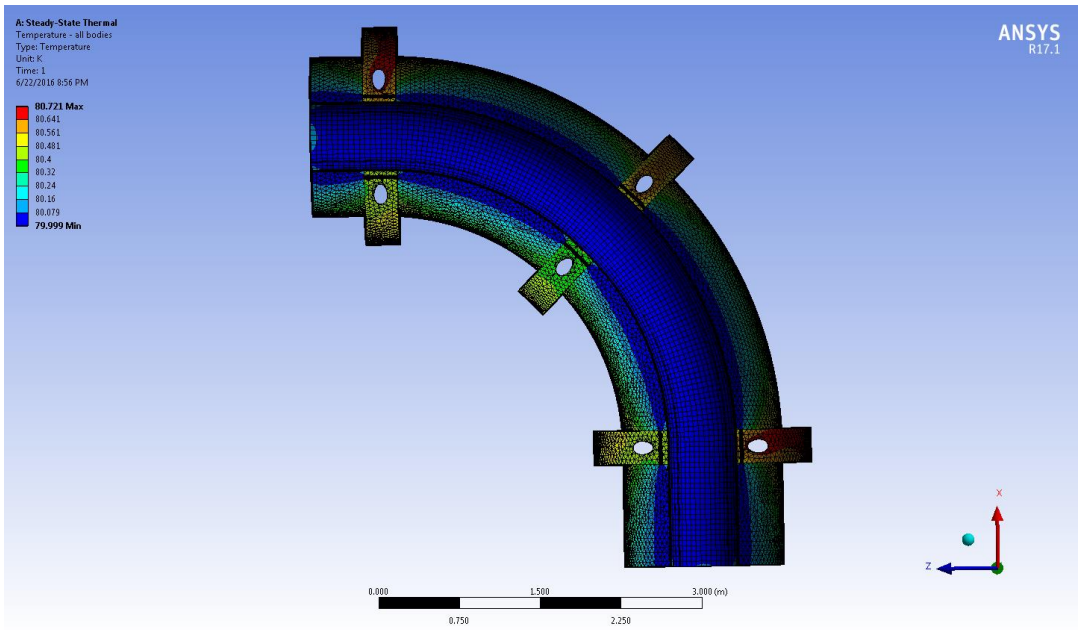

Figure 7.24 - Inner Thermal shield in the case with two tubes on it and two tubes at 60° on the Outer Thermal Shield.

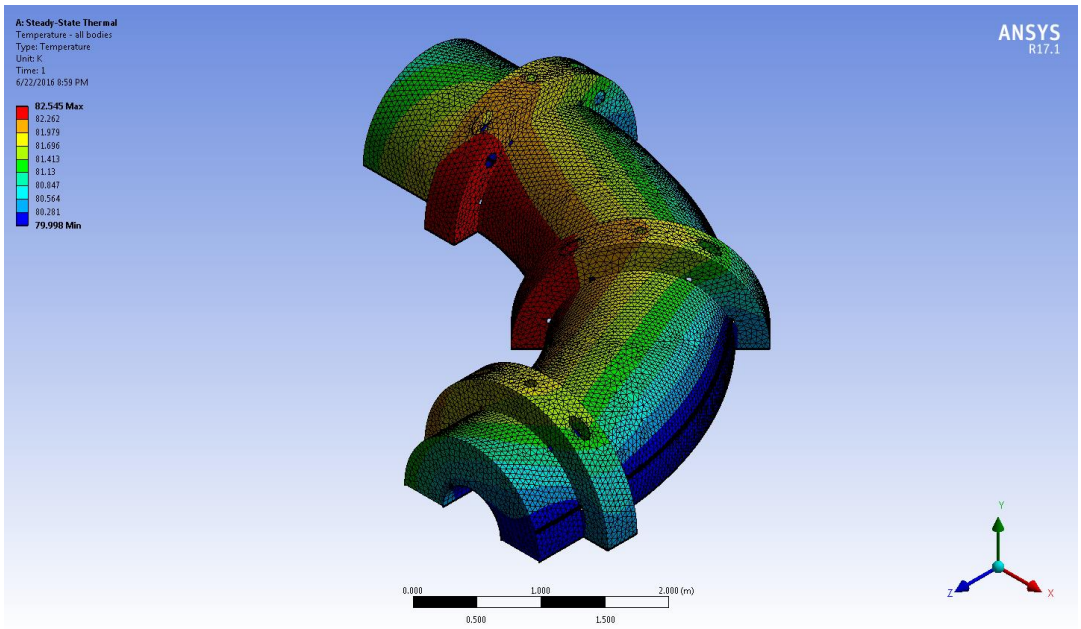

Figure 7.25 - Outer Thermal shield in the case with the "external" tube at 20° only on it and two tubes on the Inner Thermal Shield.

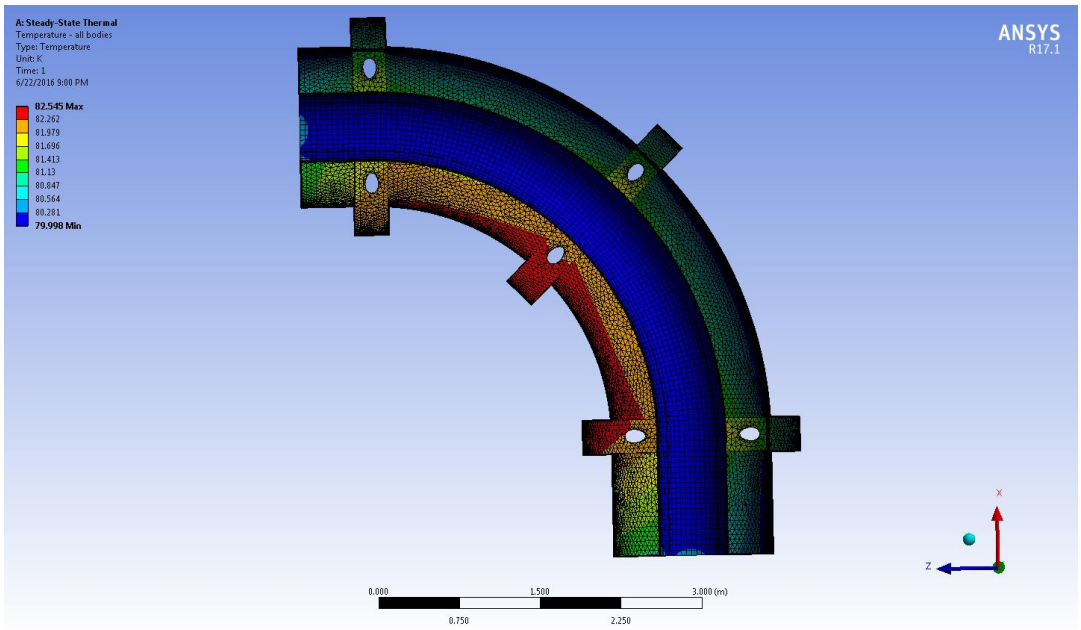

Figure 7.26 - Inner Thermal shield in the case with two tubes on it and the "external" tube at 20° only on the Outer Thermal Shield.

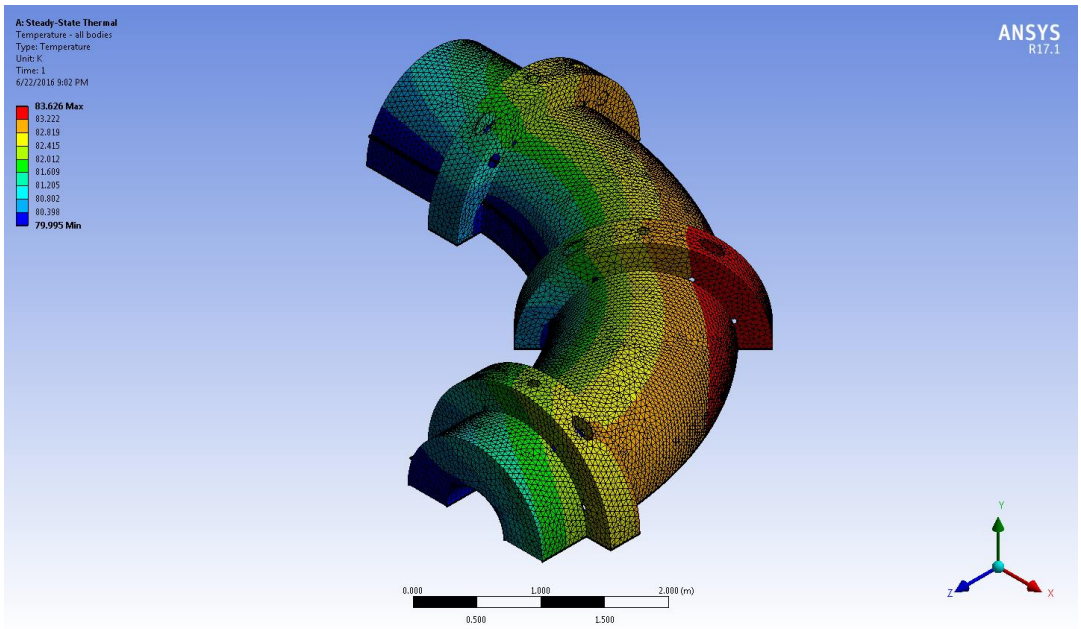

Figure 7.27 - Outer Thermal shield in the case with the "internal" tube at 20° only on it and two tubes on the Inner Thermal Shield.

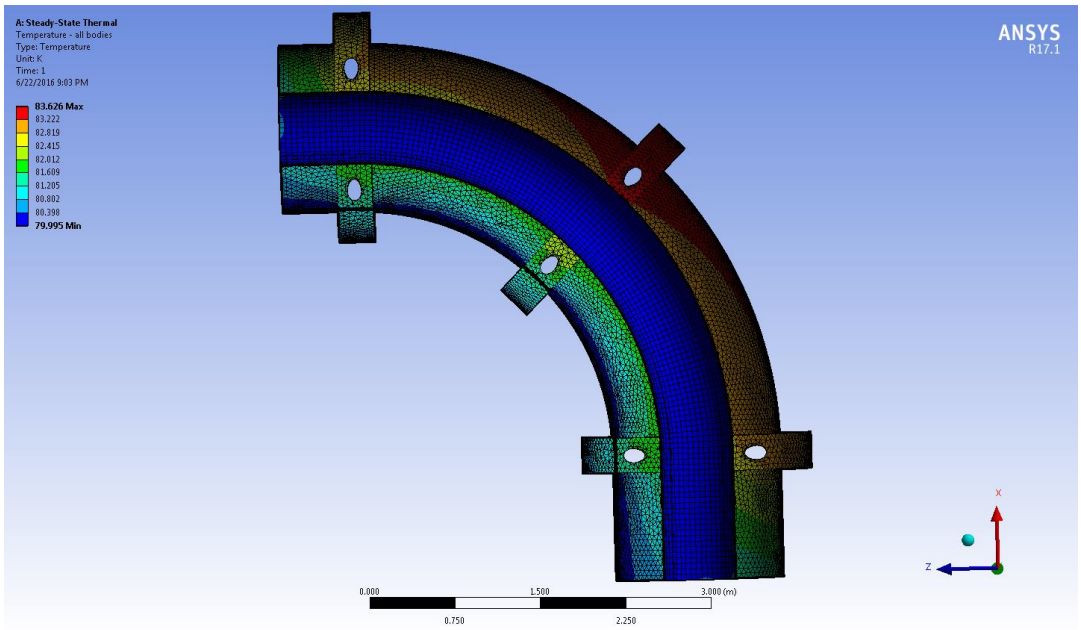

Figure 7.28 - Inner Thermal shield in the case with two tubes on it and the "internal" tube at 20° only on the Outer Thermal Shield.

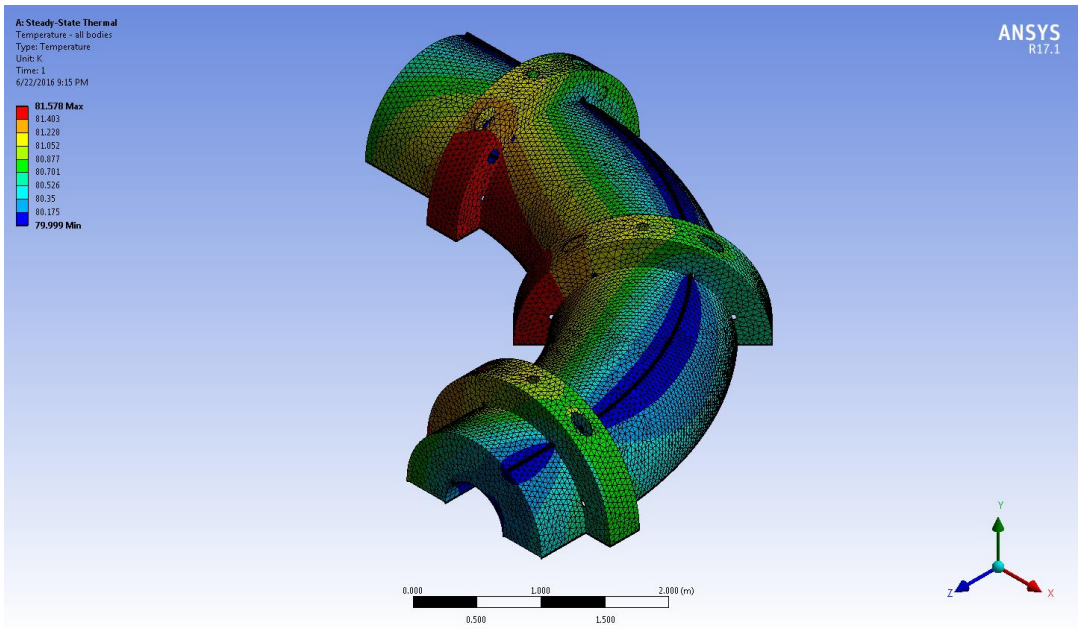

Figure 7.29 - Outer Thermal shield in the case with the "external" tube at 60° only on it and two tubes on the Inner Thermal Shield.

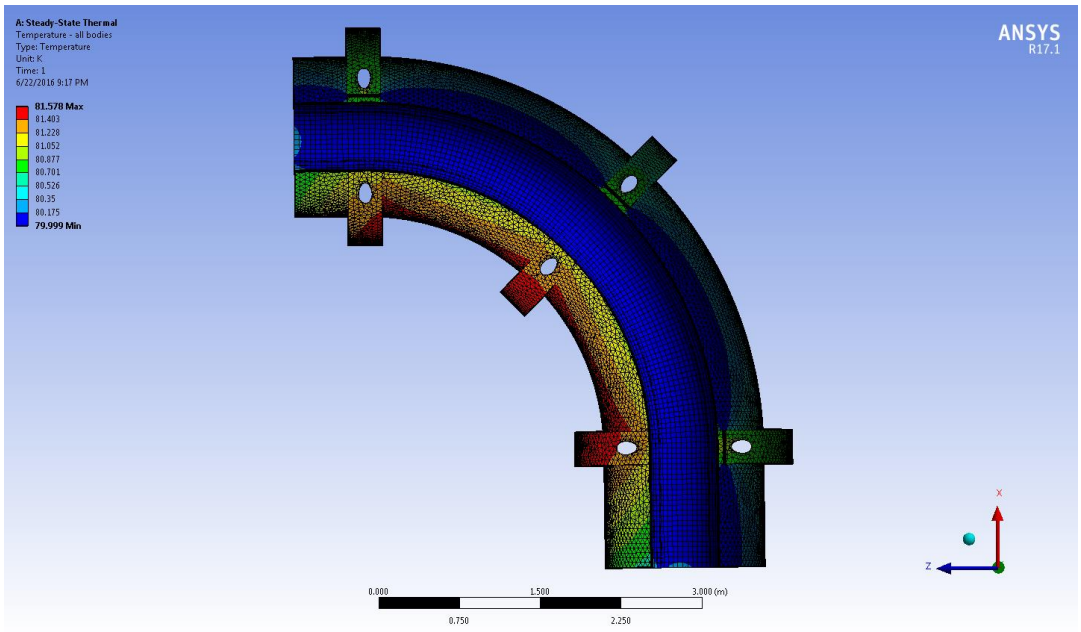

Figure 7.30 - Inner Thermal shield in the case with two tubes on it and the "external" tube at 60° only on the Outer Thermal Shield.

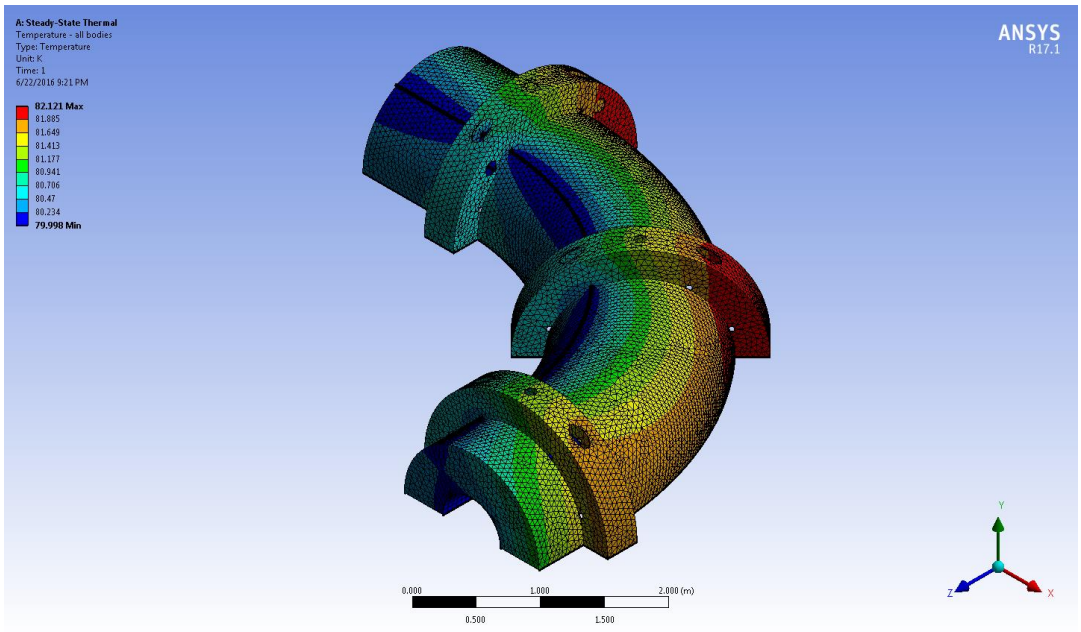

Figure 7.31 - Outer Thermal shield in the case with the "internal" tube at 60° only on it and two tubes on the Inner Thermal Shield.

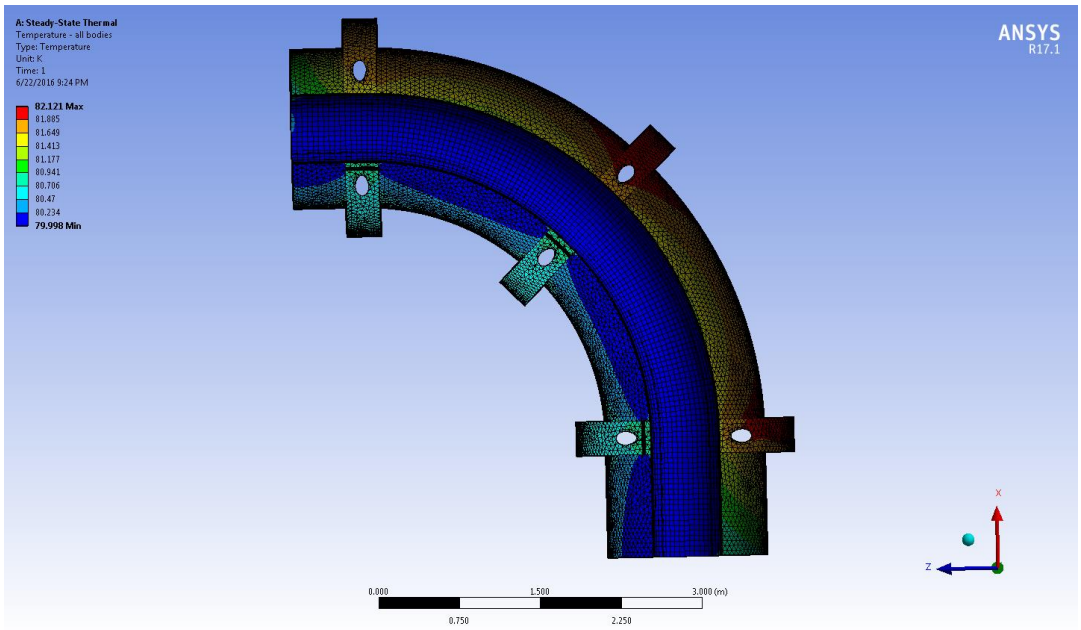

Figure 7.32 - Inner Thermal shield in the case with two tubes on it and the "internal" tube at 60° only on the Outer Thermal Shield.

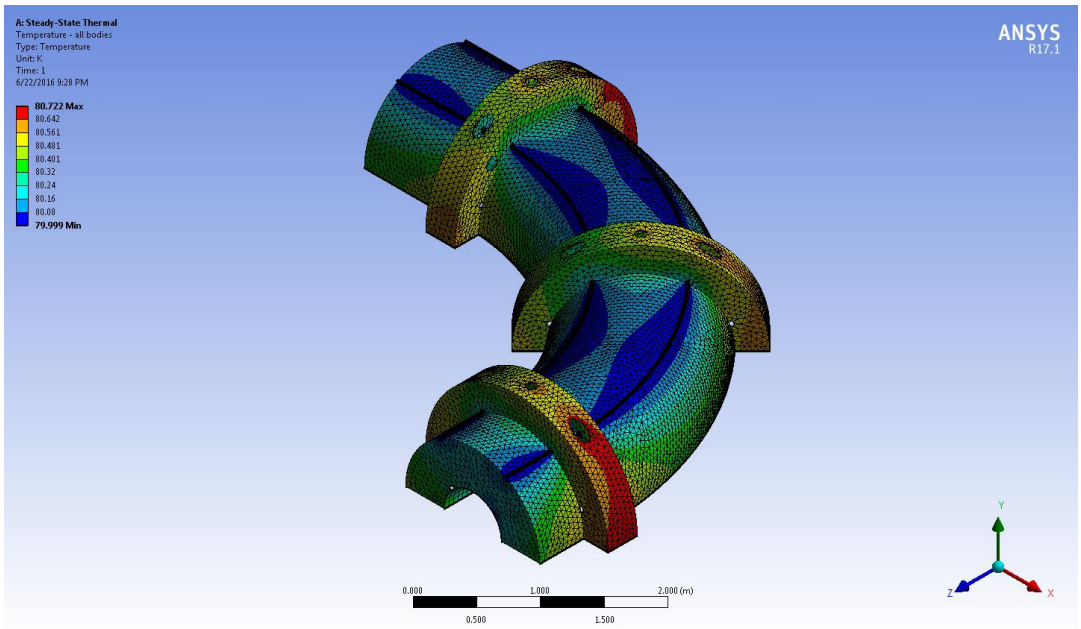

Figure 7.33 – Outer Thermal Shield in the case with two tubes at 60° only on it and the "external" tube only on the Inner Thermal Shield.

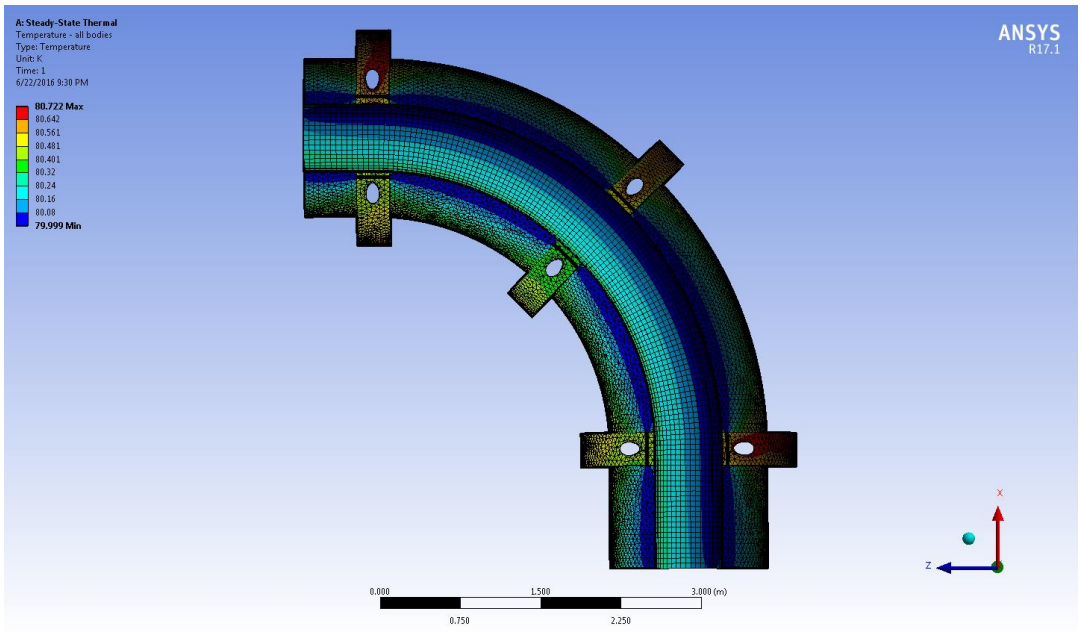

Figure 7.34 - Inner Thermal Shield in the case with the "external" tube only on it and two tubes at 60° only on the Outer Thermal Shield.

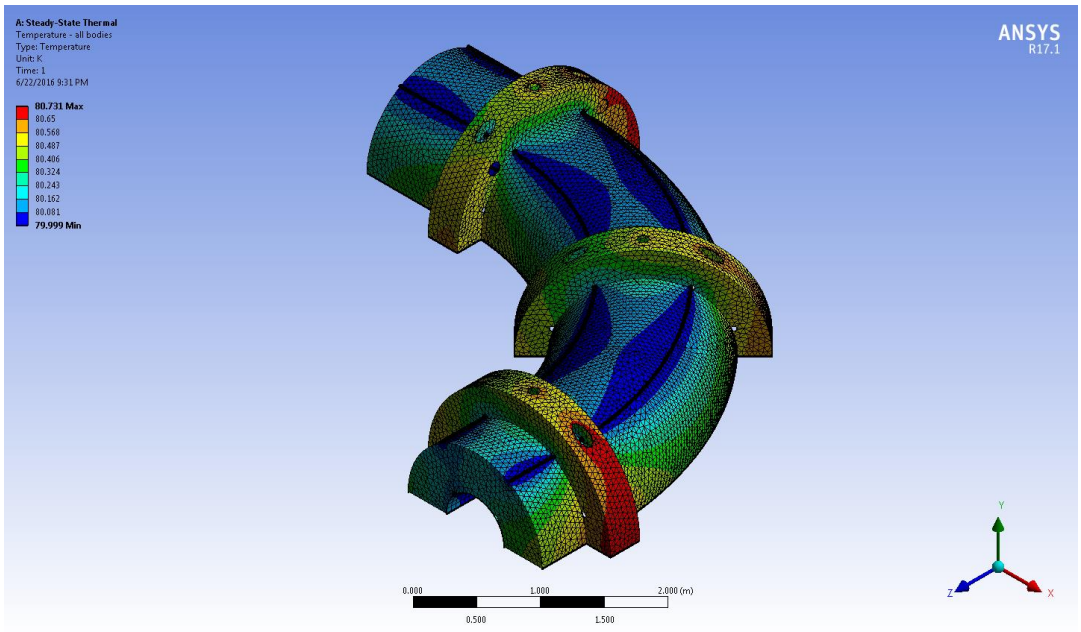

Figure 7.35 - Outer Thermal Shield in the case with two tubes at 60° only on it and the "internal" tube only on the Inner Thermal Shield.

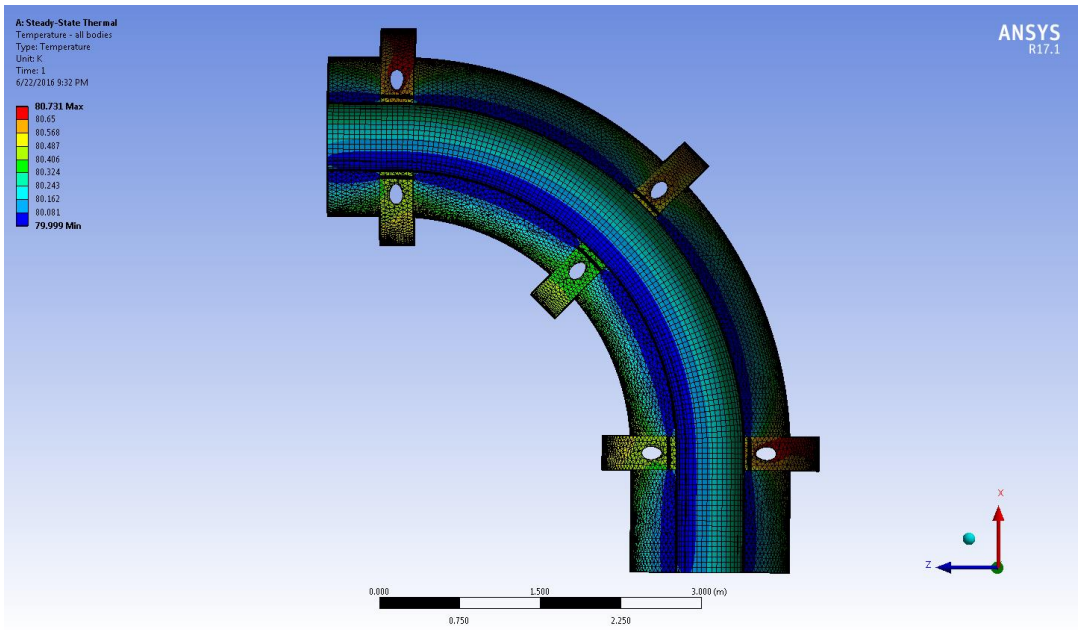

Figure 7.36 - Inner Thermal Shield in the case with the "internal" tube only on it and two tubes at 60° only on the Outer Thermal Shield.

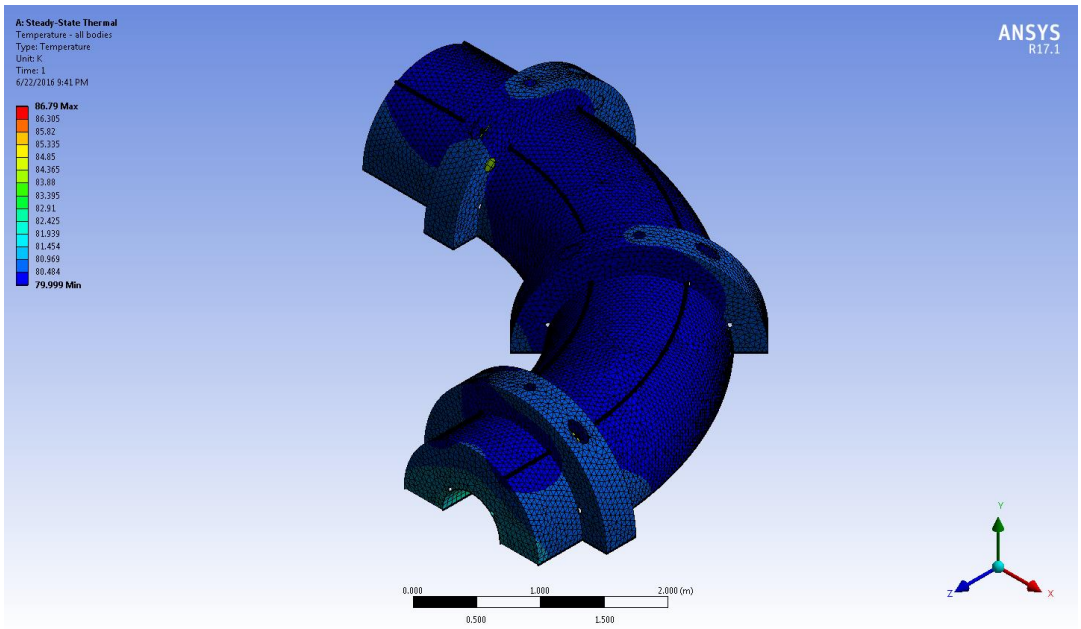

Figure 7.37 - Outer Thermal Shield in the case with two tubes at 60° only on it and no tubes on the Inner Thermal Shield.

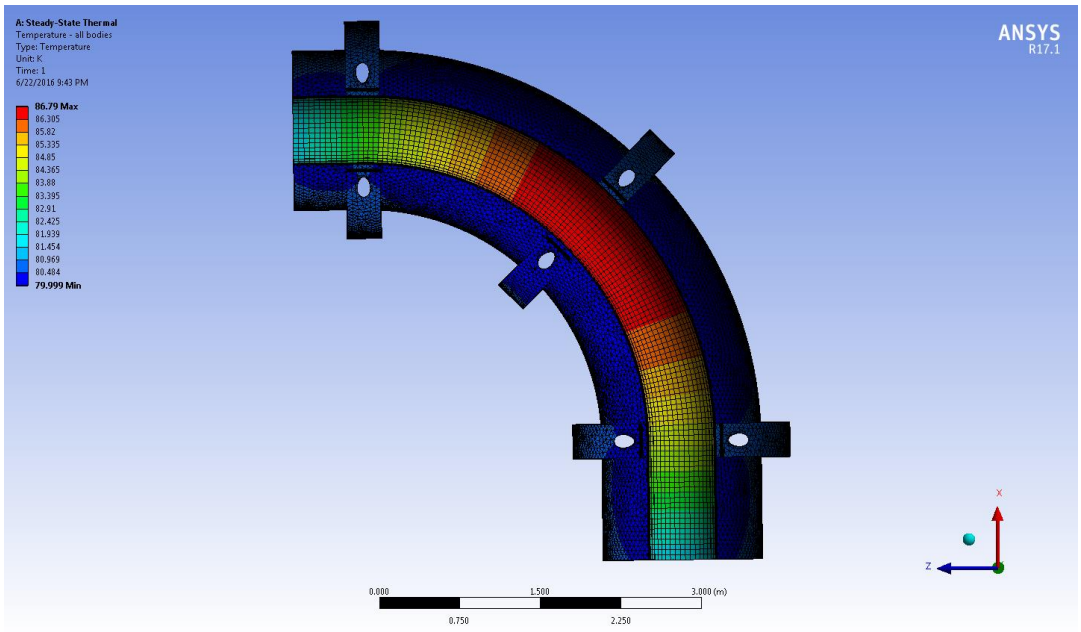

Figure 7.38 - Inner Thermal Shield in the case with no tubes on it and two tubes at 60° only on the Outer Thermal Shield.

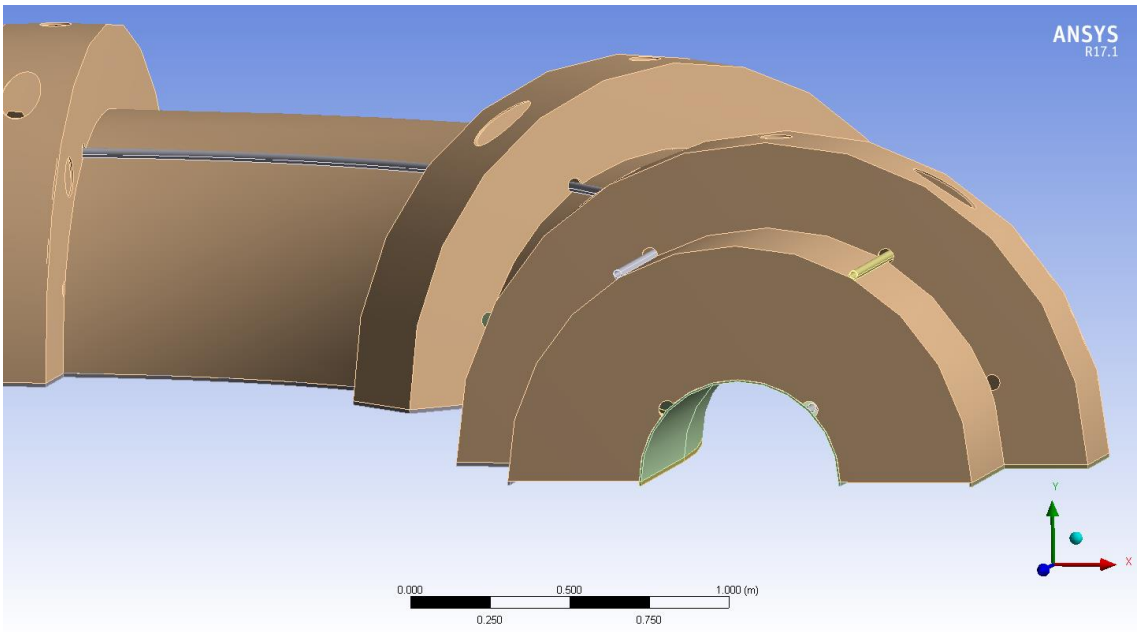

Figure 7.39 – Chosen cooling scheme from the Steady State Thermal Analysis.

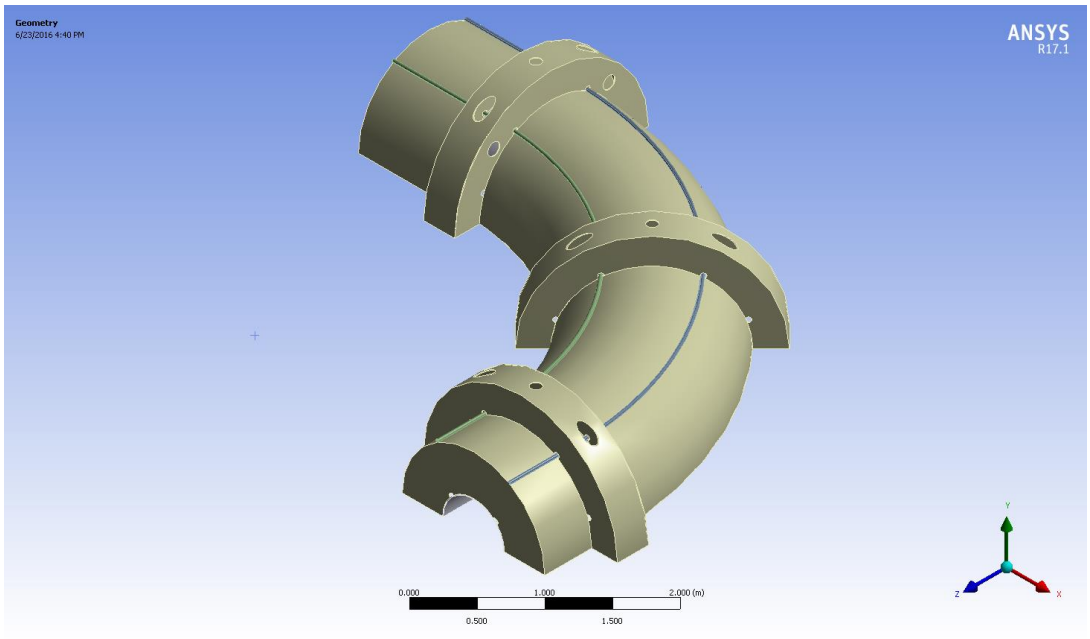

Figure 7.40 – Simplified model of the Thermal Shield for the Transient Thermal Analysis.

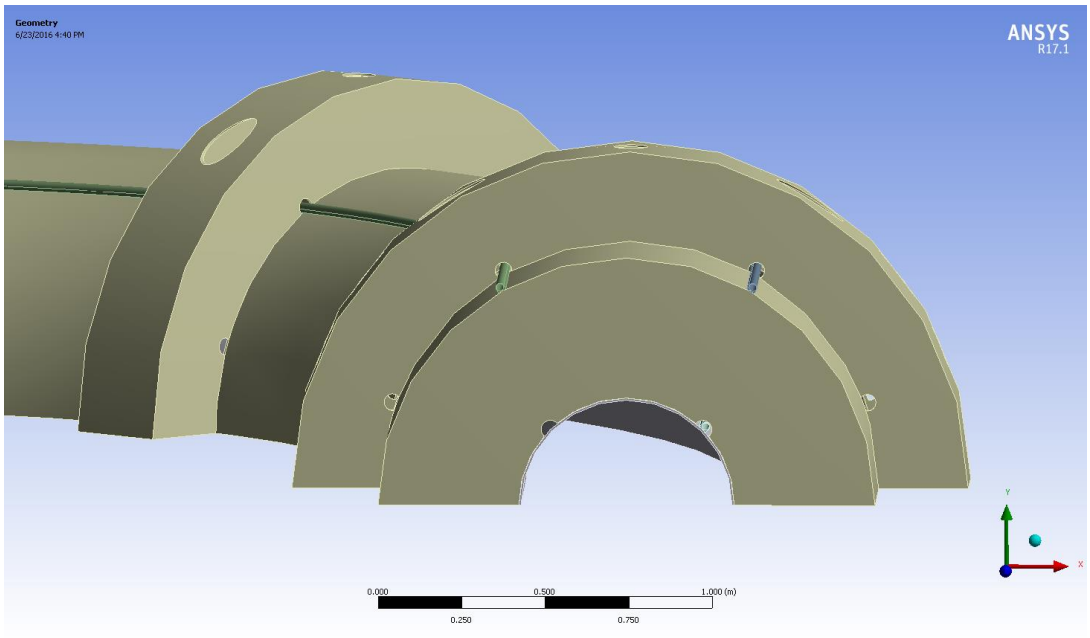

Figure 7.41 – Arrangement of the tubes in the model of the Thermal Shield for the Transient Thermal Analysis.

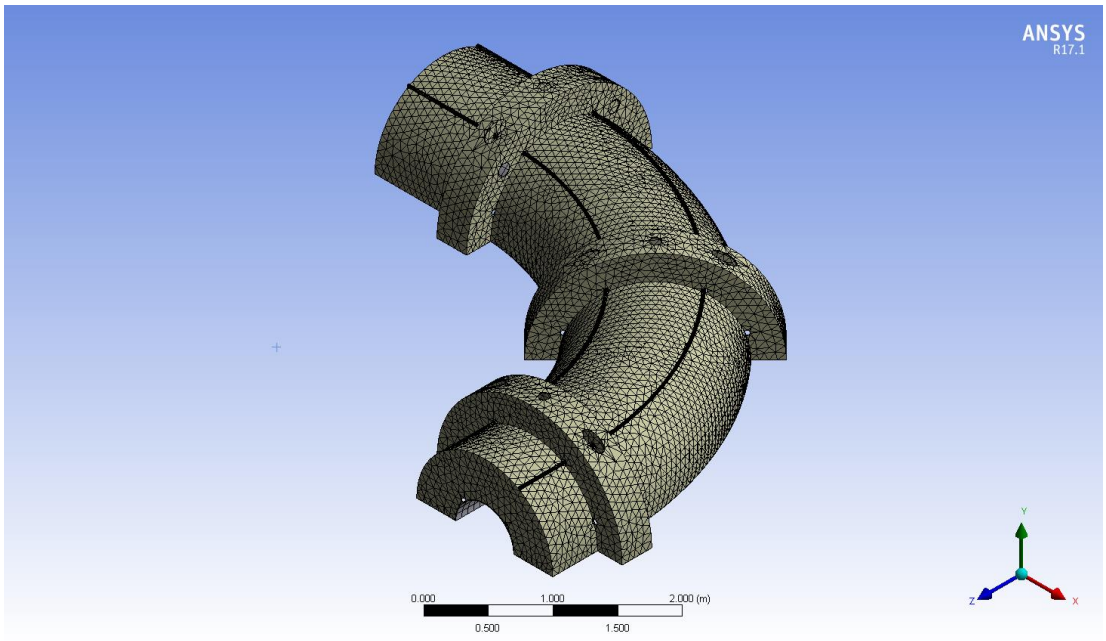

Figure 7.42 – The Mesh on the entire body for the Transient Thermal Analysis.

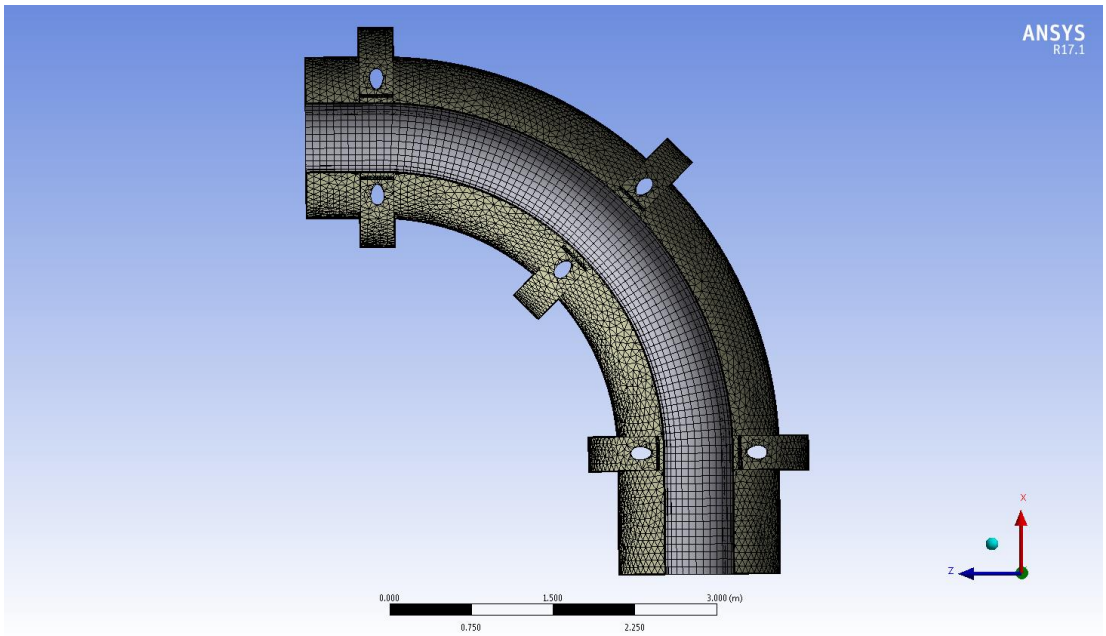

Figure 7.43 – The Mesh on the Inner Thermal Shield for the Transient Thermal Analysis.

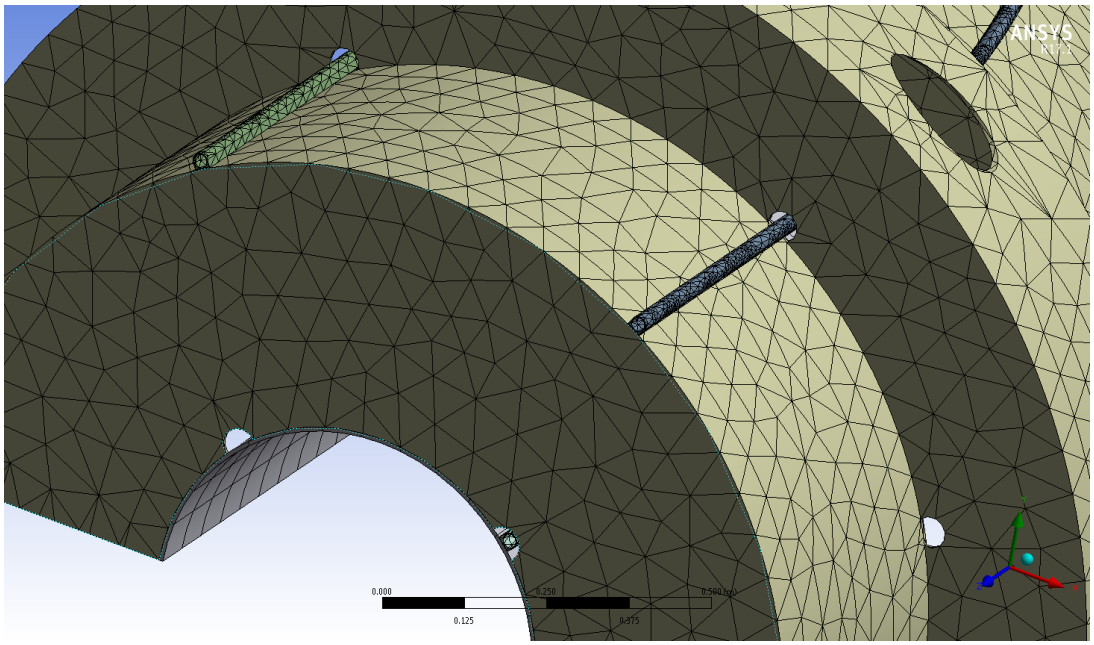

Figure 7.44 – The Mesh on the tubes for the Transient Thermal Analysis.

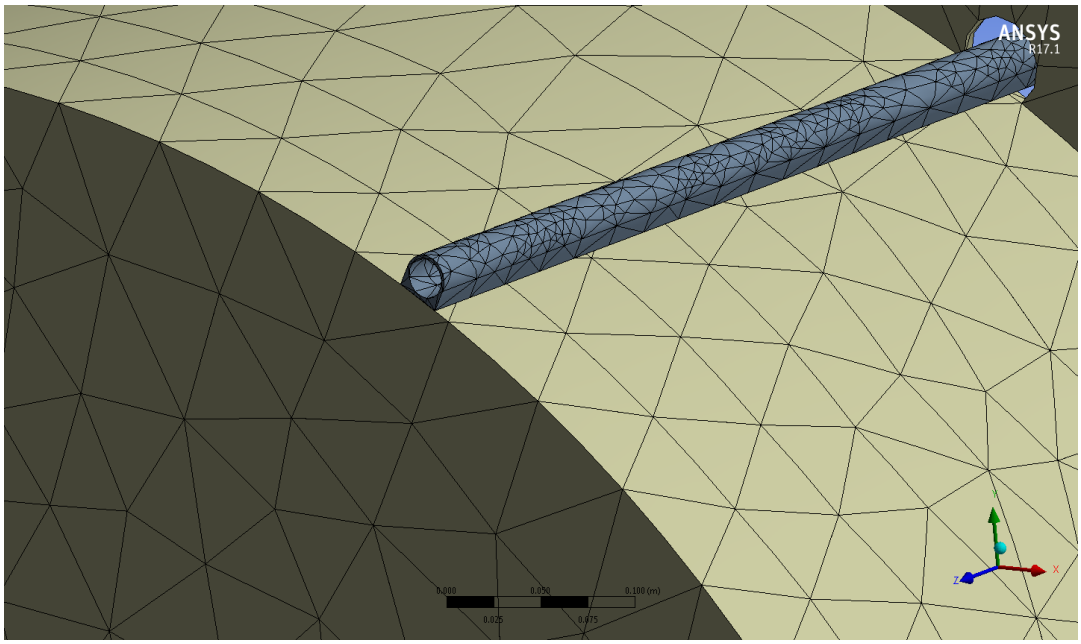

Figure 7.45 – Detail of the mesh on a tube.

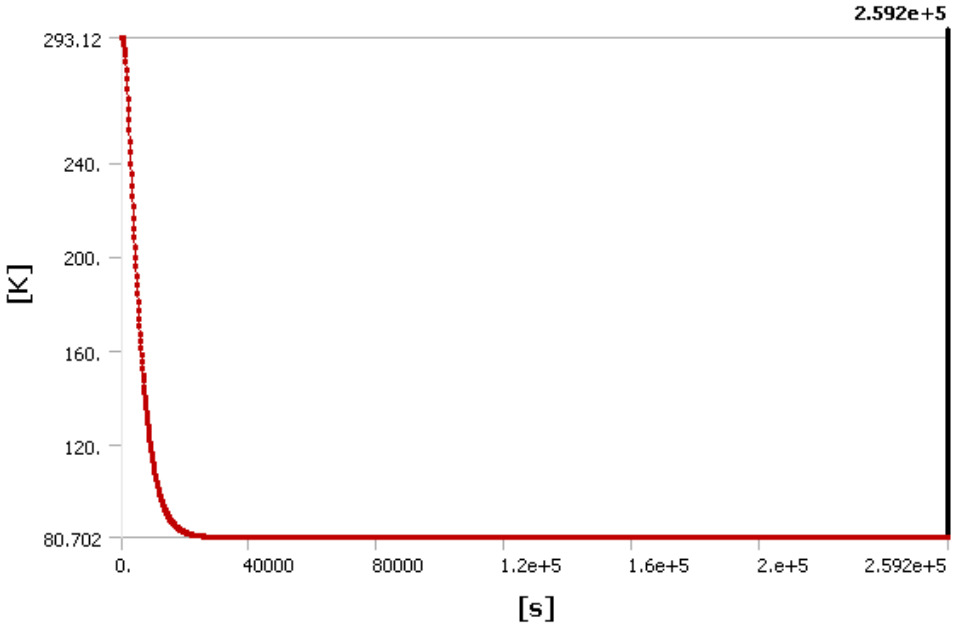

Figure 7.46 – Maximum temperature profile.

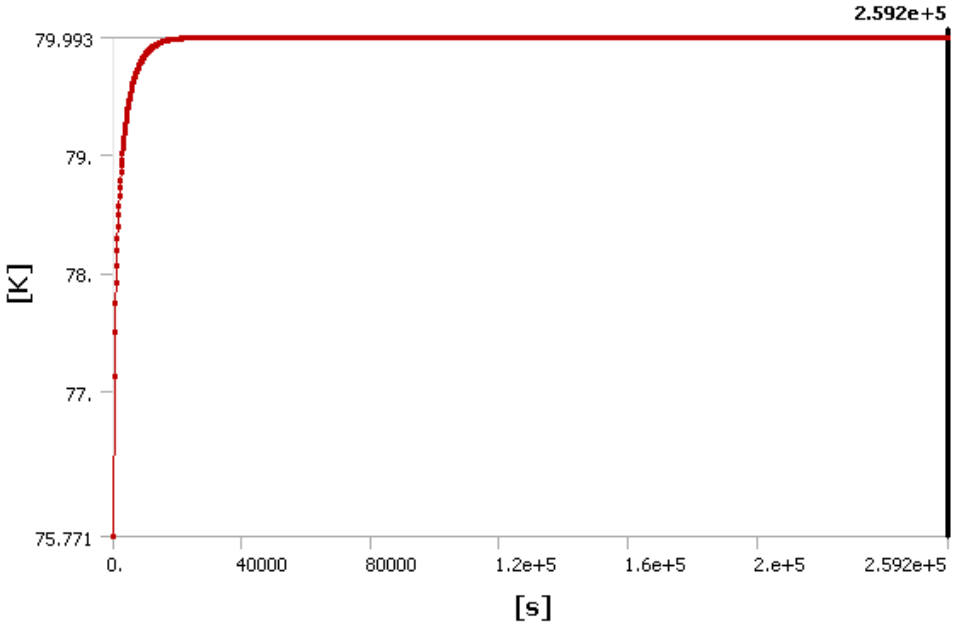

Figure 7.47 – Minimum temperature profile.

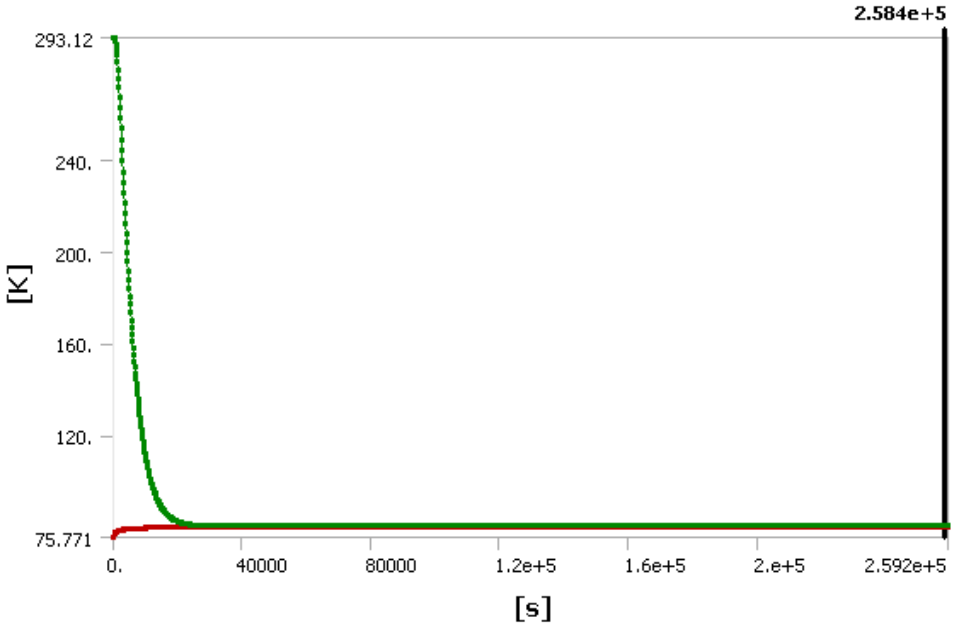

Figure 7.48 – Profile of the global maximum and minimum temperature during the cooling down.

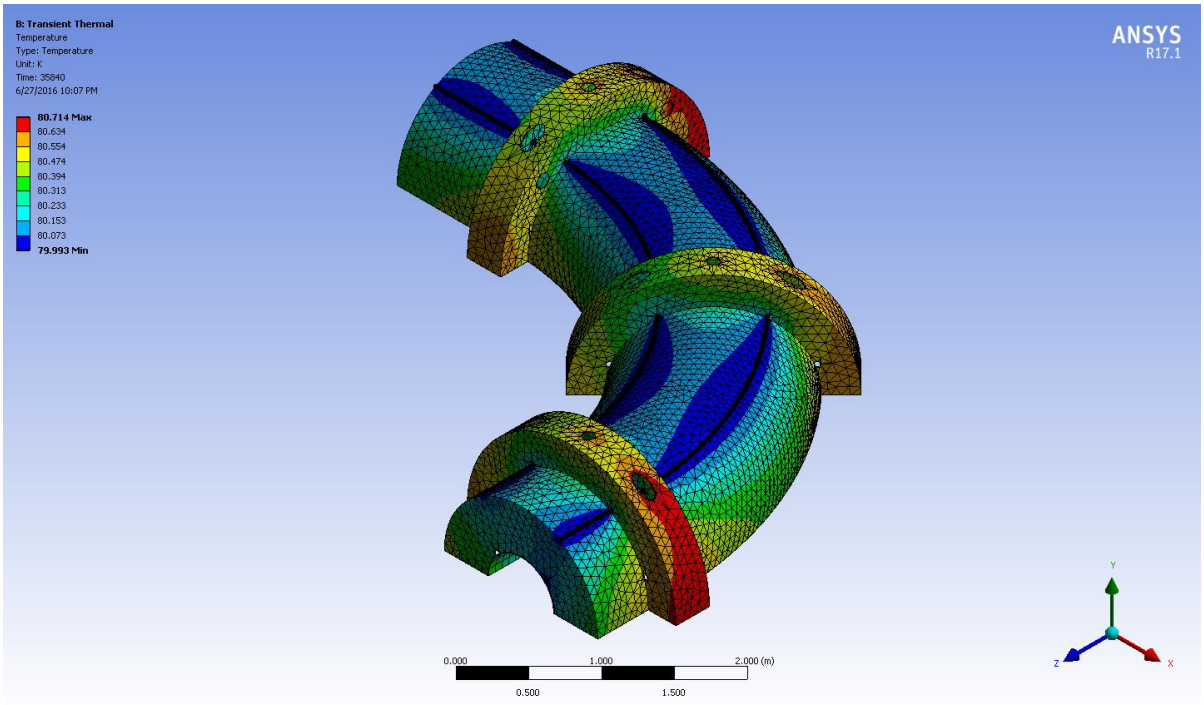

Figure 7.49 – Temperature distribution on the Outer Thermal Shield after cooling down.

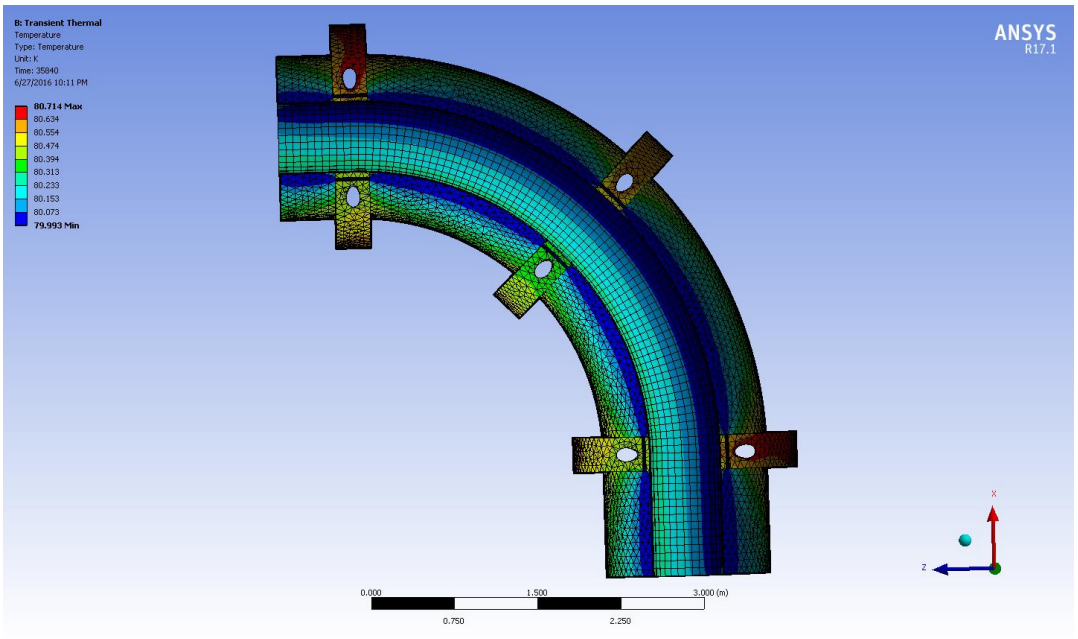

Figure 7.50 – Temperature distribution on the Inner Thermal Shield after cooling down.

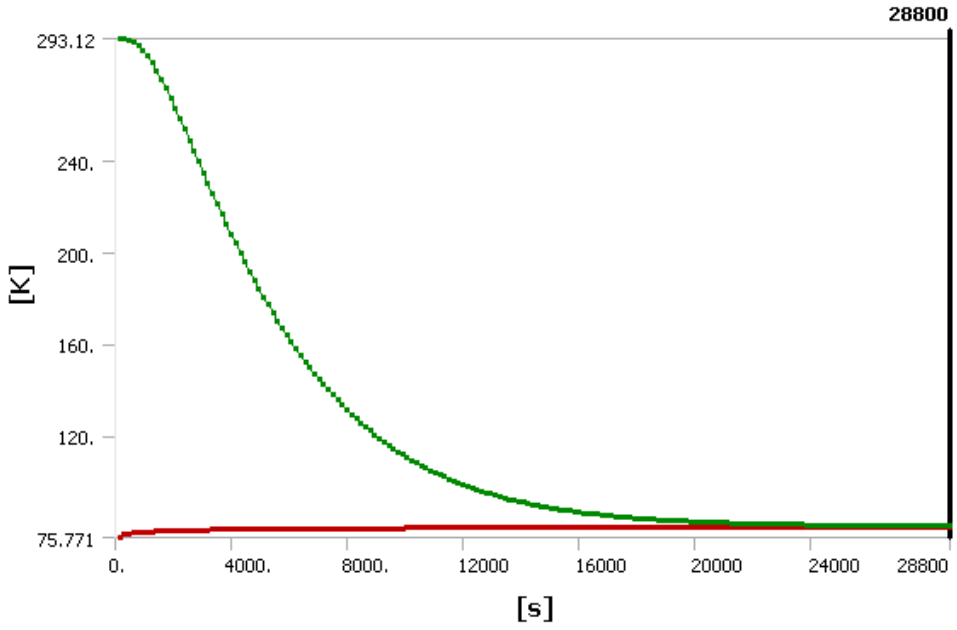

Figure 7.51 – Profile of the global maximum and minimum temperatures during the first eight hours of cooling down.

8. TSU WARM BORE HEATING SYSTEM

As described at the beginning of Section 7, the Warm Bore has an inner diameter equal to ID = 500 mm and a thickness t = 15.875 mm. [1]

As the Vacuum Vessel, it is made by 316L stainless steel, is maintained at room temperature (T = 293.15 K) and has a pressure $p = 1.3 \times 10^{-4}$ Pa. The physical properties of the 316L stainless steel are summarized in Table 7.1.

As we can see from Figures 4.11 – 4.12, which give an overview of the TSu cryostat, it is located inside the Inner Thermal Shield, that has a temperature T = 80 K and a pressure $p = 1.3 \times 10^{-4}$ Pa.

Since the Warm Bore and the Thermal Shield have different temperatures, there is a heat flux that comes from the Warm Bore and enters the inner surface of the Inner Thermal Shield. It is due to radiation and residual gas conduction. Thermal radiation protection of the Thermal Shield is enhanced by the use of MLI (described in Section 7), so the value of the heat flux is equal to 1.5 W/m^2.

The first steady state thermal analysis had the aim to determine the Warm Bore temperature, considering the heat flux.

Although, the second analysis took into account the scenario with the Warm Bore temperature lower than the temperature at which the water freezes. This is not a problem until the cryostat is sealed. However, the Warm Bore has to be opened for maintenance and, in this case, the air is expected to enter it and the water contained in the air to freeze on its walls.

In order to avoid the icing, it was decided to put some heaters on the top of the Warm Bore external surface. The second steady state thermal analysis on the Warm Bore aims to establish how many heaters we needed, in what position and at what power, to maintain the Warm Bore at room temperature. In this way, we should not have problems during the opening of the cryostat, or even in the case of a vacuum loss.

8.1 WARM BORE MODEL

The steady state thermal analysis on the Warm Bore without a heating system and the one with the heaters were both conducted in Ansys Workbench 17.1.

The model that was used represented the Warm bore inside the Vacuum Vessel, neglecting the Thermal Shield and the Coil Module Assembly (Figures 8.1 – 8.2). The Vacuum Vessel has an inner diameter

ID = 1605.95 mm and a thickness equal to t = 19.05 mm, while the Warm Bore has an inner diameter ID = 500 mm and a thickness equal to t = 15.875 mm. [1]

The Vacuum Vessel is represented with its suspension system: it is formed by three supports that connect it to the floor. In addition, also the radial, axial and gravity supports, that connect it to the Thermal Shield, are considered.

Both the Vacuum Vessel and the Warm Bore are made by 316L, an austenitic stainless steel.

In fact, austenitic stainless steels are the "workhorse" materials for cryogenics over all temperature ranges. They are readily available in a variety of forms, have good impact strengths, are easily welded vacuum tight, and have a moderately high tensile modulus (≈ 200 GPa), an ASME Code [2] design strength of 129.6 MPa at room temperature, and thermal conductivity [3] ranging from 14.7 W/m-K at 300 K to 7.9 W/m-K at 77 K to 0.28 W/m-K at 4 K. The 300-series stainless steel as types 304, 304L, 304N, 316, 316L and 321 are reasonably clean with respect to surface outgassing, are readily baked out, and have less diffused hydrogen than typical carbon steel. One caveat is that stainless steel bars sometime have axial inclusions that leak slowly or not at all at ambient temperature but may exhibit profuse vacuum leak rates at cryogenic temperatures. Also, very high tensile and yield strengths are obtained from cold-worked 300-series stainless steel machined parts and cables, but these improved properties are lost by the annealing effect of welding or brazing.

8.2 HEAT LOADS ON THE WARM BORE

A temperature equal to T = 295.15 K, representing the room temperature, was imposed on the Vacuum Vessel and the Warm Bore. Moreover, to maintain the Vacuum Vessel at this temperature during the analysis, a temperature T = 295.15 K was imposed also on the base of the three supports that formed the suspension system (Figure 8.3).

On the Warm Bore was imposed a heat flux equal to -1.5 W/m^2 (Figure 8.4). Its value was negative to specify that it came out from the outer surface of the Warm Bore and it represented the thermal exchange between it and the Thermal Shield (Figures 4.11 – 4.12), even if the shield was not included in the model.

Since the purpose of the steady state analysis of the Warm Bore without a heating system was to analyze how the temperature of the Warm Bore was influenced by the Thermal Shield one, the imposed temperature and heat load just described were enough for it. Whereas, in the steady state analysis of the Warm Bore with a heating system the aim was to maintain the Warm Bore at room temperature, in order to avoid the icing problem. We imposed again the data just described, but, as we will see in Section 8.5,

we added a positive heat flow, entering the outer surface of the Warm Bore, for each of the heaters. We ran several simulations with different arrangement of the heaters.

8.3 Selection of the Mesh for the Finite Element Analysis

To obtain the mesh size sensitivity (Table 8.1) we tested six different mesh densities.
The temperature average was chosen as benchmark. In the model there were no sections with significant smaller dimensions than the others, so it was chosen to use just one body sizing for the entire body.
It was chosen to use the Mesh with 3325641 elements, in order to reduce the computation time. It is a hybrid grid, with both structured and unstructured parts. It is shown in Figures 8.5 – 8.6.

8.4 Steady State Thermal Analysis of the Warm Bore without a heating system

8.4.1 Results

For the steady state thermal analysis of the Warm Bore without a heating system, using the chosen mesh with 3325641 elements, the elapsed time needed to complete the simulation was equal to 16 min 48 s.
The thermal power generated from the Warm Bore, was equal to 16.255 W.
As shown in Figure 8.7, the temperature on the Vacuum Vessel remained equal to T = 295.15 K, except for its two extremities, which had a temperature of T = 288.53 K.
Although, as we can see from Figure 8.8, the temperature on the two extremities of the Warm Bore was T = 281.91 K and it decreased to T = 235.57 K towards the Warm Bore center.

8.4.2 Discussion of the results

The value of the thermal power generated from the Warm bore can be checked by the Equation 8.1:

$$\dot{Q} = A \times q = 10.837 \times (-1.5) = -16.255 \text{ W} \qquad \textit{(Eq. 8.1)}$$

where $A = 10.837 \text{ m}^2$ is the Warm Bore surface area, acquired from Ansys Workbench 17.1, while $q = -1.5 \text{ W/m}^2$ is the imposed heat flux. In the calculation, the negative sign of the thermal power indicates that the it comes out from the Warm Bore surface.

The temperature on the Warm bore varies from a minimum temperature of T = 235.57 K on the center of the body, to a maximum one of about T = 280 K on its extremities, and almost all the shell is below the temperature at which the water freezes.

This is not a problem during the experiment. In fact, in this case, the cryostat is sealed and the vacuum is maintained inside it, so there is no air flow and, consequently, no icing problem.

However, in case of a vacuum loss or, more simply, when it is necessary to open the cryostat for maintenance, icing becomes a real problem, because the air humidity inevitably freezes on the wall of the Warm Bore.

To avoid this problem, it was chosen to use some heaters in order to maintain the Warm Bore at the room temperature. The number, position and power of the heaters are the subject of the analysis presented in Section 8.5.

8.5 STEADY STATE THERMAL ANALYSIS OF THE WARM BORE WITH THE HEATING SYSTEM

8.5.1 Results

For the steady state thermal analysis of the Warm Bore with a heating system, using the chosen mesh with 3325641 elements, several simulations were realized to identify the most appropriate arrangement for the heaters, changing the number, the position and the power of the heaters themselves.

As we can see in Figure 8.2, the model of the Warm Bore is divided into ten sections. Established that the heaters should have been placed on the top of the Warm Bore external wall, it was decided to represent each of them as a positive heat flow, entering the outer surface of the shell.

The heaters thermal flows, so, have the opposite direction to the 1.5 W/m^2 heat flux. As a result of this, the thermal power generated from the Warm Bore in the case without heaters, equal to 16.255 W, is expected to decrease.

The results for each simulation, in terms of minimum and maximum temperature and thermal power generated from the Warm Bore, are summarized below:

1. Two central heaters at 2 W each and two heaters at the extremities at 1 W each

   The positions of the heaters are shown in Figure 8.9.

   As shown in Figure 8.10, the temperature on the Warm bore varies from a minimum temperature T = 262.73 K on the center of the body, to a maximum one equal to T = 287.95 K on its extremities. Although, the Vacuum Vessel is maintained at T = 295.15 K, except for its extremities, which have a temperature T = 291.55 K.

The thermal power generated from the Warm Bore is equal to $\dot{Q}$ = 10.255 W.

2. Two central heaters at 2 W each and two heaters at the extremities at 2 W each

   The positions of the heaters are shown in Figure 8.9.

   As shown in Figure 8.11, the temperature on the Warm bore varies from a minimum temperature T = 266.65 K on the center of the body, to a maximum one equal to T = 288.82 K on its extremities. Although, the Vacuum Vessel is maintained at T = 295.15 K, except for a small part of its extremities, which has a temperature T = 291.98 K.

   The thermal power generated from the Warm Bore is equal to $\dot{Q}$ = 8.2553 W.

3. Two central heaters at 2.5 W each and two heaters at the extremities at 2 W each

   The positions of the heaters are shown in Figure 8.9.

   As shown in Figure 8.12, the temperature on the Warm bore varies from a minimum temperature T = 271.48 K on the center of the body, to a maximum one equal to T = 289.89 K on its extremities. Although, the Vacuum Vessel is maintained at T = 295.15 K, except for a small part of its extremities, which has a temperature T = 292.52 K.

   The thermal power generated from the Warm Bore is equal to $\dot{Q}$ = 7.2553 W.

4. Two central heaters at 2.5 W each and two heaters at the extremities at 2.5 W each

   The positions of the heaters are shown in Figure 8.9.

   As shown in Figure 8.13, the temperature on the Warm bore varies from a minimum temperature T = 273.43 K on the center of the body, to a maximum one equal to T = 290.32 K on its extremities. However, in the center of the Warm Bore, a small wedge has the temperature T = 278.26 K. The Vacuum Vessel is maintained at T = 295.15 K, except for a small part of its extremities, which has a temperature T = 292.74 K.

   The thermal power generated from the Warm Bore is equal to $\dot{Q}$ = 6.2553 W.

5. Two central heaters at 3 W each and two heaters at the extremities at 3 W each

   The positions of the heaters are shown in Figure 8.9.

   As shown in Figure 8.14, the temperature on the center of the Warm bore is T = 284.96 K and, moving to the extremities, it first decreases until its minimum T = 279.87 K, then it increases until T = 291.75 K. Although, the Vacuum Vessel is maintained at T = 295.15 K.

   The thermal power generated from the Warm Bore is equal to $\dot{Q}$ = 4.2553 W.

6. Two heaters in the center, two at the extremities and two halfway through them at 2 W each

   The positions of the heaters are shown in Figure 8.15.

As shown in Figure 8.16, the temperature on the Warm bore varies from a minimum temperature T = 283.67 K on the center of the body, to a maximum one equal to T = 292.6 K on its extremities. Although, the Vacuum Vessel is maintained at T = 295.15 K, except for its extremities, which have a temperature T = 293.87 K.

The thermal power generated from the Warm Bore is equal to $\dot{Q}$ = 4.2553 W.

7. Two heaters in the center at 2.5 W, two at the extremities and two halfway through them at 2 W each

   The positions of the heaters are shown in Figure 8.15.

   As shown in Figure 8.17, the temperature on the center of the Warm bore is T = 290.85 K and, moving to the extremities, it first decreases until its minimum T = 287.42 K, then it increases until T = 293.43 K. Although, the Vacuum Vessel is maintained at T = 295.15 K, except for its extremities, which have a temperature T = 294.29 K.

   The thermal power generated from the Warm Bore is equal to $\dot{Q}$ = 3.2553 W.

8. Two heaters in the center at 2.5 W, two at the extremities at 2 W and two halfway through them at 2.5 W each

   The positions of the heaters are shown in Figure 8.15.

   As shown in Figure 8.18, the temperature on the center of the Warm bore is the maximum one, equal to T = 295.15 K, and, moving to the extremities, it first decreases until its minimum T = 290.56 K, then it increases until T = 293.62 K. Although, the Vacuum Vessel is maintained at T = 295.15 K, except for its extremities, which have a temperature T = 294.64 K.

   The thermal power generated from the Warm Bore is equal to $\dot{Q}$ = 2.2553 W.

9. Two heaters in the center, two at the extremities and two halfway through them at 2.5 W each

   The positions of the heaters are shown in Figure 8.15.

   As shown in Figure 8.19, the temperature on the center of the Warm bore is the maximum one, equal to T = 296.7 K, and, moving to the extremities, it first decreases until its minimum T = 292.51 K, then it increases until T = 294.37 K. Although, the Vacuum Vessel is maintained at T = 295.3 K, except for its extremities, which have a temperature T = 294.84 K.

   The thermal power generated from the Warm Bore is equal to $\dot{Q}$ = 1.2553 W.

8.5.2 Discussion of the results

From the steady state thermal analysis on the Warm Bore, the system that consisted of two heaters in the center at 2.5 W, two at the extremities at 2 W and two halfway through them at 2.5 W each, turned out to

be the most efficient. In fact, it allowed to maintain the whole body at a temperature higher than T = 290 K, without warm up it over the room temperature. As we can see from the Simulation 9, if we add just 1 W to the heaters placed at the Warm Bore extremities, the maximum temperature reached by the system starts to exceed the room temperature.

The value of the thermal power generated from the Warm bore can be checked by the Equation 8.2, which can be used for any simulation:

$$\dot{Q}_{TOT} = (\mathrm{A} \times \mathrm{q}) + \sum_{j=1}^{n} n_j \times \dot{Q}_j \qquad \textit{(Eq. 8.2)}$$

where $\mathrm{A} = 10.837\ \mathrm{m}^2$ is the Warm Bore surface area, acquired from Ansys Workbench 17.1, $\mathrm{q} = -1.5\ \mathrm{W/m}^2$ is the imposed heat flux, n_j represents the number of j type heaters and $\dot{Q}_j$ their thermal power.

It is necessary to add together the thermal power generated from the Warm bore without the heaters and the one of the heaters themselves.

In Equation 8.3 is the example for the chosen system:

$$\dot{Q}_{TOT} = (\mathrm{A} \times \mathrm{q}) + \sum_{j=1}^{n} n_j \times \dot{Q}_j = \qquad \textit{(Eq. 8.3)}$$

$$= 10.837 \times (-1.5) + 4 \times 2.5 + 2 \times 2 =$$

$$= -16.255 + 14 = -2.255\ \mathrm{W}$$

The negative sign of the thermal power indicates that it comes out from the Warm Bore surface.

In summary, the chosen arrangement for the heaters allowed to maintain the Warm Bore temperature over the one at which the water freezes. In this way, the icing problem was totally avoided, whether in case of a vacuum loss or a break necessary for maintenance.

REFERENCES

[1] arXiv:1501.05241, *Mu2e Technical Design Report*, March 2015

[2] *ASME Boiler and Pressure Vessel Code*, Section VIII, Division 1, American Society for Mechanical Engineers, New York, 1995

[3] R. P. Reed, A. F. Clark, *Materials at Low Temperatures*, American Society for Metals, Ohio, 1983

[4] J. G. Weisend, *Handbook of Cryogenic Engineering*, edited by CRC Press, July 1998

Table 8.1 – Mesh Size Sensibility for the steady state thermal analyses on the Warm Bore.

Number of Elements	**Body Sizing [m]**	**Mean Temperature [K]**
3347432	3×10^{-2}	265.4
3329459	1×10^{-2}	265.4
3325641	5×10^{-3}	265.36
3340785	3×10^{-3}	265.4
3525134	1×10^{-3}	265.36
3995094	5×10^{-4}	265.36

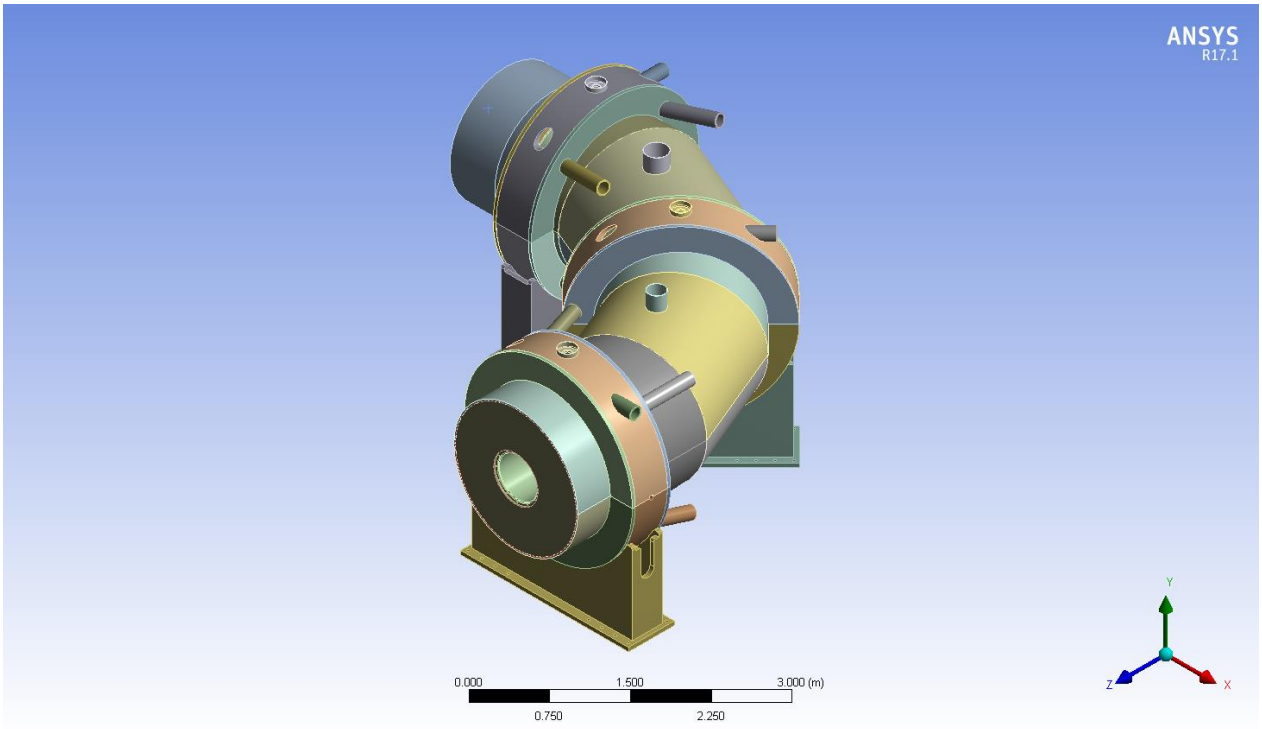

Figure 8.1 – Model of the Vacuum Vessel.

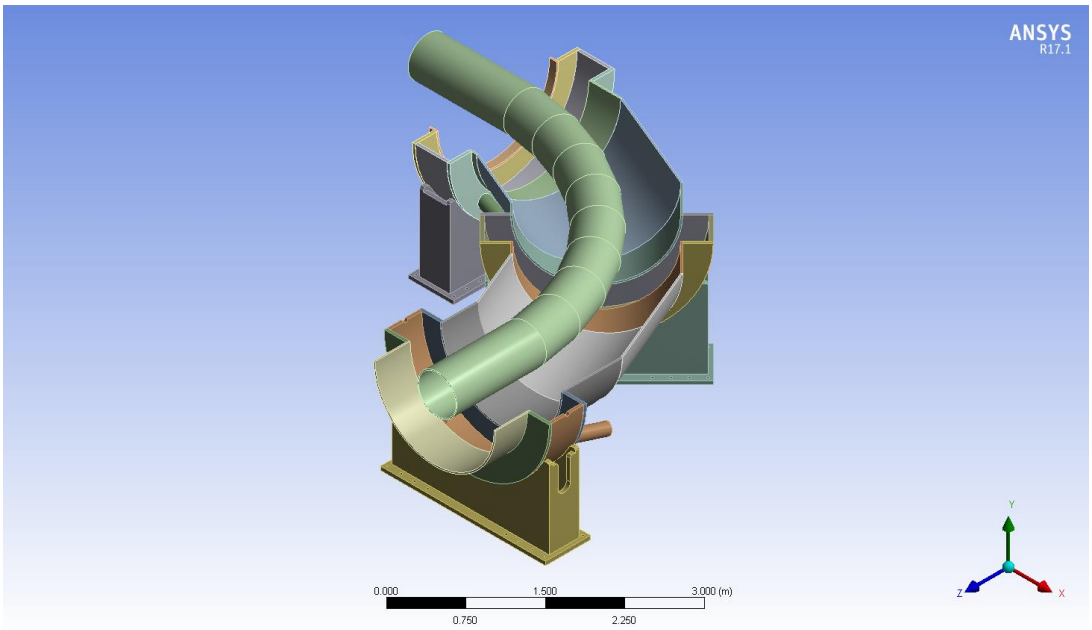

Figure 8.2 – Model of the Warm Bore.

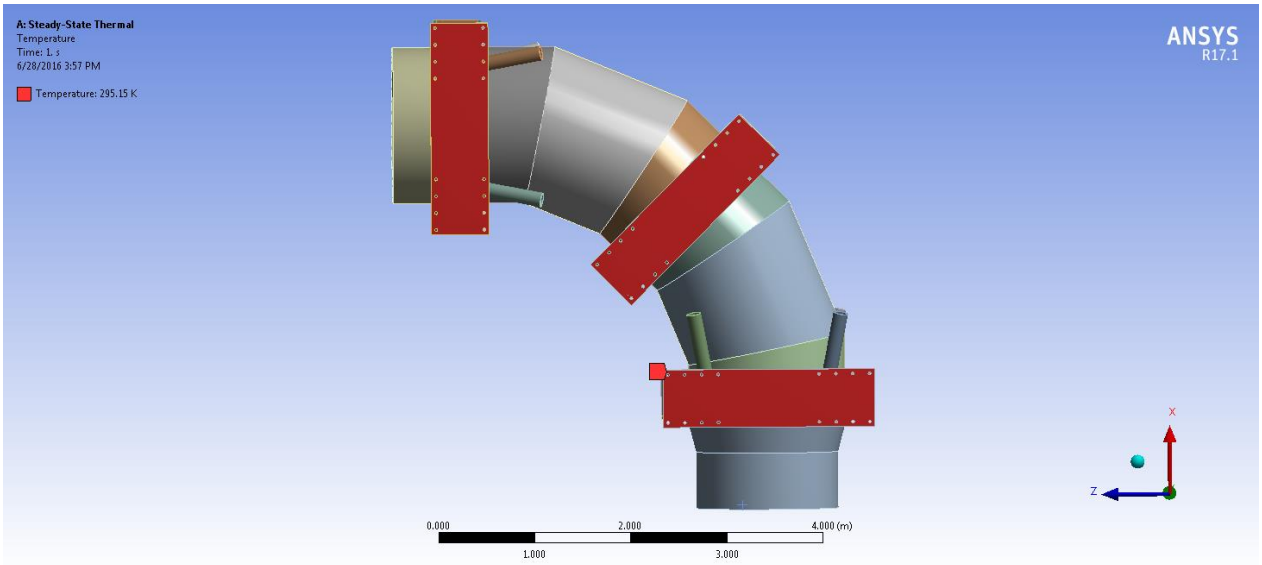

Figure 8.3 – Imposed temperature of T = 295.15 K on the three supports of the Vacuum Vessel.

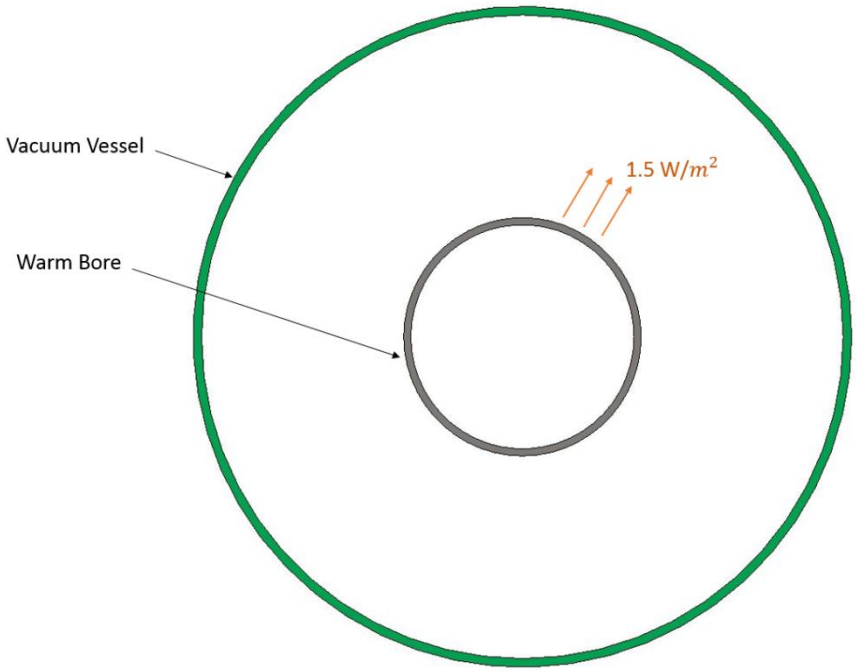

Figure 8.4 – Heat Flux coming out from the outer surface of the Warm Bore. (T. H. Nicol)

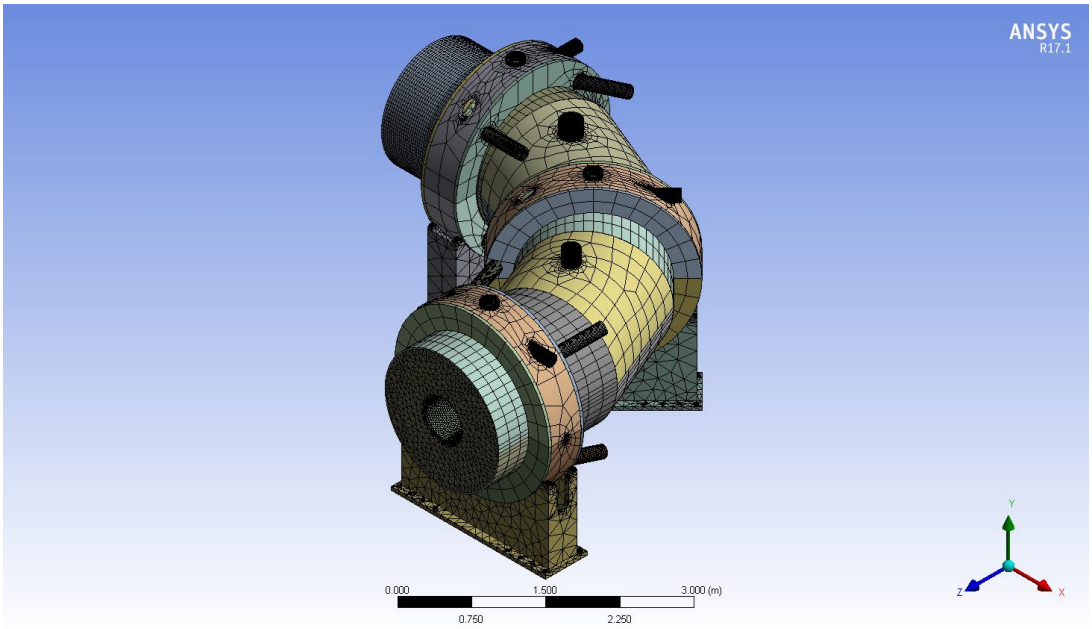

Figure 8.5 – The Mesh on the entire model.

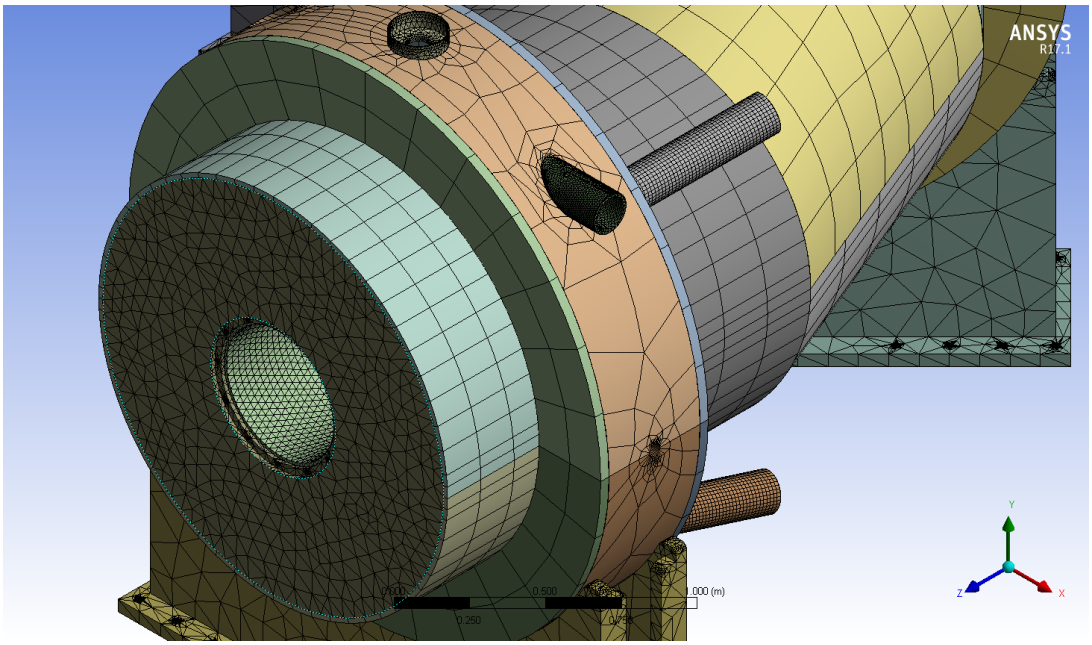

Figure 8.6 – A detail of the Mesh.

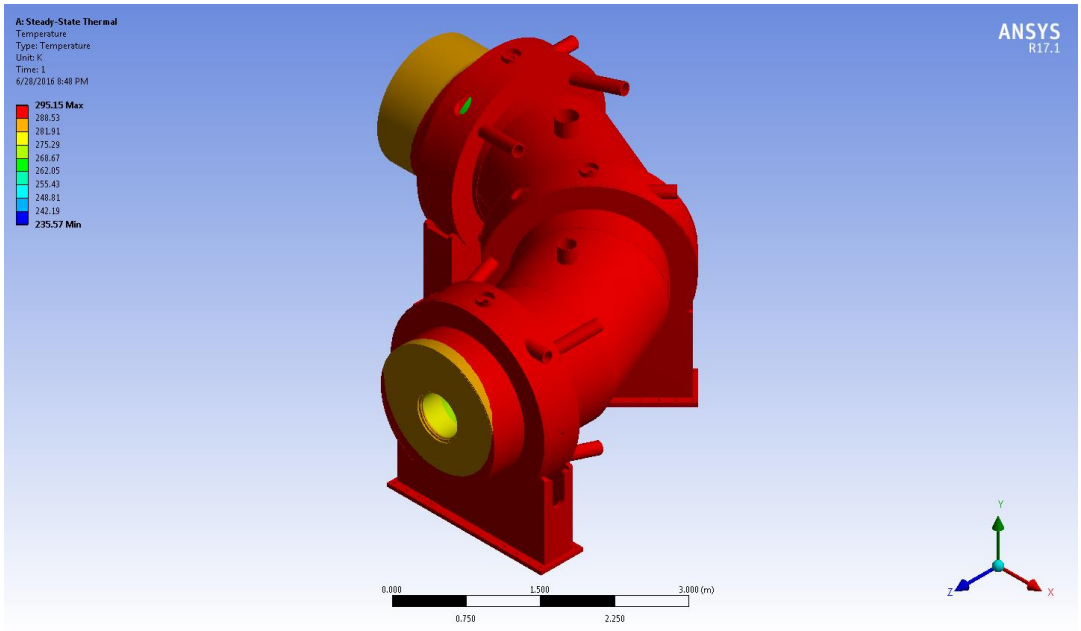

Figure 8.7 – Temperature distribution on the Vacuum Vessel.

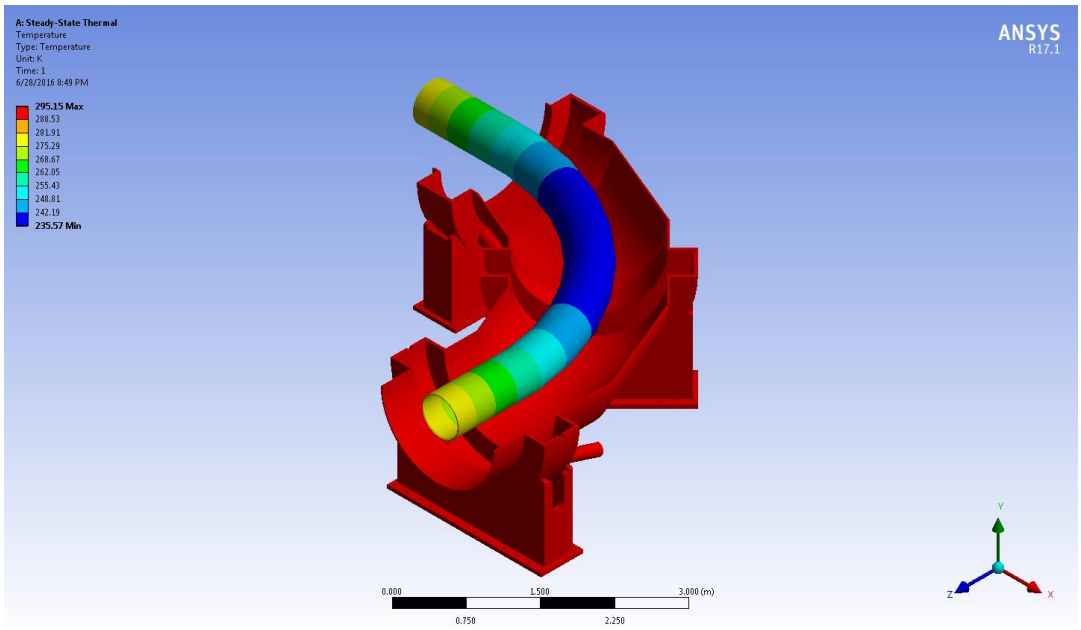

Figure 8.8 – Temperature distribution on the Warm Bore.

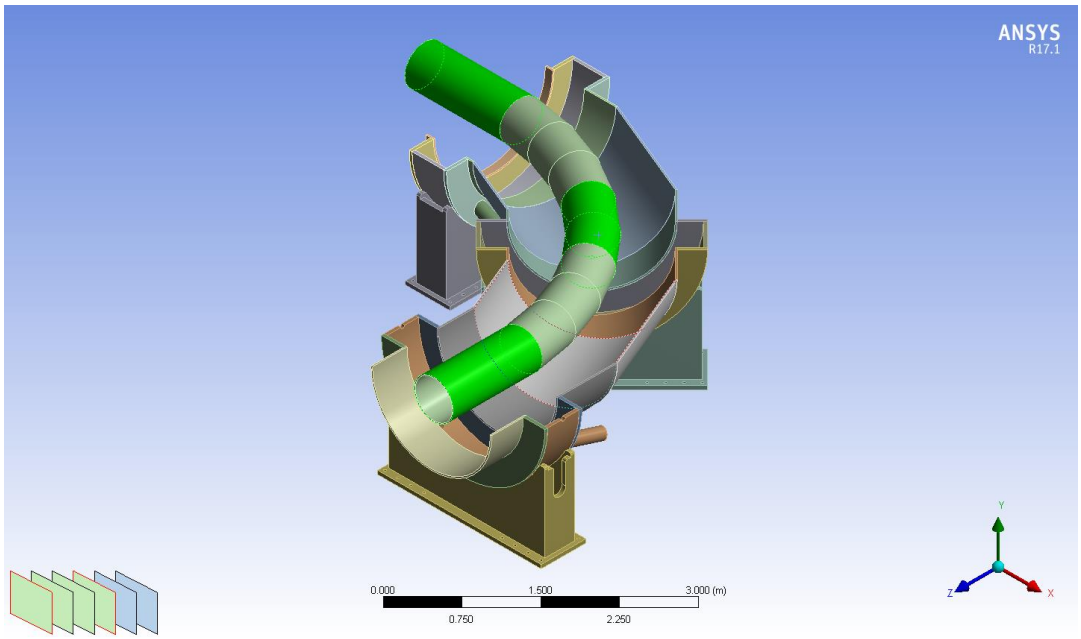

Figure 8.9 – Position of the two heaters in the center and two at the extremities.

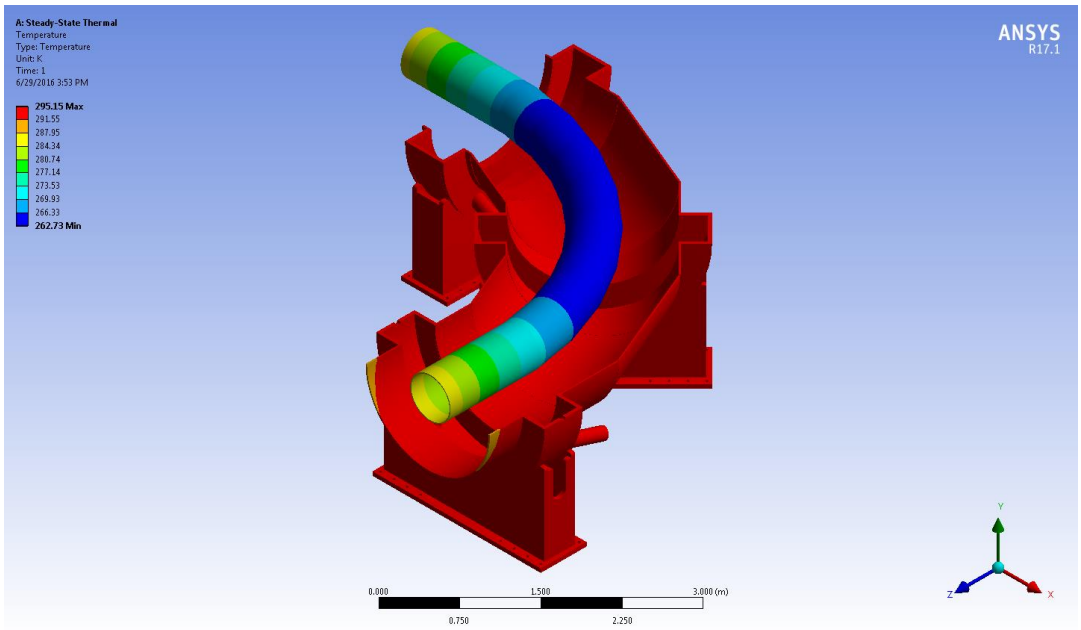

Figure 8.10 – Temperature distribution with two central heaters at 2 W each and two heaters at the extremities at 1 W each.

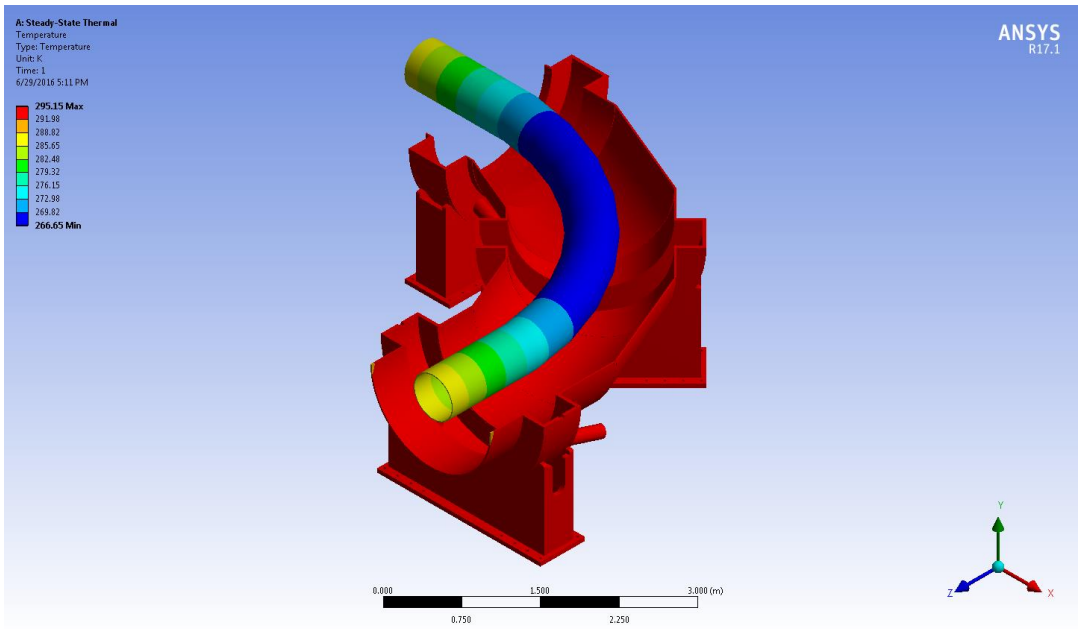

Figure 8.11 – Temperature distribution with two central heaters at 2 W each and two heaters at the extremities at 2 W each

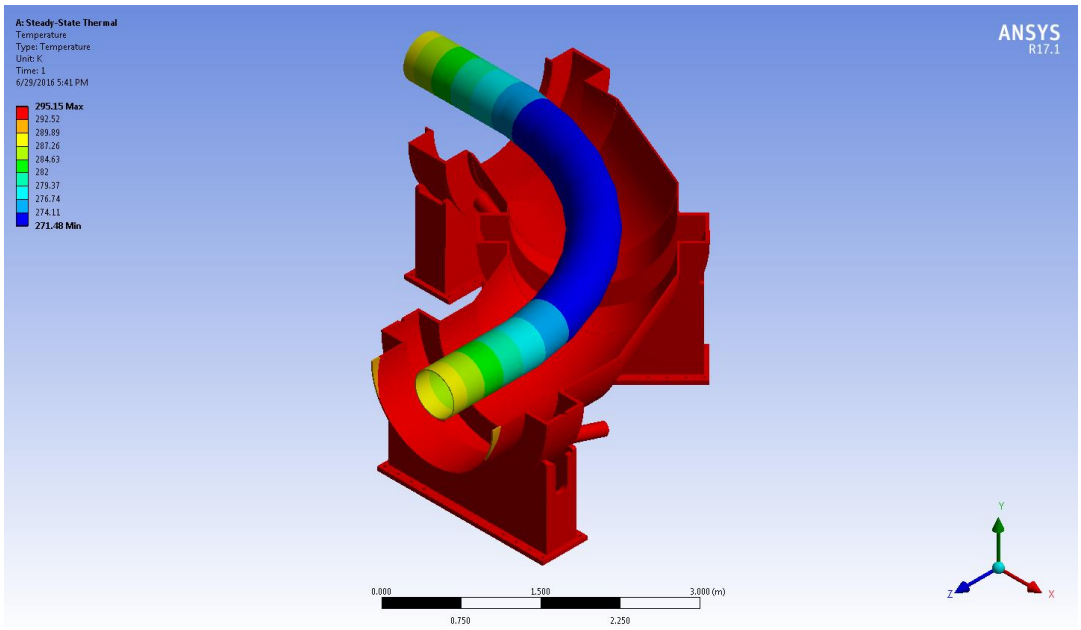

Figure 8.12 – Temperature distribution with two central heaters at 2.5 W each and two heaters at the extremities at 2 W each.

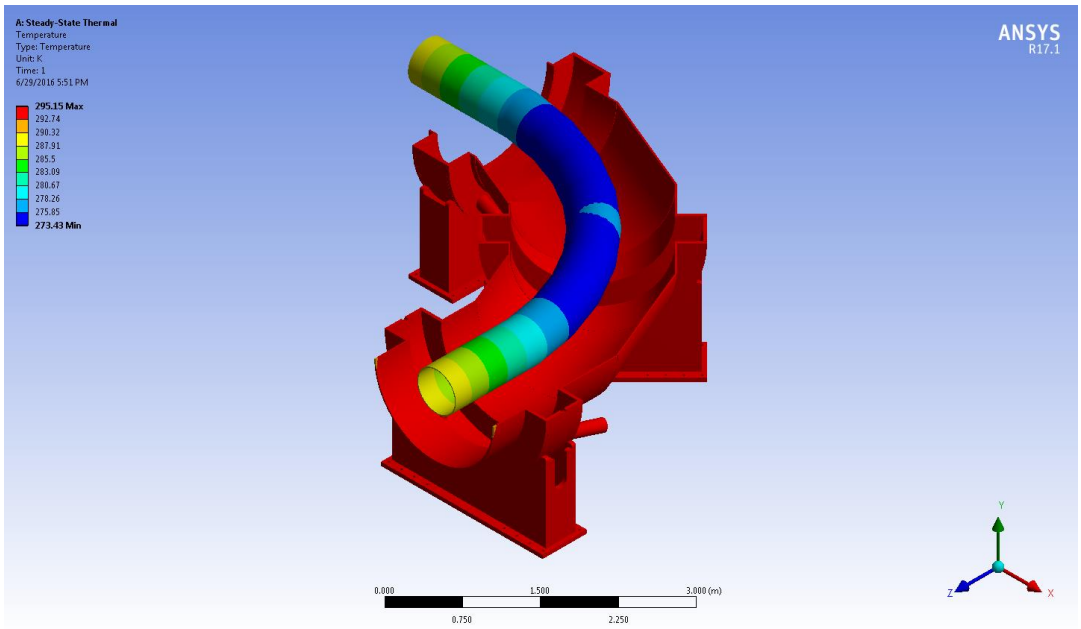

Figure 8.13 – Temperature distribution with two central heaters at 2.5 W each and two heaters at the extremities at 2.5 W each.

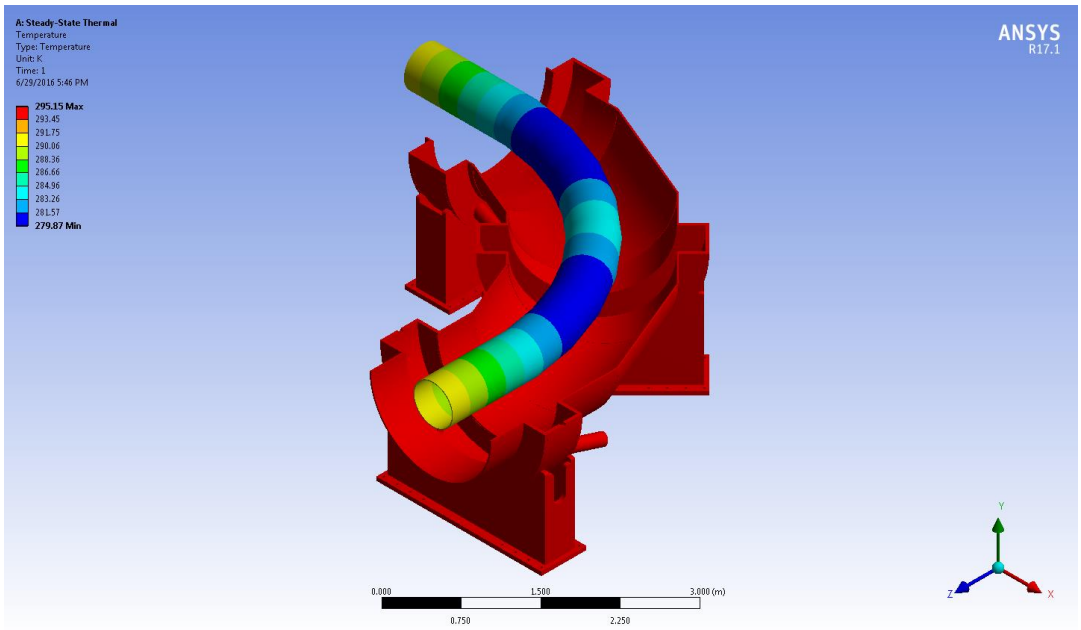

Figure 8.14 – Temperature distribution with two central heaters at 3 W each and two heaters at the extremities at 3 W each.

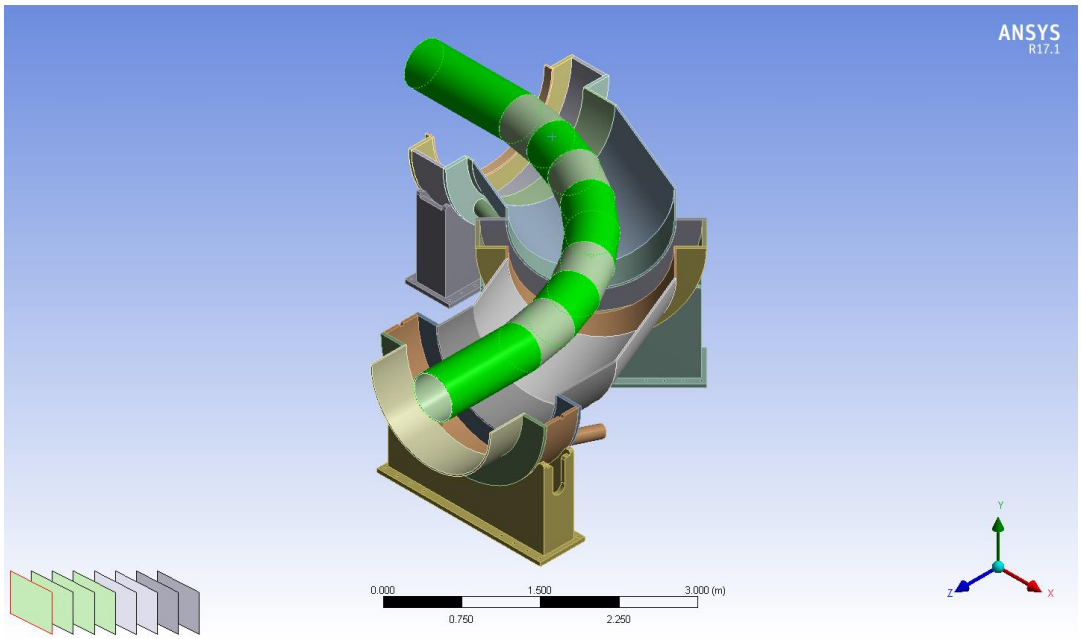

Figure 8.15 - Position of the two heaters in the center, two at the extremities and two halfway through them.

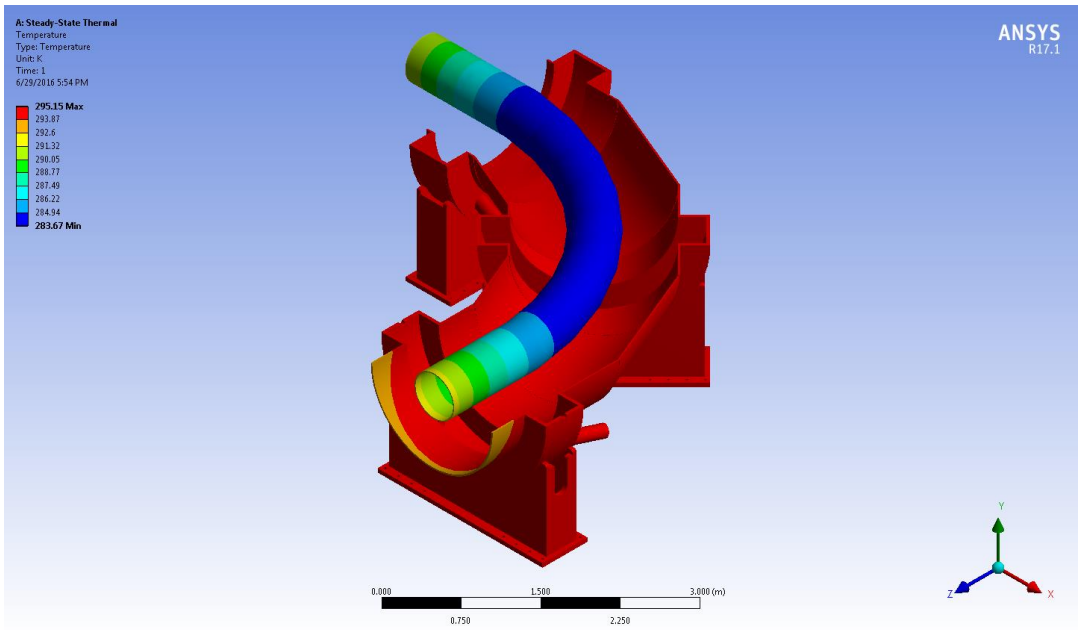

Figure 8.16 – Temperature distribution with two heaters in the center, two at the extremities and two halfway through them at 2 W each.

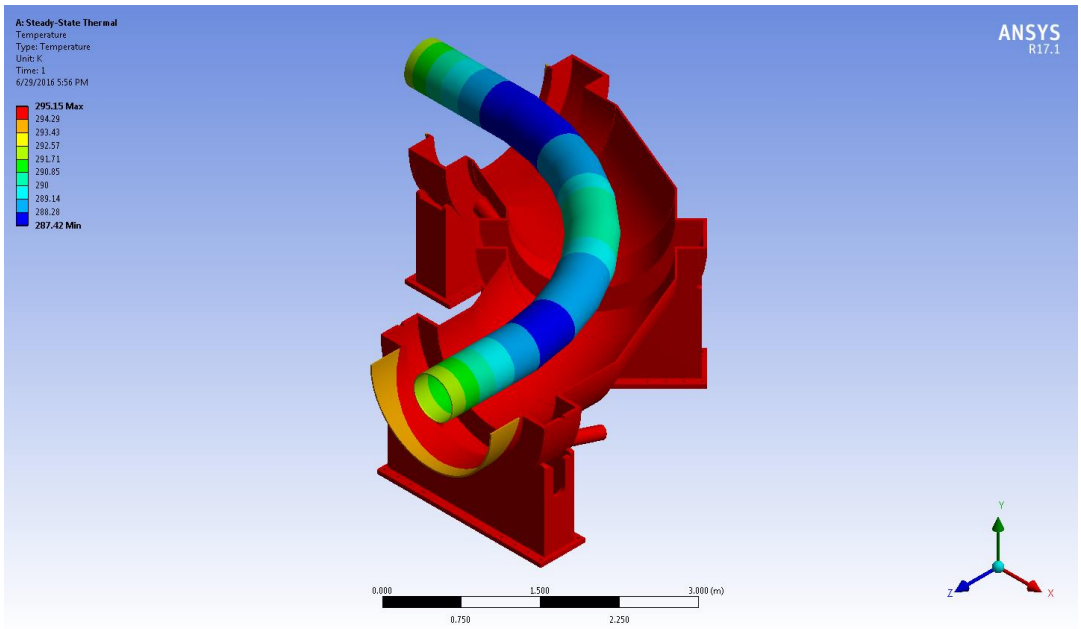

Figure 8.17 – Temperature distribution with two heaters in the center at 2.5 W, two at the extremities and two halfway through them at 2 W each.

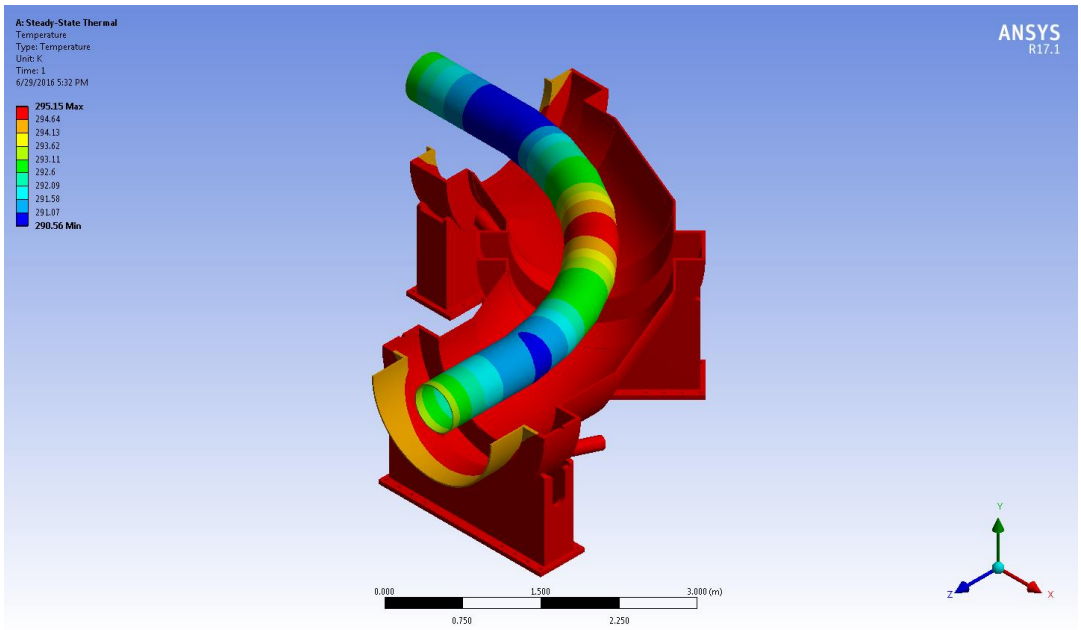

Figure 8.18 – Temperature distribution with two heaters in the center at 2.5 W, two at the extremities at 2 W and two halfway through them at 2.5 W each.

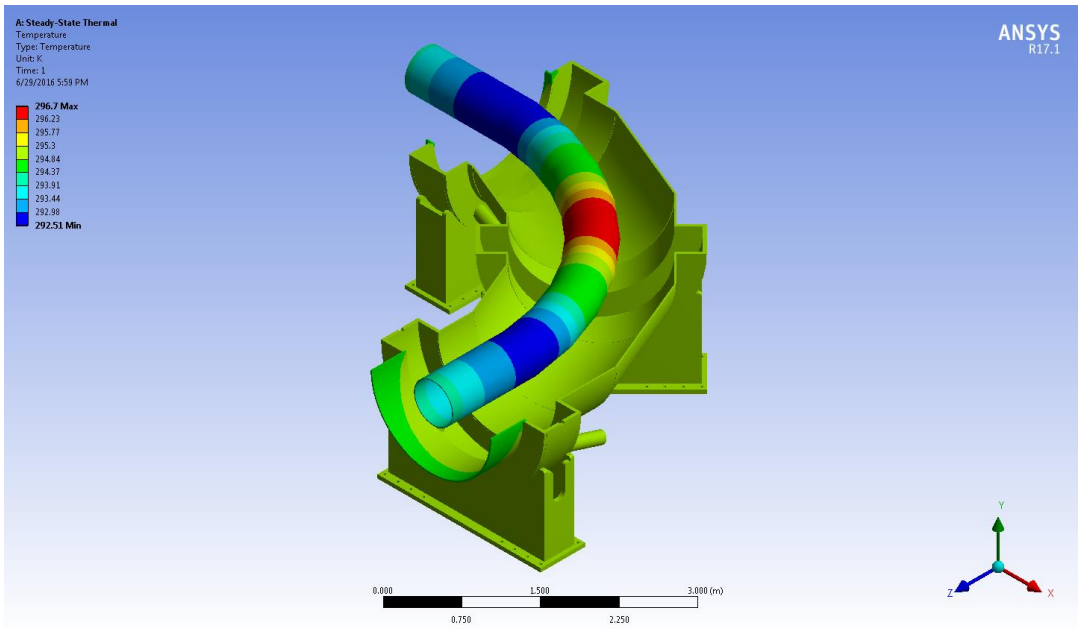

Figure 8.19 – Temperature distribution with two heaters in the center, two at the extremities and two halfway through them at 2.5 W each.

9. CONCLUDING REMARKS

The steady state thermal analysis on the Thermal Shield (Section 7.1) was conducted to identify the most efficient Thermal Shield cooling system, taking into account the heat loads acting on it. The shield had a temperature T = 293 K and was subject to two heat fluxes equal to 1.5 W/m^2, one entering from the external surface of the Outer Thermal Shield and representing the thermal exchange between the Vacuum Vessel and the Thermal Shield, the other entering from the internal surface of the Inner Thermal Shield and representing the thermal exchange between the Warm Bore and the Thermal Shield. Moreover, to represent the thermal effect of the mechanical connections between the Vacuum Vessel and the Thermal Shield, an uniform heat flow equal to 2 W was imposed on the holes inner surfaces of the three gravity support rods and an uniform 5 W heat flow on the ones of the radial and axial support rods. Inside the tubes needed to cool down the shield, was a temperature T = 80 K and the nitrogen had a pressure p = 1.36 bar and a quality equal to x = 0.06 at the entrance of the TSu and a pressure p = 1.01 bar and a quality equal to x = 0.6 at the end of it. The analysis demonstrated that the minimum number of tubes needed to maintain the shield at T = 80 K was three: two tubes at 60° from the horizontal plane on the Outer Thermal Shield and one "external" tube at 45° on the Inner Thermal Shield.

However, in order to be conservative, the number of tubes should be increased at least at five, but this lies outside the subject of this paper.

The transient thermal analysis on the Thermal Shield (Section 7.2) aimed to analyze the time necessary to the Thermal Shield to cool down until a temperature of T = 80 K, using the cooling scheme proposed from the steady state analysis, with three tubes. The heat loads considered were the same of the steady state analysis, in addition to the nitrogen heat transfer coefficient, equal to h = 105.1 W/m^2-K.

The time needed to cool down the Thermal Shield until a temperature T = 80 K was equal to t = 48800 s, that was 13 h 33 min.

The study on the Thermal Shield revealed some delicate aspects of the facility.

Serious attention should be payed to the weld joints between the tubes and the shield, for two different reasons. First of all, the thermal effect of the weld joints on the structure could be examined in depth. Moreover, it is necessary to mention that the weld joints are usually air permeable, so, in case of a vacuum loss inside the Vacuum Vessel, this could generate an air penetration also inside the Thermal Shield.

Another important aspect of the facility is to maintain the vacuum inside it. It is complicated to reach the pressure p = 1.3 x 10^{-4} Pa that we have inside the cryostat and the Warm Bore, but it has to be considered

that even a minimal vacuum loss inside the Vacuum Vessel could cause very strong convective thermal exchanges.

Eventually, during the steady state and the transient thermal analysis on the Thermal Shield, the temperature inside the tubes was considered uniform. Study in depth the distribution of temperature inside them could be useful to guarantee that there are no temperature differences between the walls and the center of the tubes.

The steady state thermal analysis on the Warm Bore without a heating system (Section 8) had the purpose to specify the temperature of the Warm Bore, taking into account the thermal effect of the Thermal Shield, that was represented by an heat flux equal to -1.5 W/m^2.

The analysis demonstrated that the temperature on the Warm bore varied from a minimum T = 235.57 K on the center of the body, to a maximum T = 280 K on its extremities.

The second steady state thermal analysis on the Warm Bore (section 8.5) aimed to establish how many heaters were necessary, in what position and at what power, to maintain the Warm Bore at room temperature, in order to avoid the icing problem during the opening of the cryostat, or even in the case of a vacuum loss.

The system that consisted of two heaters in the center at 2.5 W, two at the extremities at 2 W and two halfway through them at 2.5 W each, turned out to be the most efficient.

However, the analyses conducted on the Warm Bore could be the starting point for an in-depth study about it. First of all, in the analyses the heaters were placed only on the top of the Warm Bore, but it could be interesting to simulate new configurations that take into account also some heaters on the bottom of it.

Secondly, the design of the heaters should be studied as well, in order to choose the most efficient.

Eventually, since it will not be possible to use the heaters during the tests of the magnets, another way to avoid the icing problem should be analyzed.

REFERENCES

1. W. Bertl, SINDRUM II Collaboration, *A Search for muon to electron conversion in muonic gold*, Eur. Phys. J. C47, 337, 2006
2. arXiv:1501.05241, *Mu2e Technical Design Report*, March 2015
3. G. Ambrosio, R. Coleman, V. Kashikhin, M. Lamm, N. Mokhov, J. Popp, V. Pronskikh, *Requirements for the Mu2e Production Solenoid Heat and Radiation Shield*, January 2013
4. G. Tatkowski, S. Cheban, N. Dhanaraj, D. Evbota, M. Lopes, T. Nicol, R. Sanders, R. Schmitt, E. Voirin., *Forced two-phase helium cooling scheme for the Mu2e Transport Solenoid*, IOP Publishing Ltd
5. T. H. Nicol, C. Darve, Y. Huang, T. M. Page, *LHC Interaction Region Quadrupole Cryostat Design and Fabrication*, IEEE Transactions on Applied Superconductivity (Volume:12 , Issue: 1), August 2002
6. N. Templeton, T. Jones, S. Pattalwar, K. Marinov, A. May, E. Nolan, G. Burt, K. Artoos, R. Calaga, O. Capatina, T. Capelli, F. Carra, R. Leuxe, C. Zanoni, A. Ratti, *Design of the Thermal and the Magnetic Shielding for the LHC High Luminosity Crab-Cavity upgrade*
7. T. H. Nicol, *SSC Collider Dipole Cryostat*
8. *Cryostat Design*, contribution to the CAS-CERN Accelerator School: Superconductivity for Accelerators, Erice, Italy, edited by R. Bailey, 24 April - 4 May 2013
9. Ph. Fazilleau, Ph. Bredy, and B. Levesy, *CMS Coil Thermal Shields Final Design*, IEEE Transactions on Applied Superconductivity, Vol. 12, No. 1, March 2002
10. R. Fast, J. Grimson, R. Kephart, E. Leung, L. Mapalo, R. Wands, R. Yamada, H. Minemura, S. Mori, M. Noguchi, R. Yoshizaki, K. Kondo, *Design Report for an Indirectly Cooled 3-m Diameter Superconducting Solenoid for the FERMILAB Collider Detector Facility*, October 1982
11. J. Brzezniak, R.W. Fast, K. Krempetz, A. Kristalinski, A. Lee, D. Markley, A. Mesin, S. Orr, R. Rucinski, S. Sakla, R.L. Schmitt, R.P. Smith, B. Squires, R.P. Stanek, A.M. Stefanik, A. Visser, R. Wands, R. Yamada, *Conceptual Design of a 2 Tesla Superconducting Solenoid for the Fermilab D0 Detector Upgrade*, May 1994
12. ATLAS Collaboration, *ATLAS Magnet Project TDR Volume 4: Central Solenoid*, April 30, 1997
13. G. Tatkowski, J. Catalanell, *Mu2e Nitrogen Process "Steady State" Flow Diagram*, 2014
14. J. E. Fesmire, S. D. Augustynowicz, *Cryogenic Thermal Insulation Systems*, 16th Thermal and Fluids Analysis Workshop, Orlando, Florida, August 9, 2005

15. R. J. Powers, J. D. Gonczy, J. Otavka, R. C. Niemann, A. Szymulanski, J. L. Tague, *5cm, No Iron SSC Dipole 12m Model Cryostat Thermal Performance*, September 1985
16. J. G. Weisend, *Handbook of Cryogenic Engineering*, edited by CRC Press, July 1998
17. *ASME Boiler and Pressure Vessel Code*, Section VIII, Division 1, American Society for Mechanical Engineers, New York, 1995
18. R. P. Reed, A. F. Clark, *Materials at Low Temperatures*, American Society for Metals, Ohio, 1983